UNIVERSITY OF SOUTHAMPTON

EXCITON-POLARITON DYNAMICS IN SEMICONDUCTOR MICROCAVITIES

By

Pavlos G. Lagoudakis

Thesis submitted for the degree of

Doctor of Philosophy

PHYSICS AND ASTRONOMY

FACULTY OF SCIENCE

July 2003

UNIVERSITY OF SOUTHAMPTON

ABSTRACT

FACULTY OF SCIENCE
PHYSICS AND ASTRONOMY

Doctor of Philosophy

EXCITON-POLARITON DYNAMICS IN SEMICONDUCTOR MICROCAVITIES

By Pavlos G. Lagoudakis

This thesis reports an experimental investigation of the nonlinear optical properties of bound electron-hole pairs (excitons) in quantum wells embedded in semiconductor microcavities. A microcavity is a monolithic resonator composed of two Bragg mirrors with cavity length comparable to the wavelength of light. The embedded quantum wells serve as the optically active medium which also confines the electronic excitations. Strong interaction between the cavity photons and the quantum well excitons results in new eigenstates of the system, the so called microcavity exciton-polaritons. Continuous wave excitation, and time-, spectral-, and angular-resolved ultrafast spectroscopy were employed in order to analyze the dynamics of this system.

Microcavity exciton-polaritons exhibit a very steep dispersion around the ground polariton state resulting in a much longer polariton de Broglie wavelength compared to that of bare excitons. Therefore, quantum degeneracy of a polariton gas is achievable at much lower densities than for an exciton gas. Recently, observations of parametric polariton scattering under stimulation of the final state provided conclusive proof of the bosonic behaviour of polaritons. In this thesis a comprehensive analysis of the spin dynamics in the stimulated polariton scattering is presented.

Due to the effect known as relaxation bottleneck, which prevents excitons from relaxing into the ground polariton state, Bose condensation of polaritons has not yet been observed from an initially incoherent population of excitons. However, experimental evidence is presented of the potential of electron-polariton scattering as an efficient process, which can drive polaritons from the bottleneck region to the ground state.

to my grandfather Konstantino

Table of Contents

Acknowledgements

I would like to thank my supervisor Prof. Jeremy Baumberg for giving me the opportunity to work under optimal conditions, and receive continuous support, and competent scientific advice.

I would like to thank Prof. A. Kavokin, Dr. G. Malpuech, and Dr. D. Whittaker for providing theoretical support for this work, and our collaborators Prof. M. Skolnick, Prof. E. Cohen, Prof. L. N. Pfeiffer, and Dr. J. Roberts for many useful discussions and for designing and fabricating the high quality microcavity samples used in the experiments described in this thesis.

I am gratefully indebted to Dr. P. Savvidis, with whom I learnt the first ultrafast experimental techniques, and spent a very pleasant time during my first year in Southampton. I am grateful to Dr. M. C. Netti for patiently transferring her expertise in the lab. I wish to thank Dr. M. D. Martin for the stimulating discussions and for bearing me during the very long nights spent together in the lab. I acknowledge stimulating discussions with all the members of the Quantopt group and especially Prof. R. Harley, S. Hoogland, S. Coyle, and K. Bourdakos.

I am indebted to Dr. G. Malpuech, and Prof. A. Kavokin for the pleasant hospitality and exciting collaboration during my stay in Clermont-Ferrand.

I am grateful to Dr. V. Apostolopoulos, Dr. S. Mailis, S. Coyle, and M. T. Johnson for accomplishing the impossible task of proof reading my thesis.

I express my gratitude to my family for their continuous love and support. A big thank you to Yioula, Tamer, and George for providing the essentials for my survival and sanity. Finally, I thank Martina for the wonderful time spent together.

Southampton, UK
June, 2003

Pavlos Lagoudakis

Chapter 1

Introduction

Present technological applications mostly use silicon-based semiconductor devices. The speed at which silicon electronics can process and modulate electronic signals is very high and has overcome the GHz frequency. However, the processing of information via electronic signals has almost reached its physical limits, which are given by the frequency dependent losses that distort electronic signals.[1] Optical signals have a carrier frequency much higher than that of electronic ones and minimal distortion due to the frequency dependent transmission. Therefore, optical transmission is preferable for information processing. Telecommunication systems based on optical inter-connections are already being used widely for long distance transmissions. The demand for higher transmission bandwidth in short distances is rapidly growing and optical transmission is a very promising candidate. However, at present optical signal modulation is based on silicon technology, which is complex and slows down the final transmission rate. The necessity for a new generation of optoelectronic devices which will directly modulate optical signals is apparent.[2, 3] III-V semiconductors have been the preferred materials for such devices.

Over the past ten years, the development and application of low-dimensional semiconductor heterostructures has been vast and rapid. The doors have opened on a whole new field of physics in quantum confined structures by the epitaxial growth and device fabrication techniques, which are constantly improving. Light emitting diodes, semiconductor lasers, vertical cavity surface emitting lasers, microdisc lasers, and displays are some of the applications based on the enormous technological advance

of epitaxial growth. The physics underlying these exceptional emitters is well understood and relies on the radiative recombination of a population inverted reservoir of electron-hole plasma, which can be achieved by either electrical carrier injection or optical pumping.

1.1 Historical Overview

Exciton-polaritons play an important role in the investigation of the optical properties of semiconductors at energies close to the fundamental energy gap. In an infinite crystal due to the translational symmetry an exciton is strongly coupled to a single photon mode resulting in coupled mode excitations, 'the polaritons', which are the true propagating modes inside the material. An analogous effect involving phonons gives rise to phonon-polaritons.[4] Starting with the pioneering work by Hopfield [5] on polaritons in bulk semiconductors, the investigations in the field of exciton-polaritons has grown rapidly. The first experimental evidence of exciton-polaritons came from the direct measurement of the polariton dispersion by two photon absorption spectroscopy [6] and hyper-Raman scattering [7] experiments. Related properties of bulk polaritons, such as the measurement of the group velocity of wave packets, were investigated experimentally by Ulbrich [8]. However, the most debated property has been the polariton luminescence. Exciton-polaritons are intrinsically stationary states and therefore luminescence occurs only through the propagation to the crystal surface. This makes the luminescence process fundamentally dependent on the volume properties of each specific sample. Investigations on polariton luminescence has been thoroughly studied, both theoretically and experimentally.[9, 10, 11, 12]

The progress in semiconductor technology paved the way to fabrication of heterostructures, such as thin films, quantum wells, and superlattices. The confinement of the electronic wave function within the narrow layers of material of these structures, strongly modifies their optical response with respect to the bulk semiconductor. As a consequence the selection rules for the exciton-radiation coupling are modified and the conservation of the component of momentum orthogonal to the quantum well plane is no longer required. The exciton is thus coupled to a continuum of photon modes and

experiences an irreversible decay in complete analogy with atomic spontaneous emission.[13] The lifetime of quantum well excitons (estimated to be about 20 ps in GaAs structures) is strongly modified by the disorder in these structures which alters the exciton wave function and effects the recombination properties.[14, 15] The free exciton lifetime was measured on very high quality samples by Deveaud *et al.*[16] Quantitatively, the spontaneous emission rates depend on the photon density of states, which can be tailored by modifying the dielectric environment of the quantum well.

By embedding the quantum wells in a cavity (semiconductor microcavity) it is possible to inhibit or enhance the spontaneous emission as predicted by Purcell (1946).[17] When the enhancement of the light matter interaction is strong enough, the system cannot any longer be explained by the perturbative Fermi's golden rule for the weak coupling regime. In the strong coupling regime the exciton-photon interaction is non-perturbative and new modes appear in the system, as observed by Weisbuch.[18] The normal modes of the microcavity system cannot be described by photons or excitons alone but by a mixing of these bare modes. Such half-matter half-light quasi particles are the so-called microcavity polaritons.

Unlike the quantum well excitons, the microcavity polaritons have a very sharp energy dispersion [19] due to the cavity photon component, which has a very light mass. Unlike the bare cavity photons, polaritons have pronounced nonlinear behaviour because of their exciton-exciton interaction and the transition to the perturbative regime of the exciton-photon coupling. Semiconductor microcavities allow for direct manipulation of their light quasiparticles by laser beams both in energy and momentum space. They provide an ideal laboratory for the study of nonlinear dynamics of interacting particles with integer spin. As long as the excitation densities are below the exciton saturation, polaritons behave as good bosons. Bosonic effects such as stimulated scattering and Bose condensation can be investigated under low density excitation. These effects have been studied in bulk semiconductors and the outcome has always been very controversial.[20, 21] This is in contrast to the investigations of ultra-cold trapped atoms where spectacular demonstrations of Bose condensation have been achieved.[22]

The peculiar properties of microcavity polaritons have opened the field for the

observation of bosonic effects in the solid state with the recent example of the experimental observation of stimulated polariton amplification reported by Savvidis *et al.*[23] However, the finite microcavity polariton lifetime makes effects, such as the thermal equilibrium Bose condensation impossible to observe in this system. Nevertheless, non-equilibrium condensation phenomena are good candidates for this two-dimensional system.[24]

1.2 Outline

This thesis presents experimental results on the nonlinear dynamics of excitons and photons in semiconductor planar structures. The work presented in this thesis has been inspired by prior theoretical investigations [25] and has led both to the experimental validation of the theory and to the development of further theoretical models.[26, 27] The structure of this thesis is the following:

Chapter 1 as presented above.

Chapter 2 contains a brief overview of the theory of excitons and exciton-polaritons in bulk semiconductors, quantum wells and semiconductor microcavities.

Chapter 3 gives a description of the experimental methods used for measuring the parameters that characterize light-matter interactions including the basic principles of the major experimental equipment and the characteristics of the samples that were employed in this study.

Chapter 4 presents a review of related work on semiconductor heterostructures.

Chapter 5 investigates the experimental observation of electron-polariton scattering in a structure that allows control of the electron density. This process has been proposed as an efficient mechanism that can drive polaritons to the ground state, achieving Bose amplification of the optical emission. Substantial enhancement of

photoluminescence is reported under non-resonant excitation.

Chapter 6 analyzes the polarization dynamics of the light emitted from semiconductor microcavities in the regime of parametric polariton scattering. A microscopic theoretical model that could explain the spin dynamics of the parametric polariton scattering is discussed together with the phenomenological arguments that support it.

Chapter 7 studies the coexistence of low-threshold lasing and strong coupling in a high quality semiconductor microcavity under near resonant optical pumping. The appearance of this lasing mode distinguishes between quantum-well excitons which are strongly-coupled and quantum well excitons which are weakly-coupled with the cavity mode.

Chapter 8 summarizes the results of this thesis and suggests further experimental investigations.

Chapter 2

Basic Concepts of Exciton-Polaritons

During the last five decades, a significant number of studies have been performed in condensed matter physics on semiconducting materials. Apart from the impressive technological applications in electronics and optical telecommunications, semiconductors have been a very fertile ground for fundamental research.[28] In this chapter, some basic concepts of semiconductor physics are revised.

2.1 Excitons

In semiconductors, apart from the optical transitions for photon energies bigger than the energy band gap, $\hbar\omega \geq E_g$, there are some transitions that occur for $\hbar\omega \leq E_g$. These transitions are allowed due to the formation of bound electron-hole (e-h) pairs as a result of the attractive e-h Coulomb interaction. These bound states, which are called '*excitons*', are discrete transition resonances of binding energy E_b. Therefore, photon absorption can occur at energies, $\hbar\omega = E_g - E_b$, even below the band gap, E_g. On the other hand, when a bound electron-hole pair recombines, the exciton annihilates and its energy is transferred to a photon (radiative recombination) or to lattice vibrations or impurities (non-radiative recombination). Excitons in semiconductors are usually shallow, i.e. their radius is much larger than the interatomic spacing: as such they can be described by a two particle effective-mass equation (Wannier-Mott excitons).[29] The opposite extreme, i.e. that of tightly bound (or Frenkel) excitons,

is appropriate to molecular crystals.[30]

2.1.1 Excitons in Bulk Semiconductors

An exciton in a bulk semiconductor, being a bound state of a positive and a negative charge, is reminiscent of positronium. However, exciton physical scales are rather different. If we replace the proton mass with the reduced electron-hole mass, ($\frac{1}{\mu} = \frac{1}{m_e} + \frac{1}{m_h}$), and the electronic charge by $\frac{e}{\epsilon}$, we can use the Bohr hydrogen model to describe an exciton. Therefore, the energy of an exciton state is given by the modified exciton Rydberg energy

$$E_{ex} = E_g - \frac{\hbar^2}{2\mu\alpha_{ex}^2 n^2} + \frac{\hbar^2 K^2}{2M} \tag{2.1}$$

where $\alpha_{ex} = \frac{\hbar^2\epsilon}{e^2\mu}$ is the exciton Bohr radius, ϵ is the dielectric constant, n is the principal quantum number and $K = k_e + k_h$, $M = m_e + m_h$ are the translational wave vector and mass of the exciton respectively. Due to the light effective masses of the carriers and the dielectric screening of the Coulomb interaction, the exciton Rydberg is much smaller and the exciton radius much bigger than the atomic one. For most semiconductors, the exciton radius is larger than the lattice constant and hence the '*orbits*' of electron and hole around their common center of mass average over many unit cells, which justifies the effective-mass approximation.[31]

Thus, excitons seem to be very fragile objects. For example in GaAs, the exciton binding energy is 4.2meV, exciton Bohr radius $\sim 120\mathring{A}$ and $\epsilon \simeq 13.13$ (compared with 13.6eV and $0.5\mathring{A}$ in the hydrogen atom). Even the room temperature thermal energy ($k_BT \simeq 25meV$) is bigger than the exciton Rydberg. Consequently, the conditions under which excitons play an important role in semiconductors are quite stringent and depend on the exciton energy compared to the thermal energy, the mean distance of electron-hole pair compared to the exciton Bohr radius, the screening length, and the phase space filling. The screening length is a measure of the effectiveness of the Coulomb interaction between two carriers in the presence of other carriers (Coulomb screening effect). The phase space filling originates from the fermionic nature of the individual electrons and holes. Pauli's exclusion principle forbids the occupation of

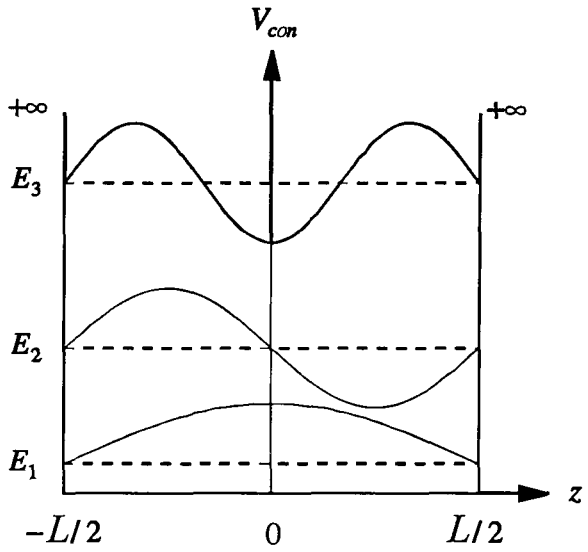

Figure 2.1: Energy eigenfunctions and eigenvalues of the three lowest energetically states for an infinite one-dimensional square potential well

the same quantum state by particles with the same quantum numbers. The effect of phase space filling in *e-h* attraction is similar to that of screening but of a quantum nature. A consequence of these many-body effects is the decrease of optical transition energy with the increase of carrier density. This energy red-shift is called 'band gap renormalization' energy and is independent of the electron momentum.

2.1.2 Quantum Well Excitons

With the advent of modern crystal growth techniques, it has become possible to fabricate microstructures with one or more of the dimensions of the structure comparable to the de Broglie wavelength of its elementary excitations. In that case, the electronic and optical properties deviate substantially from those of bulk materials and the effects of quantum confinement become pronounced. Quantum confinement of one (two, three) spatial dimension results in quantum well structures (quantum wires, quantum dots). The most pronounced effects of quantum confinement are the modification of the electronic energy levels of a crystal and the alteration of the density of states.

In the ideal quantum confinement conditions of a quantum well (QW) of width L (infinite potential barrier at the walls), the elementary excitations are completely

confined in the microstructure and the electronic wavefunctions vanish beyond the walls, Fig.2.1. In the growth direction, perpendicular to the walls, the confinement of the wave functions results in the quantization of the corresponding wavevector component

$$k_{n\perp} = n\pi/L \tag{2.2}$$

and the bound energy states

$$E_{n\perp} = \frac{\hbar^2 k_{n\perp}^2}{2m_\perp} = \frac{\hbar^2 \pi^2 n^2}{2m_\perp L^2} \tag{2.3}$$

where n=1,2,... The total energy of an electron subject to one-dimensional quantum confinement is

$$E_{tot} = E_{n\perp} + E_{//} \tag{2.4}$$

where $E_{//} = \hbar^2 k_{//}^2 / 2m_{//}$ is the energy corresponding to the free motion of the electron on the plane parallel to the walls.

Two dimensional density of states

An important difference between bulk and quantum well structures is the density of states. In the parabolic energy band approximation and for symmetric band structure in the plane parallel to the walls the energy density of states is constant

$$\rho_{2D} = \frac{m_\perp}{\pi L \hbar^2} \tag{2.5}$$

On the other hand, the energy density of states in a bulk semiconductor is

$$\rho_{3D} = \frac{1}{2\pi^2} \left(\frac{2m}{\hbar^2} \right)^{3/2} \sqrt{E_{ex}} \tag{2.6}$$

which tends to zero at the bottom of the band, Fig.2.2. Therefore, in quantum wells all the dynamical phenomena, such as scattering, optical absorption and gain, remain finite at low kinetic energies and low temperatures.[32]

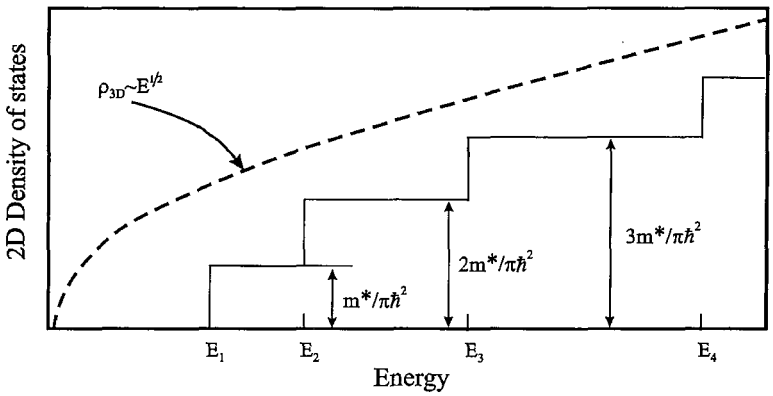

Figure 2.2: 2D density of states and comparison with the 3D density of states, calculated for a layer with thickness equal to that of the quantum well.[33]

2.1.3 Optical Properties of Excitons

In the simplified picture of the two band model (one valence band and one conduction band), an exciton can be considered as a two level system. In this case, the exciton-photon interaction is reminiscent of the two level atom-photon interaction. The optical transition probability in the presence of an electric field is given by Fermi's golden rule

$$\lambda_{if} = \frac{2\pi}{\hbar} |M_{if}|^2 \rho_f \tag{2.7}$$

where λ_{if} is the transition probability, M_{if} is the matrix element of the interaction and ρ_f the density of final states. In the electric dipole approximation the interband optical matrix element can be written

$$M_{if} = \langle f | H_I | i \rangle = \langle f | -\mu \cdot E(t) | i \rangle \tag{2.8}$$

where μ is the electric dipole moment of the two level transition and $E(t)$ is the time varying external electric field. The dipole approximation is justified when the dipole size is several orders of magnitude smaller than the wavelength of the excitation field of the optical transitions.

Exciton oscillator strength

Since the exciton Bohr radius is bigger than the interatomic distance in the crystal, its wavefunction extends over many lattice sites of the crystal.[29] Thus, the exciton

collects the dipole oscillator strength of many atoms. More precisely, the excitonic oscillator strength can be derived in the following way [34]

$$f_{exc} = \frac{2}{m_e \hbar \omega} |\langle f | H_I | i \rangle|^2 = \frac{4}{m_e \hbar \omega} |\langle u_v | \eta \cdot \mathbf{p} | u_c \rangle|^2 V |\psi_n(r=0)|^2 \delta_{k_{ex},0} \tag{2.9}$$

where m_e is the free electron mass and ω is the optical transition frequency, u_v and u_c represent the Bloch wavefunctions of the valence band and the conduction band, V is the crystal volume, η is the polarization vector of light and $\psi_n(r)$ is the exciton envelope function. For the 1s exciton state,

$$|\psi_{1s}(r=0)|^2 = \frac{1}{\pi \alpha_{ex}^3} \tag{2.10}$$

Therefore,

$$f_{exc} = f_{atom} \frac{V}{\pi \alpha_{ex}^3} \tag{2.11}$$

where f_{atom} is the oscillator strength for a uncorrelated electron-hole pair. Thus, the strong correlation of an electron-hole pair in an exciton enhances the oscillator strength by a factor of $V/\pi\alpha_{ex}^3$. Furthermore, the dimensionless oscillator strength is proportional to the crystal volume due to the extending of the center of mass wavefunction over the whole crystal (impurities and crystal disorder neglected). A meaningful quantity is the exciton oscillator strength per unit volume for bulk semiconductor, or per unit area for quantum well excitons, which is directly related to the absorption coefficient $\alpha(\omega)$ through

$$f_{3D} = \frac{f_{exc}}{V} \propto \int \alpha(\omega) d\omega \tag{2.12}$$

and

$$f_{2D} = \frac{f_{exc}}{S} \propto \int \alpha(\omega) d\omega \tag{2.13}$$

correspondingly. A comparison between the exciton oscillator strength per unit volume (3D, bulk case) and per unit area (2D, QW case) shows that

$$f_{2D} = 8 \cdot f_{3D} \tag{2.14}$$

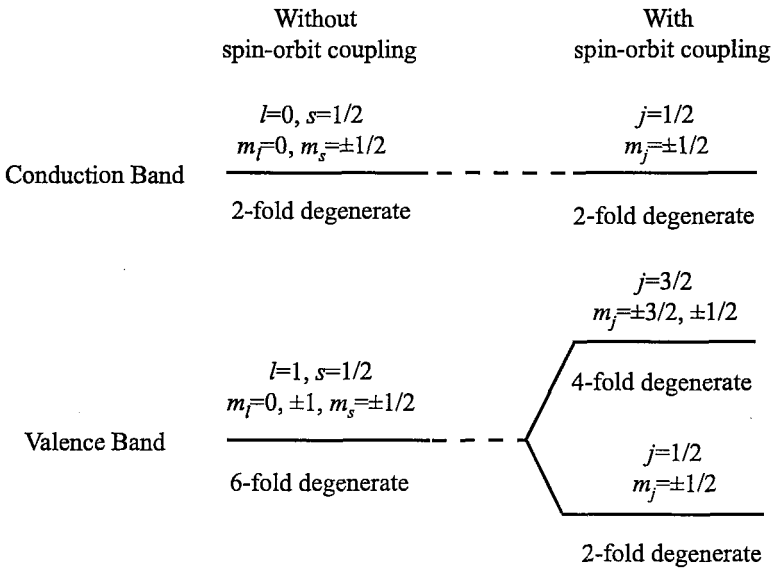

Figure 2.3: Electron (hole) eigenstates at $k = 0$ for the lowest (upper) conduction (valence) band states in bulk GaAs. In the absence of spin-orbital coupling the eigenstates are $|lsm_l m_s >$, where l, m_l and s, m_s are the total and z-component quantum numbers for the orbital and spin angular momenta, respectively. With spin-orbit coupling the eigenstates become $|ls; jm_j >$, where j, m_j are the quantum numbers for the total (orbital plus spin) angular momentum.

where the approximation[1] $a_{2D} = a_{3D}/4$ has been used. The above analogy can intuitively be understood by the fact that in quantum wells the overlap of the electron and hole wavefunctions is bigger than in excitons in bulk semiconductors due to the spatial confinement and hence the optical matrix element is larger.

2.1.4 Exciton Spin and Angular Momentum

The study of the exciton spin, and therefore polariton spin dynamics, requires a clear representation of the exciton spin states. The spin state of an exciton is a direct product of the conduction band electron and valence band hole spin states.

For III-V compounds like GaAs, the conduction and valence band structure are calculated using the *Kane* or $\mathbf{k} \cdot \mathbf{p}$ theory [35] and the Luttinger Hamiltonian.[36] The results for bulk GaAs are summarized in figure 2.3. The lower conduction band states at $k = 0$ have an s-like symmetry (l=0), and therefore a two-fold spin degeneracy

[1]This approximation holds in the 2D exciton case

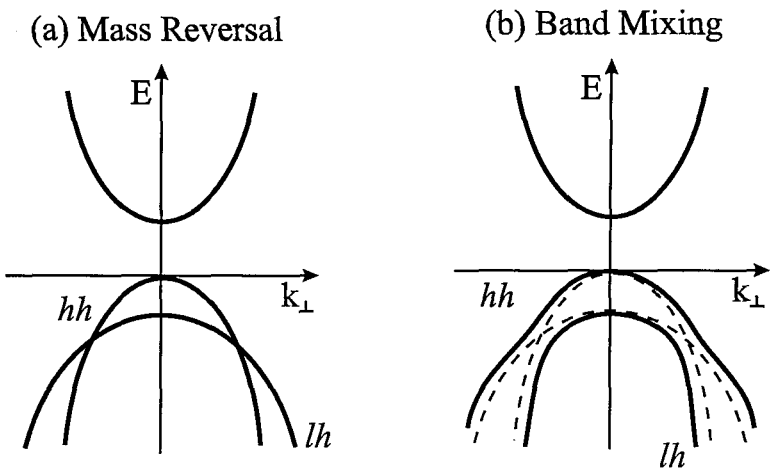

Figure 2.4: (a) Heavy (hh)and light (lh) hole bands in the absence of band mixing in quantum wells showing the *mass reversal*, (b) Heavy (hh)and light (lh) hole bands in the presence of band mixing (*solid curves*) showing the removal of the degeneracies that are present without band mixing (*dashed curves*).

($m_s = \pm\frac{1}{2}$) without spin orbit coupling. The upper most valence band states have a p-like symmetry (l=1), and therefore a six-fold degeneracy without spin orbit coupling. The coupling between the orbital angular momentum and the electron spin when it is small (in comparison to the electrostatic interaction, *Russell – Saunders* case) results in new eigenstates of the total angular momentum, J of the system. For the $J = 1/2$ conduction band the new eigenstates are $|\pm\frac{1}{2}>$, for the $J = 3/2$ heavy-hole valence band are $|\pm\frac{3}{2}>$, for the $J = 3/2$ light-hole valence band are $|\pm\frac{1}{2}>$, and for the split-off holes, $J = 1/2$, are $|\pm\frac{1}{2}>$, where the repeated quantum numbers have been omitted, Fig.2.3.

In quantum wells the band structure is further modified due to the quantum confinement. The influence of quantum confinement causes significant band mixing especially on the top two bulk semiconductor valence bands, the heavy-hole and the light-hole bands. This effect is treated again within the framework of the Luttinger Hamiltonian [37] and results in an anti-crossing of the two bands. Another difference between the quantum well structures and the bulk semiconductors is that the effective mass has different values for the confinement (growth) and the transverse (in-plane) directions.[31] States with a heavier effective mass in the confinement direction have a lighter effective mass in the transverse direction. This is commonly referred to as

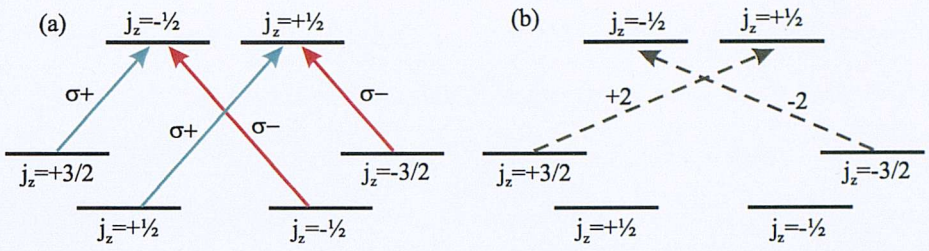

Figure 2.5: (a) single photon absorption optically allowed transitions for heavy and light-hole states, (b) optically inactive transitions, '*dark states*'.

'*mass reversal*'. The convention is to use the terms light- and heavy-holes according to the respective mass in the confinement direction. Therefore, light-holes are heavier than heavy-holes in a quantum well. The effects of quantum confinement on the band structure of quantum wells are summarized in figure 2.4.

When a photon is absorbed to resonantly excite an exciton with electron and hole spins denoted by (s, m_h), the possible transitions are governed by angular momentum conservation between the exciton spin and the polarization of light

$$m_p = s + m_h \tag{2.15}$$

where m_p is the photon spin and can take the value ± 1 for the $\sigma\pm$ circular polarizations. The possible transitions are summarized in figure 2.5. The $(s + m_h = \pm 2)$ excitonic states are optically inactive since they cannot be excited by a single photon absorption although they can be excited by two photon absorption processes.

An appropriate basis to describe the different polarization states of the optical transitions of the heavy hole excitons is that of the two opposite circular polarization states, $|1>$ for $\sigma+$ and $|-1>$ for $\sigma-$. Therefore, circularly polarized light $\sigma\pm$ creates excitons on states $|\pm 1>$, the '*circular excitons*', and linearly polarized light creates linear combinations of the $|\pm 1>$ states. In particular, $H-$ and $V-$linearly polarized light (horizontal, vertical polarization) create the '*linear exciton*' states $|H>=(|1>+|-1>)/\sqrt{2})$, $|V>=(|1>-|-1>)/i\sqrt{2})$ correspondingly. The photo-induced inequality of the states $|\pm 1>$ in the population, created by circular or elliptical polarized light is called '*optical orientation*' of excitonic spins and is a particular case of a more general phenomenon, namely the selective optical excitation of excitonic sublevels. Another example of the selective excitation is the '*optical alignment*' of

excitons by linearly polarized radiation. Linearly polarized light can, under resonant conditions, excite the exciton states with a definite direction of oscillating electric dipole moment. Such a state can also be described as a coherent superposition, $(|1> + e^{i\phi}|-1>)/\sqrt{2}$, of states $|\pm 1>$, where the phase ϕ is determined by the orientation of the polarization plane.

Exciton spin polarization has been extensively studied in bulk semiconductors [38, 39] and semiconductor heterostructures.[40] For an extensive review see Ivchenko and Pikus.[41]

2.2 Cavities

Quantitatively, the spontaneous emission rates depend on the photon density of final states. Tailoring the photon density of states by modifying the dielectric environment of the quantum wells allows control of the spontaneous emission rates. Thus, we can enhance or inhibit the spontaneous emission rate by enlarging or reducing the resonant photon density of states, as was predicted by Purcell and will be thoroughly discussed in section 2.3.1.[17]

The density of optical modes as a function of wavelength in a structure that confines photons depends on the dimensionality of the structure in a similar manner to that of the density of electrical carriers in a quantum well, wire or dot.[42, 43] In the bulk, 3D case $L \gg \lambda/2n$, the optical mode density increases quadratically with frequency, Fig.2.6a

$$\rho(\omega) = \frac{\omega^2}{2\pi^2 c^3} \tag{2.16}$$

In a planar cavity, the optical modes in the direction perpendicular to the mirror plates are quantized

$$k_z = \frac{2\pi}{L} m_z \tag{2.17}$$

where L is the distance between the mirrors and m_z is an integer. In the transverse direction (parallel to the mirror planes), there is a continuum of optical modes, owing

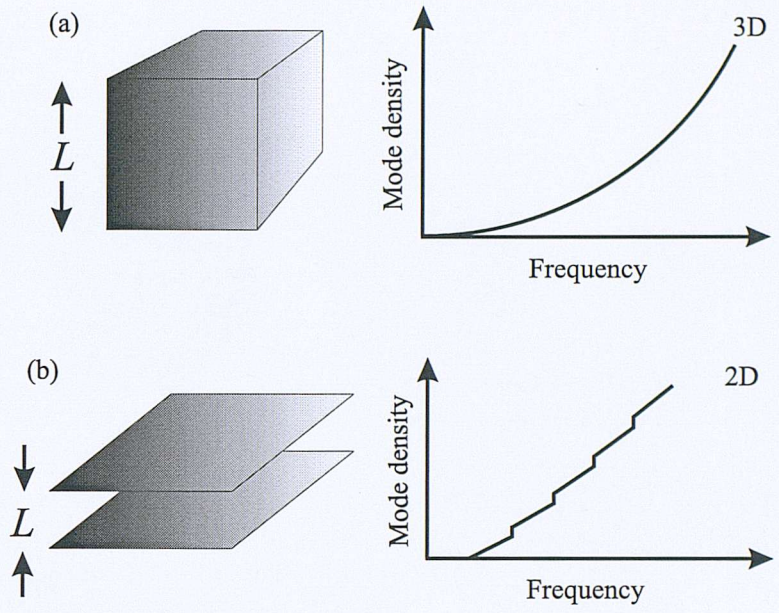

Figure 2.6: Mode density as a function of frequency for (a) a bulk cavity with $L \gg \lambda/n$, (b) a two dimensional cavity.

to the lack of optical confinement. Hence, the 2D density of states is

$$\rho(\omega) = N_z \frac{\omega}{2\pi^2 c^2} \tag{2.18}$$

where N_z is an integer less than $2L/\lambda$, equal to the number of quantized longitudinal modes in the cavity. The optical mode density increases stepwise each time another half-wavelength fits between the planar mirrors (N_z jumps by one). Between these steps, the mode density increases linearly owing to the modes propagating in the transverse direction, Fig.2.6b.

2.2.1 Fabry-Pérot Etalon

The simplest structure for the confinement of the electromagnetic field is the planar Fabry−Pérot resonator. This device is made of two parallel plane mirrors separated by some dielectric material, called a '*spacer*', as in Fig.2.7a. Assuming perfectly reflective mirrors with reflectivity $R = 1$, the condition for the existence of the electromagnetic field inside the Fabry−Pérot is that of constructive interference between successive passes of a propagating wave. Thus, we require that the phase change in a round trip

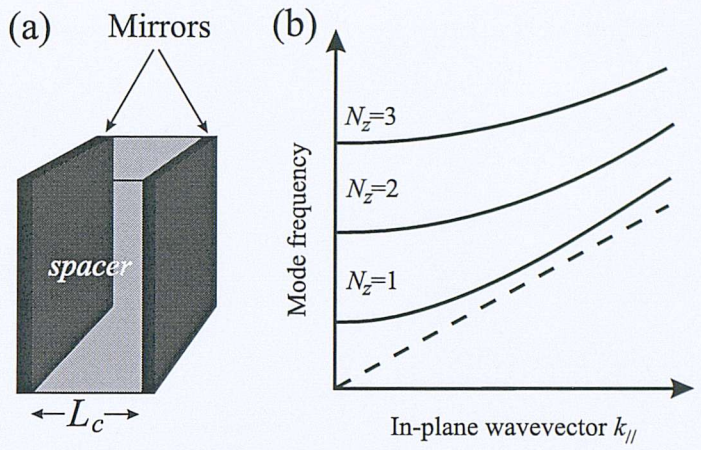

Figure 2.7: (a) A schematic Fabry-Pérot resonator. (b) The dispersion curves of a Fabry-Pérot resonator. The modes N_z=1,2,3 are plotted. The dashed line is the two dimensional free photon dispersion $\omega = ck_{//}/n_{cav}$

inside the Fabry−Pérot be equal to N times 2π

$$\left(\frac{\omega^2}{c^2}n_{cav}^2 - k_{//}^2\right)^{1/2} L_c = N\pi \tag{2.19}$$

where ω is the photon frequency, n_{cav} is the refraction index of the spacer, $k_{//}$ is the component of the photon wave vector along the Fabry−Pérot plane, and L_c is the spacer thickness. The quantity $k_z = \sqrt{(\omega^2 n_{cav}^2)/c^2 - k_{//}^2}$ is the component of the photon wave vector orthogonal to the Fabry−Pérot plane. From (2.19), it seems that inside a Fabry−Pérot the values assumed by k_z are quantized, while $k_{//}$ is still a '$free$' quantum number because of the in-plane translational symmetry of the Fabry−Pérot structure. The photon frequency as a function of the in-plane wave vector is plotted in figure 2.7b. From these dispersion curves it is evident that a cutoff frequency exists, below which there is no electromagnetic field inside the Fabry−Pérot.

Ideal Fabry−Pérot resonators with perfectly reflective mirrors are only a crude approximation of a realistic device. Mirrors have a finite transmission and a finite loss coefficient which has to be considered when describing the features of these resonators. We consider here, for simplicity, a Fabry−Pérot with two equivalent mirrors having a real (no losses), frequency independent reflection coefficient r. We further restrict ourselves to the case of light at normal incidence. Let us consider a plane wave $E_{in}(\omega, z) = E_0 \exp(ik_z z)$ incoming from outside the Fabry−Pérot. Because of the finite mirror transmission, two plane waves propagating in opposite directions will be

present inside the spacer. We write the electric field inside the Fabry–Pérot as

$$E(\omega, z) = E_0 \left[I(\omega) \exp(ik_z z) + J(\omega) \exp(-ik_z z) \right] \tag{2.20}$$

The two coefficients $I(\omega)$ and $J(\omega)$ are obtained by imposing the boundary conditions at the two mirrors:

$$I(\omega) = \frac{\sqrt{1-r^2}}{1 - r^2 \exp(2ik_z L_c)} \quad , \qquad J(\omega) = rI(\omega) \exp(ik_z L_c) \tag{2.21}$$

where k_z depends on ω according to (2.19) with $k_{//}$=0. The field strength at the center of the spacer is obtained by taking the square modulus of the electric field

$$|E(\omega)|^2 = E_0^2 \frac{1-r^2}{(1-r)^2 + 4r \sin^2(k_z L_c)} \tag{2.22}$$

From the last expression it appears that in a realistic Fabry–Pérot the electromagnetic field is not strictly quantized and, at a given angle, it is non-zero for every value of the frequency. Expression (2.22) has a resonant behaviour in correspondence with the frequencies defined by the dispersion relation (2.19), as can be seen by taking the second term in the Taylor expansion of the denominator

$$|E(\omega)|^2 \propto \frac{1}{(\omega - \omega_c)^2 + \gamma_c^2/4} \tag{2.23}$$

where $\omega_c = \pi c / L_c n_{cav}$ and

$$\gamma_c = \frac{c(1-r)^2}{L_c n_{cav} r} \tag{2.24}$$

The last expression represents the linewidth of the cavity mode resonance, and an equivalent expression will be derived for semiconductor microcavities. A quantity related to γ_c is the finesse F, defined as the ratio of the energy separation between successive cavity modes to the cavity mode linewidth, which gives a figure of merit of how close a Fabry–Pérot is to the ideal case with infinitely sharp resonances. Using (2.24) and the expression for ω_c one derives

$$F = \frac{\pi r}{(1-r)^2} \tag{2.25}$$

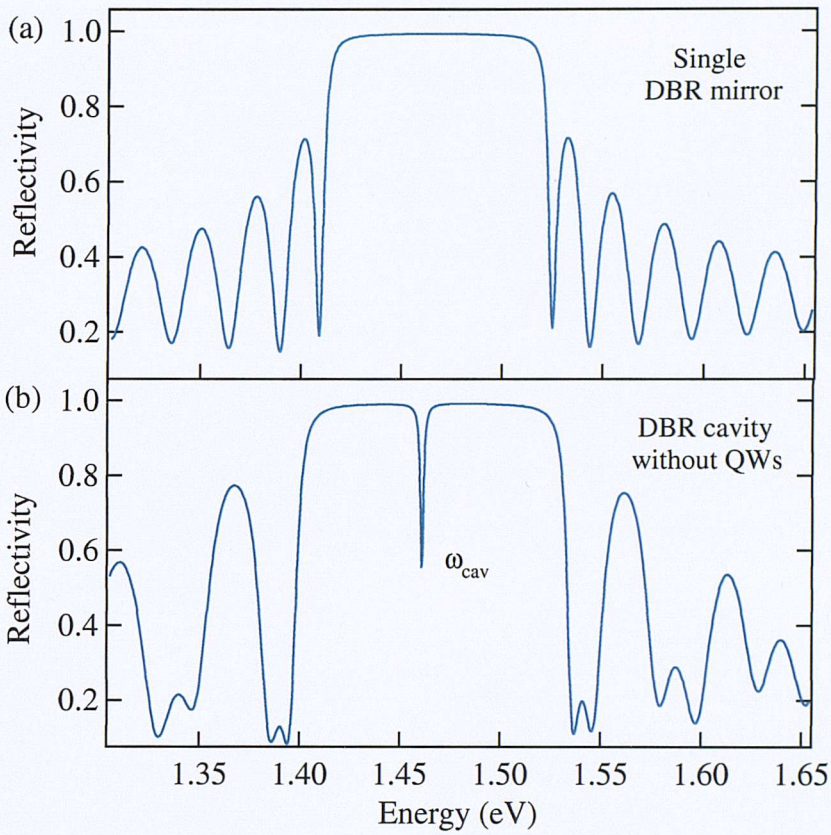

Figure 2.8: Reflectivity spectra obtained from transfer matrix model simulations for (a) a single DBR mirror, and (b) a semiconductor microcavity sample without QW's (DBR cavity)

2.2.2 Distributed Bragg Reflectors Cavity

So far, the properties of a simplified Fabry–Pérot structure has been discussed with equal mirrors having reflectivity independent of frequency. Semiconductor microcavities are essentially Fabry–Pérot resonators formed by two Bragg mirrors, which consist of thin layers of dielectric with alternating low and high refractive indices. The highest reflectivity of a Bragg mirror is achieved when the layer thickness is equal to one-quarter of the optical wavelength.[44] In this case, all Fresnel reflections add in phase and the transmission of the mirrors decreases approximately exponentially as a function of the mirror thickness or the number of alternating dielectric layers.[45, 46] These mirrors are usually called Distributed Bragg Reflectors (DBRs) due to their structure.

The reflectivity of DBRs of a specific architecture versus wavelength is usually calculated using the transfer matrix technique to solve Maxwell equations for the dielectric structure, Fig.2.8. The DBR has a high reflectivity only in a certain frequency region called 'the stop band', and the phase of the reflectivity of the DBR is π only at the center of the stop band. The central frequency of the stop band, ω_{Bragg} corresponds to a wavelength λ_{Bragg} which is defined by the fundamental periodicity of the layers

$$\lambda_{Bragg} = 2(l_1 n_1 + l_2 n_2) \tag{2.26}$$

where l_i and n_i are the thickness and the refractive index of the layers $i = 1, 2$. Each semiconductor layer is chosen to have an optical thickness $\lambda/4$. The width of the stop band is approximately given by [2]

$$\Delta\lambda_{stopband} = \frac{2\lambda_{Bragg}\Delta n}{\pi n_{eff}} \tag{2.27}$$

where $\Delta n = |n_2 - n_1|$ and n_{eff} is the effective refractive index of the mirror. For small refractive index differences n_{eff} can be replaced by the arithmetic mean of the refractive indices in the stack, otherwise the geometric mean is more suitable.[2]

Similar to the case of the Fabry–Pérot cavity, a DBR has a resonant behaviour that leads to the cavity mode linewidth

$$\gamma_c = \frac{(1-R)^2}{2\sqrt{R}} \frac{c}{(L_c + L_{DBR})n_{cav}} \tag{2.28}$$

where L_{DBR} represents the mirror penetration depth

$$L_{DBR} = \frac{\lambda}{2} \frac{n_1 n_2}{n_{cav}(n_2 - n_1)}, \qquad (n_1 < n_2) \tag{2.29}$$

where λ is the optical wavelength. In the case the DBRs are designed to have $\omega_c \simeq \omega_{Bragg}$, the resonance condition of constructive interference in a round trip is

$$\left(\frac{\omega^2}{c^2} n_{cav}^2 - k_{||}^2\right)^{1/2} L_{eff} = N\pi \tag{2.30}$$

where $L_{eff} = L_c + L_{DBR}$ is the effective cavity length. For a given mirror reflectivity, this longer optical length results in a higher frequency selectivity and thus in narrower cavity mode linewidth in comparison to a Fabry–Pérot with metallic mirrors of equal reflectivity.

2.3 Light-Matter Interaction

In this section a brief review of matter-radiation coupling is presented. Beginning with the well studied case of the atom-photon coupling, an extension to the exciton-photon coupling is derived. The physics of strong and weak coupling regime of photons with their electronic excitations is reviewed.

2.3.1 Weak Coupling Regime

The simplest case of a two level system is an excited one electron atom with two states, considered in its excited state in vacuum. The ground state $|g>$, and the excited state $|e>$ are energetically separated by $E_e - E_g = \hbar\omega$. De-excitation of the atom can be seen as a jump of the excited electron to its ground state accompanied by the emission of a photon of $E_{ph} = \hbar\omega$. In order for this process to occur, so called spontaneous emission, an electromagnetic field state of a photon at the particular energy is required to exist in space. Radiation field in space is usually described as an infinite set of harmonic oscillators, one for each mode of the radiation. The levels of each oscillator correspond to states with 0, 1, 2,..., n photons of energy $\hbar\omega$. The ground state of each oscillator has a zero-point energy $\hbar\omega/2$ so-called vacuum photon energy. In free space there is always an infinity of vacuum field states available to the radiated photon. This process can be understood as the coupling between the excited electron state and the vacuum photon field state

$$|e> \ + \ |0> \ \rightarrow \ |g> \ + \ |1> \tag{2.31}$$

The coupling of an atom to an electromagnetic field mode at its vacuum state is described by the frequency

$$\Omega_{eg} = D_{eg}E_{vac}/\hbar \tag{2.32}$$

where D_{eg} is the matrix element of the electric dipole of the atom between its excited and ground state, E_{vac} is the rms vacuum electric field amplitude of a mode of frequency ω[2]. Ω_{eg} is the frequency at which the atom and the field would exchange

[2] $E_{vac} = (\frac{\hbar\omega}{2\epsilon_0 V})^{1/2}$, where ϵ_0 is the permitivity of free space and V is the size of an arbitrary quantity volume

energy if there was only a single mode of the field, so called vacuum Rabi frequency. However, in free space the atom can emit in any mode that satisfies energy and momentum conservation. The particular mode and the time of the emission are random variables.

The probability Γ_0 of photon emission per unit time, so called Einstein coefficient A, is given by Fermi's golden rule

$$\Gamma_0 = 2\pi\Omega_{eg}^2 \frac{\rho_0(\omega)}{3} \tag{2.33}$$

where $\rho_0(\omega) = \omega^2 V/\pi^2 c^3$ is the number of modes available per unit frequency, with $V \gg \lambda^3$. The probability $P_e^{WC}(t)$ of finding the atom at the excited state after time t from its 'preparation' to that state is

$$P_e^{WC}(t) = e^{-\Gamma_0 t} \tag{2.34}$$

This exponential law describes the irreversible of the spontaneous emission in free space. The source of irreversibility is the continuum of vacuum field modes that are resonantly coupled to the atom, which act as a huge reservoir in which the atomic excitation decays away.[47] Therefore, no oscillations of the exchange energy can occur between the excited atom and the resonant vacuum field modes in free space and the described system is said to be in the weak coupling regime (WC).

In order for the exchange energy to oscillate between the excited atom and the electromagnetic field, the structure of the vacuum field modes should change to a set of discrete photon modes. This structural change of the photon modes can be achieved by the presence of a cavity. For an electric field polarized parallel to two mirrors with separation L_c, no mode exists in the intracavity space unless $\lambda = 2L_c/n, n\epsilon\mathbb{N}^*$. In the picture of a single excited atom in a cavity whose radiation field comes from an oscillating electric dipole parallel to the mirrors, there are two distinguishable cases. If the radiation field has $\lambda > 2L_c$, then the absence of any photon modes at these wavelengths inhibits the emission from the excited atom, which becomes infinitely long lived. In the other case the radiation field is resonant with the cavity photon mode then the spontaneous emission rate is enhanced. The radiative rate in a cavity

of volume V is

$$\Gamma_{cav} \cong \Gamma_0 \frac{\omega\lambda^3}{\Delta\omega_c V} \tag{2.35}$$

where $\Delta\omega_c$ is the cavity bandwidth. The spontaneous emission rate Γ_{cav} in a cavity in comparison with Γ_0 in free space is increased by a factor of $\omega\lambda^3/\Delta\omega_c V$. The alteration of an electromagnetic transition rate by modifying the surrounding of the electromagnetic field was first predicted by Purcell [17] and later on demonstrated experimentally by Drexhage.[48] This effect, the so-called Purcell effect, is the cornerstone of the present interest in microcavities.

The behaviour of an excited atom with a resonant vacuum field in a cavity (oscillatory or not) depends on the ratio of the vacuum Rabi frequency Ω_{eg} to the cavity bandwidth $\Delta\omega_c$, which is inversely proportional to the lifetime of a cavity photon, τ_c. The reciprocal of the cavity bandwidth, $\Delta\omega_c$, is the density of modes that the excited atom can interact with in the cavity, and is usually described by the quality factor $Q = \omega/\Delta\omega_c$. In a low Q-cavity, even if the spontaneous emission rate is enhanced, the emitted photon is damped rapidly before being absorbed from the atom which therefore undergoes irreversible radiative decay, like in free space. The probability $P_e^{WC}(t)$ of finding the atom in the cavity at the excited state after time t is

$$P_e^{WC}(t) = e^{-\Gamma_{cav}t} \tag{2.36}$$

This exponential law describes the irreversible of the spontaneous emission in a cavity. This is the weak coupling regime in a cavity and occurs when the interaction energy between the atom and the electromagnetic field is smaller than the cavity bandwidth, $\Omega_{eg} < \Delta\omega_c$.

2.3.2 Strong Coupling Regime

In a high Q-cavity, where $\Omega_{eg} > \Delta\omega_c$, the atom-field coupling exhibits totally different behaviour. The long living cavity photon has a high probability of interacting with the atom before it dissipates. The absorption of the cavity photon from the atom makes the spontaneous emission a reversible process, named the 'vacuum Rabi oscillation',

where the atom and its own field exchange the excitation energy with a frequency Ω_{eg}

$$|e> \ + \ |0> \rightleftarrows \ |g> \ + \ |1> \tag{2.37}$$

This is the strong coupling regime (SC) in a cavity and occurs when the interaction between the cavity photon and the atom is stronger than the spectral linewidth of the cavity, $\hbar\Omega_{eg} > \hbar\Delta\omega_c$.

In the case of N atoms in a cavity the vacuum Rabi frequency is increased as

$$\Omega_R(N) = \Omega_{eg}\sqrt{N} \tag{2.38}$$

and in the case of n photons in the cavity (resonant monochromatic excitation of an atom) the Rabi frequency becomes

$$\Omega_R(n) = \Omega_{eg}\sqrt{n+1} \tag{2.39}$$

The probability $P_e^{SC}(t)$ of finding the atom in the cavity at the excited state after time t is

$$P_e^{SC}(t) = \sum_n p(n)\cos^2(\tfrac{1}{2}\Omega_{eg}\sqrt{n+1}t) \tag{2.40}$$

where $p(n)$ is the probability of n photons in the cavity.

The strongly coupled atom-cavity system results in two new eigenstates, so called dressed states. Under resonant conditions of the atom and the cavity photon mode, the dressed states have an energy separation of $\hbar\Omega_{eg}$, named the vacuum Rabi splitting, which increases as the strength of the interaction between the atom-cavity system is increased.[42]

The N atoms-cavity system is now reminiscent to the case of N two dimensional excitons (quantum well excitons) in resonance with a photon mode of a semiconductor microcavity. In this case, the strong coupling (weak coupling) regime exists when the exciton-photon coupling constant is larger (smaller) than the exciton and cavity photon decay rates. In high finesse semiconductor microcavities, the strong coupling leads to the formation of two new eigenstates of the exciton-photon coupled

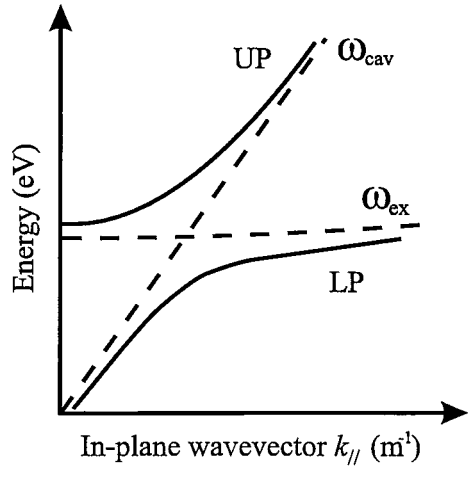

Figure 2.9: Bulk exciton-polariton dispersion of upper and lower polariton modes (*solid curves*), bare exciton and cavity modes (*dashed curves*)

system. These are called 'microcavity exciton polariton states' or simply polaritons[3]. The energy separation between the two polariton states increases as the exciton-photon coupling increases. This normal mode splitting is the solid state analog of the vacuum Rabi splitting in the atom-cavity case. In the time domain, the exciton-photon coupling makes the spontaneous exciton radiative decay process reversible, so the emitted photon is absorbed and emitted several times before it leaks out of the cavity. Thus, the emission from the strongly coupled semiconductor microcavity exhibits oscillatory behaviour, Rabi oscillations, contrary to the usual exponential decay of the weak coupling regime.

2.4 Exciton-Polaritons

In an infinite crystal, the interaction between the radiation field and excitons is characterized by translational invariance and thus wavevector conservation. A single exciton mode couples to a single radiation mode, giving rise to coupled radiation-excitation modes, the polaritons.[5] Thus, the polariton involves a spatially coherent coupling of the exciton and the optical field, which are strongly mixed close to the crossing of the bare dispersion curves.[49] Outside this crossing region, the polariton has either

[3]In this thesis the term polariton describes only the microcavity exciton polariton states unless differently specified

larger exciton content, or larger photon content. Depending on the content of exciton and photon fraction in the mixed modes, polaritons can be more exciton-like or more photon-like. Due to the energy-momentum conservation, only the excitons at the crossing of the non-interacting exciton and photon dispersions can decay, Fig.2.9. However, the exciton photon coupling leads to an anticrossing in the polariton dispersion, hence, polaritons in the infinite crystal are stationary states, and no phase space is left for the decay via radiative recombination. Their radiative decay must be associated with crystal impurities, defects, phonons, or in the realistic case of a bulk semiconductor of finite dimensions, to propagation to the crystal surface.

2.4.1 Bulk Polaritons

A quantum theory of polaritons may be obtained by using the second quantization treatment of exciton, photons, and their interaction. The exciton-photon Hamiltonian can be derived either from a microscopic model for the exciton [5, 13] or from second quantization of Maxwell's equations plus the equation of motion for the excitonic polarization [34]

$$\begin{aligned} H = &\sum_k \hbar \upsilon k \left(a_k^\dagger a_k + \frac{1}{2} \right) + \sum_k \hbar \omega_k \left(b_k^\dagger b_k + \frac{1}{2} \right) \\ &+ \sum_k iC_k \left(a_k^\dagger + a_{-k} \right) \left(b_k - b_{-k}^\dagger \right) + \sum_k D_k \left(a_k^\dagger + a_{-k} \right) \left(a_{-k}^\dagger + a_k \right) \end{aligned} \tag{2.41}$$

where $k = (\mathbf{k}, \sigma)$ is a combined index including the wavevector and the polarization vector, a_k and b_k are the annihilation Bose operators for the photon and the exciton, respectively, $\upsilon = c/\sqrt{\epsilon}$ is the speed of light in the crystal, $\hbar\omega_k = \hbar\omega_0 + \hbar^2 k^2/2M$ is the exciton energy including spatial dispersion, and

$$C_k = \hbar\omega_0 \left(\frac{\pi\beta\omega_k}{\upsilon k \varepsilon} \right)^{1/2}, \quad D_k = \hbar\omega_0 \frac{\pi\beta\omega_k}{\upsilon k \varepsilon} \tag{2.42}$$

where β is related to the oscillator strength per unit volume by

$$\beta = \frac{e^2}{m_0 \omega_0^2} \frac{f_{exc}}{V} \tag{2.43}$$

and ϵ is the dielectric function

$$\epsilon(\omega) = \epsilon_\infty + \frac{4\pi\beta\omega_0^2}{\omega_0^2 - \omega^2} \tag{2.44}$$

where ϵ_∞ represents a frequency independent contribution due to all other resonances in the crystal. The first two terms of (2.41) represent the free Hamiltonians of the exciton and photon fields. The other terms represent the exciton-photon interaction. Because of the conservation of $\mathbf{k}$ mentioned above, the Hamiltonian (2.41) can be separated into the k variable for each wavevector and diagonalized by means of operatorial transformation, called '*Hopfield transformation*'.[5] The diagonalization procedure yields the secular equation

$$\Omega_i(k)^4 - \left(\upsilon^2 k^2 + \omega_k^2 + \frac{4\pi\beta}{\epsilon_\infty}\omega_0^2\right)\Omega_i(k)^2 + \upsilon^2 k^2 + \omega_k^2 = 0 \qquad (2.45)$$

where $i \equiv UP, LP$. The resulting eigenmodes are the upper and lower polariton modes of the system, whose eigenvalues are the two solutions of the above equation, Fig.2.9.

2.4.2 Cavity Polaritons

In quantum wells, like in bulk semiconductors, polaritons give the correct description of the interaction between the exciton and the electromagnetic field. However, in a quantum well, because of the reduced dimensionality, the translational symmetry of the electronic states is broken along the confinement axis (growth direction, hereafter denoted as z axis). In this case, a two-dimensional exciton can recombine to a continuum of photon modes with all the possible values of k_z, and a finite radiative recombination rate.[13] Therefore in bare quantum wells there is no strong mixture between the exciton and photon like in the bulk case. In order to realize the two-dimensional analog of the bulk polariton a planar structure is needed, where both the photon and exciton are confined in the normal direction. Semiconductor microcavities confine the electromagnetic field by means of two parallel plane semiconductor mirrors (distributed Bragg reflectors). When a quantum well is placed inside a microcavity, excitons are coupled to the electromagnetic modes of the dielectric structure. Consequently, an exciton is coupled to a single cavity mode according to the in-plane wavevector conservation. Thus, this system constitutes the two-dimensional analog of the bulk polariton.[50] Furthermore, the finite lifetime of photons in microcavities

implies a radiative mechanism for microcavity polaritons, which in contrast to bulk polaritons is not associated with propagation and surface recombination, disorder, or impurities of the structure.

The quantum theory of a microcavity exciton-photon coupled system is based on a Hamiltonian obtained through a microscopic theory of the coupling between the quantum well exciton and the quantized electromagnetic field modes of the surrounding medium. The normal modes which diagonalize the Hamiltonian are the polariton modes. Diagonalization of the Hamiltonian is once again achieved with a Hopfield operatorial transformation.

The Hamiltonian that describes the exciton coupled to the radiation field of a quantum well embedded in a planar cavity is [51]

$$\begin{aligned} H = &\sum_{k_{//}} \left[\hbar\omega_{ph}(k_{//}) \left(a^{\dagger}_{k_{//}} a_{k_{//}} \right) + \hbar\omega_{ex}(k_{//}) \left(b^{\dagger}_{k_{//}} b_{k_{//}} \right) \right] \\ &+ \sum_{k_{//}} \left[i\hbar\Omega_R \left(a^{\dagger}_{k_{//}} b_{k_{//}} + a_{k_{//}} b^{\dagger}_{k_{//}} \right) \right] \end{aligned} \tag{2.46}$$

where $a^{\dagger}_{k_{//}}$ is the creation Bose operator of a cavity photon with in-plane wavevector $k_{//}$, and $b^{\dagger}_{k_{//}}$ is the corresponding one for a quantum well exciton, $\omega_{ph}(k_{//})$, $\omega_{ex}(k_{//})$ are the cavity photon and the quantum well exciton energy as a function of in-plane wavevector $k_{//}$, and $\hbar\Omega_R$ is the exciton-photon coupling energy. This coupling energy depends on the oscillator strength of the exciton transition and on the overlap between the cavity photon and exciton wavefunctions along the z direction.[50]

The Hopfield transformation for diagonalizing Hamiltonian (2.46) is

$$\begin{pmatrix} p_{k_{//}} \\ u_{k_{//}} \end{pmatrix} = \begin{pmatrix} X_{k_{//}} & C_{k_{//}} \\ -C_{k_{//}} & X_{k_{//}} \end{pmatrix} \begin{pmatrix} b_{k_{//}} \\ a_{k_{//}} \end{pmatrix} \tag{2.47}$$

and leads to the free polariton Hamiltonian

$$H_P = \sum_{k_{//}} \left[E_{LP} \left(p^{\dagger}_{k_{//}} p_{k_{//}} \right) + E_{UP} \left(u^{\dagger}_{k_{//}} u_{k_{//}} \right) \right] \tag{2.48}$$

where u_k and p_k are the upper and lower polariton annihilation operators and the

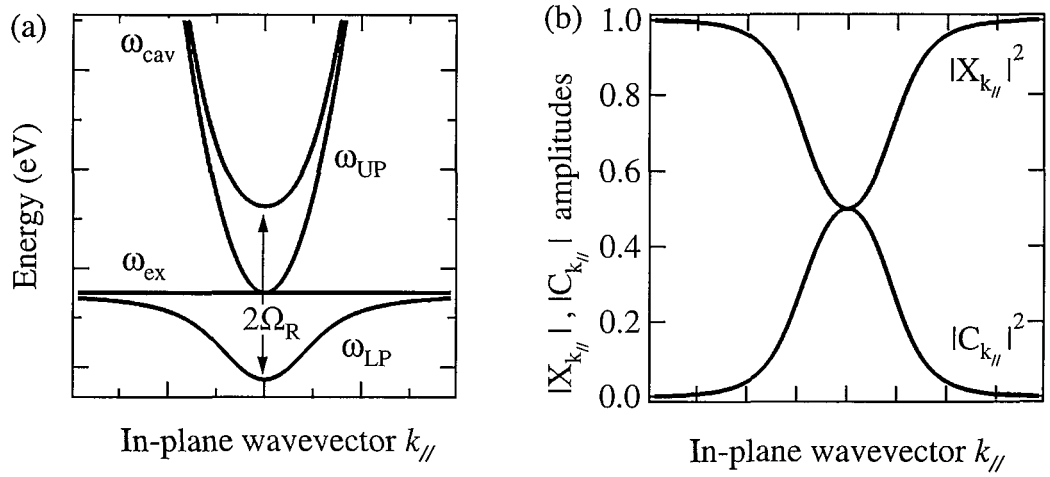

Figure 2.10: (a) Cavity exciton-polariton dispersion relations of upper and lower polariton modes (*black curves*), cavity and exciton modes (*red curves*) for $\Delta = 0meV$. (b) Bare exciton and bare cavity mode weight of upper and lower polariton modes

real $X_{k_{//}} > 0$ and $C_{k_{//}} < 0$ are given by the following expressions

$$\begin{aligned} \mathrm{X_{k_{//}}} &= \frac{1}{\sqrt{1+\left(\frac{\hbar\Omega_R}{E_{LP}(\mathrm{k_{//}})-E_C(\mathrm{k_{//}})}\right)^2}} \\ \mathrm{C_{k_{//}}} &= -\frac{1}{\sqrt{1+\left(\frac{E_{LP}(\mathrm{k_{//}})-E_C(\mathrm{k_{//}})}{\hbar\Omega_R}\right)^2}} \end{aligned} \tag{2.49}$$

Since the lower (upper) polariton operator in $p_{k_{//}} = X_{k_{//}} b_{k_{//}} + C_{k_{//}} a_{k_{//}}$ ($u_{k_{//}} = -C_{k_{//}} b_{k_{//}} + X_{k_{//}} a_{k_{//}}$), the quantities $|X_{k_{//}}|^2$ and $|C_{k_{//}}|^2$ ($|C_{k_{//}}|^2$ and $|X_{k_{//}}|^2$)represent the exciton and cavity fraction in the lower (upper) polariton mode respectively.

The energies of the polariton branches are

$$E_{UP,LP,k_{//}} = \frac{\hbar\omega_{ph}(k_{//}) + \hbar\omega_{ex}(k_{//})}{2} \pm \frac{1}{2}\sqrt{4|\hbar\Omega_R|^2 + (\hbar\omega_{ph}(k_{//}) - \hbar\omega_{ex}(k_{//}))^2} \tag{2.50}$$

For zero exciton to photon detuning $\hbar\omega_{ph}(0) = \hbar\omega_{ex}(0)$, the energy splitting between the two polariton modes is $2\hbar\Omega_R$, Fig.2.10. This quantity is the analog of the vacuum Rabi splitting in the case of strongly atom-photon coupling.[Section 2.3.2]

Chapter 3

Experimental Techniques & Samples

The experimental methods for measuring the parameters that characterize light-matter interactions are presented here. All optical characterization methods presented can be performed either as a function of wavelength, in which case we talk about frequency-resolved or spectrally-resolved spectroscopy methods, or as a function of time in which case we talk about time-resolved characterization methods. In the latter case the samples are illuminated with short pulses of light. Frequency-resolved spectroscopy needs high spectral resolution and is used mainly for probing the static features of the spectra and the effects of the environment on the different energy levels. Time-resolved spectroscopy needs high temporal resolution and is used to probe the dynamic interactions in solids.

3.1 Photoluminescence

Luminescence is defined as a non-equilibrium emission of radiation, i.e. the light emitted by a material system in excess of thermal radiation. Whereas in absorption a quantum of light is destroyed by the excitation of an electron, luminescence is a consequence of the radiative recombination of the excited electron. In competition with luminescence, other non-radiative recombination processes may occur. For luminescence to be efficient the radiative recombination must dominate over the non-radiative recombination. The dominant process for the recombination is determined

by its lifetime in the excited state since the process with the shortest lifetime wins. The quantum efficiency for a radiative transition is defined as

$$\eta = \frac{1/\tau_R}{1/\tau_R + 1/\tau_0} = \frac{\tau_0}{\tau_R + \tau_0} \tag{3.1}$$

where τ_R is the lifetime of a radiative transition and τ_0 that of non-radiative transition.

If the non-equilibrium carrier distribution in the electronic band or in the electronic states of a defective structure is obtained by irradiation with light, the radiative recombination is called photoluminescence (PL). In the present study of the optical properties of semiconductors the samples are optically excited using lamp (incoherent) or laser (coherent) light sources.

After the absorption of a photon, the semiconductor is excited and the equilibrium can be restored through several processes. If the semiconductor emits a photon directly from the excited state, the process is called photon scattering. It can be elastic (Rayleigh), where the photon is emitted at the same energy as the incident one, or inelastic (Raman) in the opposite case.

3.2 Femtosecond Pulsed & Continuous Wave Lasers

In the past decade, the advances in the field of ultrashort generation of optical pulses in laser physics have been based on the development of titanium-doped sapphire (Ti:Al_2O_3, Ti:Sapphire) as a gain medium. Different mode-locking techniques have been developed to generate short pulses with Ti:Sapphire as a gain medium.

A near transform limited 150 fs laser pulses source was employed, with a repetition rate of 76MHz and a spectral bandwidth $\sim$ 10 nm, based on the principle of self-mode-locking operation (peak power 50kW/pulse, 500mW average power, Mira 900-F, Coherent). The primary light source is an all-line blue-green argon-ion laser generating about 25 W of continuous wave (CW) emission (INNOVA Sabre Ion Laser System, Coherent) of which 8 W are used to pump the Ti:sapphire laser. For CW excitation experiments the same Ti:sapphire laser (in CW mode, peak power 400mW) and/or a tunable diode laser (tunable between 810-860nm, DC100, TUIOPTICS) with less fluctuations of the output power (peak power 60mW) have been used. The

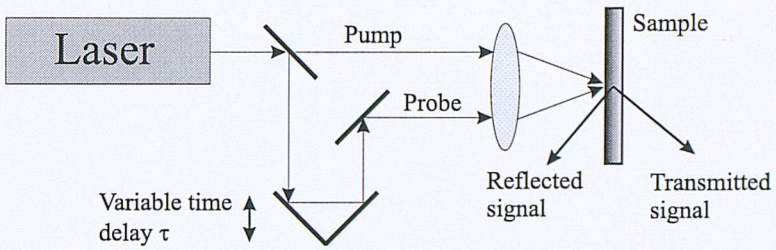

Figure 3.1: Sketch of time resolved transmission/reflection pump-probe spectroscopy

spectral parameters of the laser pulses are measured with a monochromator (Triax 550, Horiba) that uses a liquid nitrogen cooled charged coupled device (CCD) as photodetector. The spectral resolution is 0.035 meV.

3.3 Pump-Probe Technique

Pump-probe spectroscopy, when referring to reflection or transmission measurements, can be considered as a particular case of modulated reflection or transmission spectroscopy. A simple set-up for time-resolved transmission/reflection pump-probe spectroscopy is presented in Figure 3.1. The changes in the transmission or reflection of the probe pulse are measured as a function of τ, the results being displayed as differential transmission or reflection spectra, defined as

$$\Delta T/T = (T - T_0)/T, \qquad \Delta R/R = (R - R_0)/R \tag{3.2}$$

where the index '0' denotes the transmission or reflection in the absence of the pump pulse.

Pump-probe spectroscopy can be either degenerate or non-degenerate, depending on whether the pump and the probe pulses are of the same energies. In most of the experiments described in this thesis non-degenerate pump-probe spectroscopy was used, Fig.3.2. An ultrashort pulse of around 10nm[1] spectral bandwidth is split into two beams, one called '*the pump*', which excites the sample under study, and the other called '*the probe*', which monitors the changes produced in the sample due to its interaction with the pump beam. For the splitting of the two beams a variable

[1]according to Heisenberg's uncertainty principle 10nm correspond to 150 fs long pulses from $\Delta\nu \cdot \Delta t = K$, where K=0.441 for Gaussian pulse profile. [52]

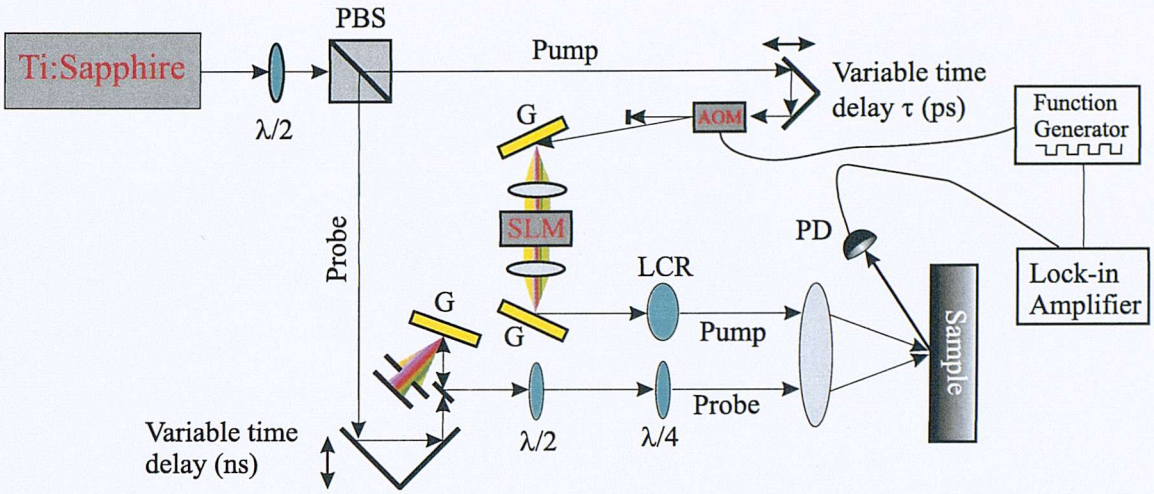

Figure 3.2: Experimental setup used in ultrafast pump-probe experiments. Grating (G), photodiode (PD), spatial light modulator (SLM), acousto optical modulator (AOM), polarizer beam splitter (PBS), liquid crystal retarder (LCR). SLM and gratings are used for spectral filtering of the pulses. AOM is driven by function generator for modulating the pump pulse in high-sensitivity lock-in detection experiments.

beam splitter was used (a combination of a half waveplate, $\lambda/2$, and a Glan-Taylor polarization beam splitter). Each beam is separately spectrally filtered, allowing for selective excitation of different polariton states.[53, 54] Two different ways of spectral filtering were employed; a computer controlled Spatial Light Modulator (SLM) [55] (with a variable slit) in combination with two (one) gratings (1200 l/mm) as depicted in figure 3.2. The SLM consists of two adjacent arrays of 128 rows/columns of liquid crystal modulators.[55] After spectral filtering, the bandwidth is reduced to $\sim$1.5meV and therefore the pulses have been elongated to a few picoseconds.

In order to scan the time delay between the pump and the probe pulses, a retroreflecting mirror is mounted on a wobbler in the pump beam path, which oscillates at a constant speed, as seen in figure 3.2, scanning a total distance of $\sim$ 2.5mm. The distance scanned by the wobbler corresponds to 6ps in a time delay scan. The time delay is scanned at a frequency of 13.3Hz. For larger changes in the time delay, a computer controlled stepper motor and an accurate worm drive are used to translate a retroreflector in the probe beam path. The time interval scanned is of a few nanoseconds. To find the approximate zero time delay, the pump-probe signal is detected on a fast photodiode. Since the pump induced changes in the transmission (or reflection) of

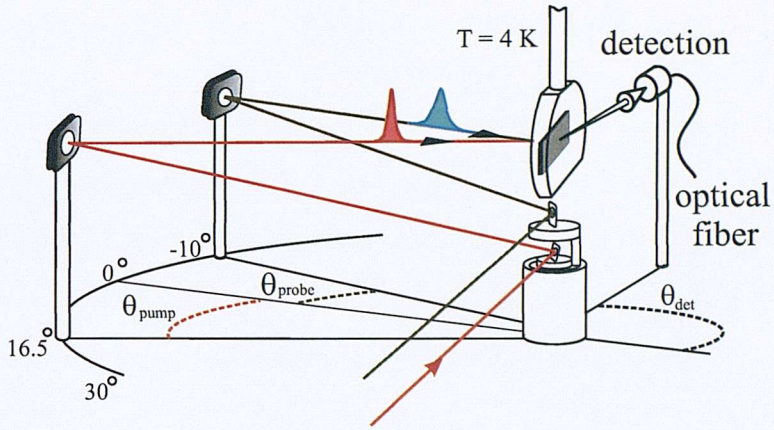

Figure 3.3: A picosecond-stable goniometer allows variation of the angle of incidence of the two beams without grossly modifying the time of arrival.[57]

the probe light are small, a phase sensitive detection was employed to decrease the noise/signal ratio. The pump pulse was modulated by an acousto-optic modulator (AOM) at a frequency of 73kHz, chosen for the minimal noise/signal ratio, Fig. 3.2. The modulation frequency was used as a reference to a lock-in amplifier which by phase sensitive detection extracts the modulated at the same frequency signal, while ignoring anything that is not synchronized with the reference.[56] In order to suppress the amplitude noise from the laser source an auto-balancing detection technique is sometimes employed, in addition to the lock-in detection, which detects a portion of the incoming probe light and subtracts it electronically from the signal to leave the induced changes dominating the laser probe noise.

Selective excitation (detection) of different polariton states in momentum space is a very powerful tool. Thus, for angularly-resolved measurements a prototype picosecond stable goniometer was employed, Fig.3.3.[57] The two arms, seen on figure 3.3, rotate along homocentric circle arcs. The samples under investigation are placed along the axis of rotation, hence the light path of the individual beams remains unchanged on a picosecond scale after rotation of the goniometer's arms.

3.4 Amplitude and Phase Spectroscoy

Amplitude and phase spectroscopy, or ellipsometry, is an optical technique, which deals with the measurement and interpretation of the polarization state of the transmitted or reflected light. The simultaneous knowledge of amplitude and phase is crucial for the complete characterization of the light-matter interaction as it can be used to disentangle the various scattering mechanisms that alter the polarization of the incident light.

Ellipsometry can be performed with continuous or pulsed excitation. In figure 3.2 the basic principles of an amplitude and phase spectroscopy setup in a pump-probe configuration are presented. Before arriving at the sample, both pump and probe beams pass through a polarizer that selects the angle of linear polarization, a $\lambda/2$ wave plate that rotates the angle of linear polarization and a $\lambda/4$ wave plate that introduces the preferred ellipticity. On the detection side, a set of a $\lambda/2$, a $\lambda/4$ and a polarization beam splitter are used to measure the three Stokes parameters [58, 59], which can fully characterize any kind of polarized light. In the case of the pump beam, the two wave plates were replaced with a liquid crystal variable retarder, which is a solid state, real-time, continuously tunable wave plate.

3.5 Semiconductor Microcavities under Study

In order to study semiconductor microcavities in the strong coupling regime it is desirable to have as narrow a cavity and exciton linewidths as possible. Both these linewidths are related to the quality of the crystal growth. The cavity linewidth is determined from mirror reflectivity, residual losses in the cavity, and by scattering with the interface roughness in the DBRs. The exciton linewidth is determined by the quantum well (QW) width and alloy fluctuations (disorder potential). In this study, two different types of microcavity QWs have been employed, one with InGaAs and one with GaAs QWs. What kind of QWs are employed depends largely on the nature of the experiment to be carried out. GaAs QWs have the advantage of smaller exciton linewidths in comparison to InGaAs QWs of the same width. On the other

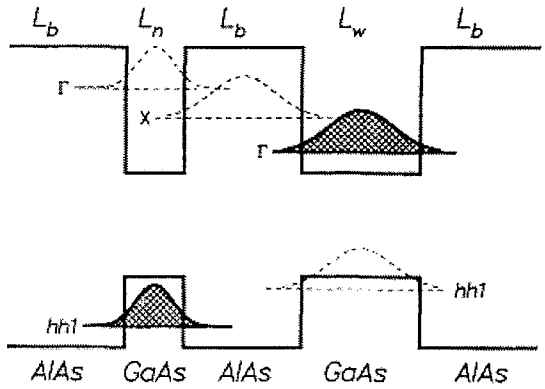

Figure 3.4: Schematic diagram showing the conduction- and valence-band edges of the MTQW structure, illustrating the relative positions of the various confined electron and heavy-hole energy levels. The hatched regions indicate the photoexcited plasmas.

hand, InGaAs have the energy of the light hole significantly shifted to higher energies by the strain in the QWs. This leads to a simplification of the spectra since when the cavity mode is in resonance with the heavy-hole exciton, the light-hole exciton remains unaffected.

Semiconductor microcavities are grown either by metallorganic vapor-phase epitaxy (MOCVD) or by molecular beam epitaxy. An important feature of their growth is the creation of a deliberate wedge by switching off the sample rotation during growth. This process leads to controlled variation of cavity thickness and thus of the cavity wavelength across the sample wafer. Therefore, by changing the position of illumination across the sample tuning of the exciton-photon resonance can be achieved. It should be noted that the exciton resonance remains virtually unaffected by the wedge in the structure.

Another parameter that opens the way for an enormous number of studies on semiconductor microcavities is the doping of the exciton's active material with mobile charges. Controllable doping of the QW in these structures can be achieved with the Mixed Type I-II QW (MTQW) architecture. A detailed study of the dynamics of the MTQW structure was performed by Galbraith *et al.*[60] Figure 3.4 shows a schematic diagram of the conduction and valence bands of a MTQW structure. It consists of two GaAs layers of thickness L_n and L_w forming two QWs separated by a barrier

layer of AlAs of thickness L_b. The thicknesses of the layers are appropriately chosen to ensure that the lowest electronic subband in each layer forms a 'staircase'. The lowest electron state is localized at Γ, in the narrow GaAs layer, the second at the X minimum in the AlAs barrier and the third again at Γ in the wide GaAs layer. This arrangement necessitates the narrow well being type II with respect to the barrier, while the wider well is type I, hence the nomenclature mixed type-I type-II QW structure.

Under laser photo-excitation with an energy below the narrow QW band gap, E_n, excitons are exclusively generated in the wide QW. However, for photo-excitation energies above the E_n, an electron hole plasma is generated above the band gap in both the narrow and wide QWs. The electron-hole plasma in the wide QW relaxes very fast into the exciton states. On the other hand, the electrons in the narrow QW thermalize by scattering via the X state in the barrier, to form an electron plasma in the wide QW leaving the holes behind in the narrow QW. The transfer from Γ to X occurs on a subpicosecond time scale [61], and the subsequent transfer from X to Γ on a submicrosecond time scale [60]. For the heavy-holes in the narrow QW the AlAs barrier is large and thus they are essentially uncoupled with heavy-holes in the wide QW. At low temperatures the narrow QW holes are able to thermalize with the wide QW only by tunneling through the AlAs barrier. If L_b is big, holes are effectively trapped in the narrow QW, producing a spatial separation between the hole plasma and the electron plasma in the wide QW.

The equilibrium carrier density for a given laser intensity depends on the hole tunneling time (AlAs barrier thickness) and results in n doping of the wide QW. Varying the laser intensity controls the electron density in the wide QW in a systematic way. Embedding this structure in a cavity, resonant with the wide QW, allows the possibility to study a strongly coupled exciton-polariton system in the presence of an electron gas of controllable density.

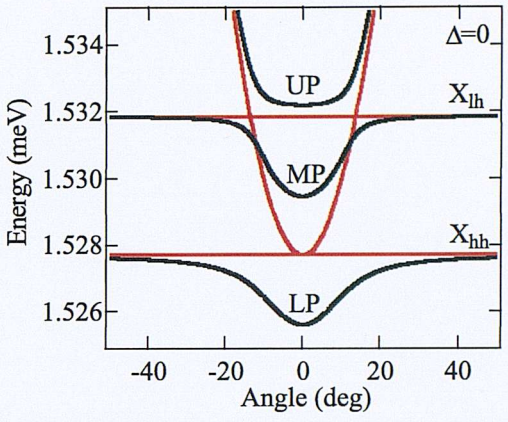

Figure 3.5: Dispersion relations of upper, middle and lower polariton modes (solid lines), cavity, X_{hh} and X_{lh} modes (dashed lines) for $\Delta = 0$

3.5.1 Semiconductor Microcavity with InGaAs Quantum Wells

The semiconductor microcavity under consideration consists of two pairs of three 100$\mathring{A}$ $In_{0.06}Ga_{0.94}As$ quantum wells (QWs) in 100$\mathring{A}$ GaAs barriers, placed between 17 (20) pairs of $GaAs/Al_{0.18}Ga_{0.82}As$ distributed Bragg reflectors (DBRs) on top (bottom). The optical cavity length is $\sim 3\lambda_{ex}/2$ and varies across the sample allowing access to both positive and negative detunings, $\Delta = \omega_{ex} - \omega_{cav}(\theta = 0)$, of the cavity resonance ω_{cav} from the exciton energy ω_{ex}.

3.5.2 Semiconductor Microcavity with GaAs MTQWs

The semiconductor microcavity structure used in this study was grown by molecular beam epitaxy on GaAs and incorporates 15 (25) periods of AlAs/AlGaAs distributed Bragg reflectors (DBR) on the top (bottom).[62] In the center of the intracavity spacer is a mixed type-I/type-II QW structure (MTQW) consisting of a single 200$\mathring{A}$ GaAs wide QW, clad on both sides by 26$\mathring{A}$ GaAs narrow QWs separated by 102$\mathring{A}$ AlAs barriers. The symmetry of the structure suppresses electric fields caused by the separation of e and h into different QWs. The optical cavity length is $\sim \lambda$ and varies across the sample. Coupling of the cavity mode with both heavy- and light-hole excitons (X_{hh} and X_{lh}) in the GaAs wide-QW results in three polariton branches (Fig. 3.5).

Chapter 4

Related Studies in Semiconductor Microcavities

This chapter is a review of studies in semiconductor heterostructures that are relevant to this thesis. The focus will be on the main experimental observations in the non-linear regime photoluminescence, the spin dynamics of polaritons, the electron-polariton scattering in semiconductor microcavities and the transition from strong to weak coupling regime.

4.1 Linear Regime Photoluminescence

In the first report of strong coupling regime in semiconductor microcavities (MCs) by Weisbuch *et al.*[18] reflectivity and transmission spectra were presented that revealed Rabi splitting between the bare exciton and photon modes in the form of anti-crossing between the coupled modes as a function of cavity detuning. Persistence of the strong coupling regime was observed up to 77K, Fig 4.1. Their structure was an MOCVD grown microcavity composed of AlGaAs/AlAs DBRs and a λ AlGaAs cavity with 76Å GaAs QWs embedded at the antinode of the photon field. This seminal publication paved the way for an enormous number of studies in the strong coupling of light with matter in systems of promising technological advances and boosted the investigations

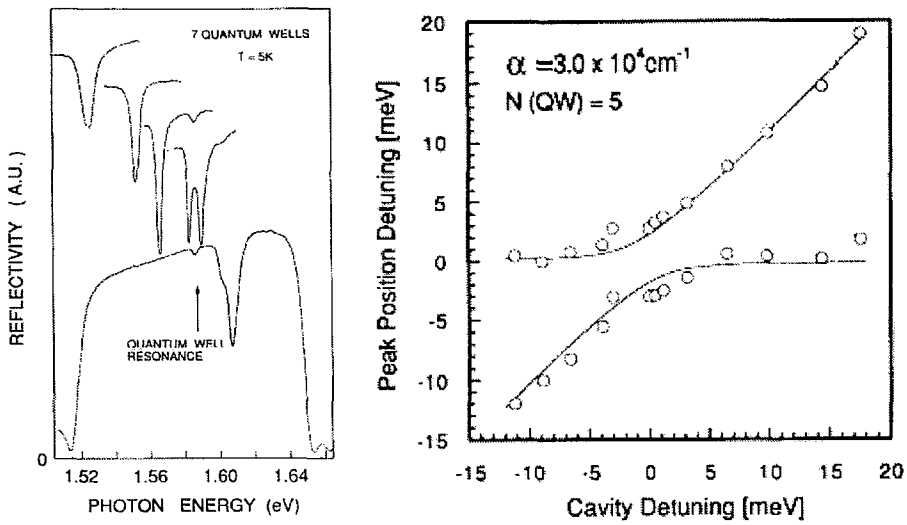

Figure 4.1: (a) Reflectivity curves for five different cavity detunings (b) Reflectivity peak positions as a function of cavity detuning

of the semiconductor community into interesting physical phenomena, such as Bose-Einstein condensation.

The positioning of the embedded QWs in microcavity structures is important for strong coupling and has been discussed in Chapter 2. Both semiclassical and quantum theory predict that for the optimum light matter coupling, QWs should be positioned at the maximum of the optical mode field. This prediction was experimentally confirmed by Zhang *et al.*[63], in an experiment in which they grew a λ MC with two kinds of embedded QWs. Four 62Å GaAs QWs were placed at the antinode of the standing wave at the center of the λ cavity and two 90Å GaAs QWs were located at each standing wave node. When the cavity mode was resonant with the 62Å QWs vacuum Rabi splitting and anti-crossing behaviour was clearly exhibited, while when the cavity mode was resonant with the 90Å QWs only a dip was observed in reflectivity spectra. The same kind of experiment was performed in a similar MC but in the weak coupling regime in a study of the Purcell effect in microcavity of structures. [64] QW emission was enhanced for the resonant condition of the QWs at the antinodes of the electric field and was inhibited for the resonant condition of the QWS at the nodes of the electric field. Finally, Frey *et al.* [65] calculated the variation of the vacuum Rabi splitting as a function of QW position in the cavity and compared the

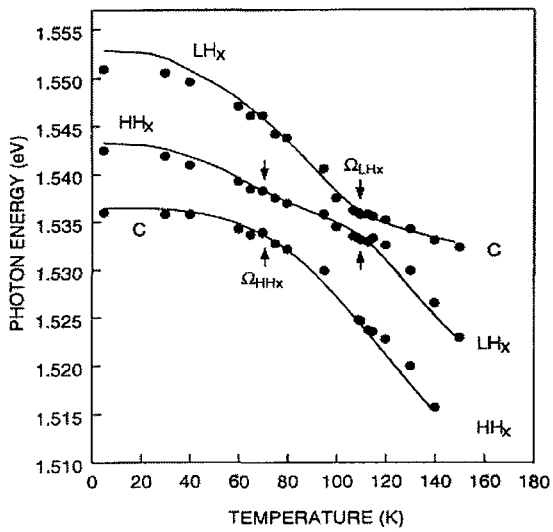

Figure 4.2: Reflectivity peak positions as a function of temperature

results with reflectivity measurements on a $\lambda/2$ cavity with two embedded InGaAs QWs.

Soon after the observation of strong coupling in semiconductor microcavities the persistence of the vacuum Rabi splitting up to room temperature was reported by Houdré *et al.*.[19] In their experiments, the microcavity was an MBE grown structure composed of AlGaAs/AlAs DBRs and a $3\lambda/2$ GaAs cavity with 75Å InGaAs QWs embedded at the antinode of the photon field. A wider linewidth of the UP mode was observed and was attributed to photon coupling to the continuum or excited exciton states (2s state). A first attempt to estimate the exciton oscillator strength was performed by fitting the reflectivity spectra into a transfer matrix simulation within the linear dispersion theory, and a fit was obtained for values of the exciton oscillator strength that were in agreement with the literature.[66]

4.1.1 Temperature Tuning

The tolerance of the strong coupling regime to elevate temperature, lead to a number of studies on the temperature tuning of the exciton-photon interaction .[67, 68, 69] The decrease of the energy band gap with the rise of temperature in semiconductors [67], results in the decrement of the exciton energy. In addition, the bare cavity mode

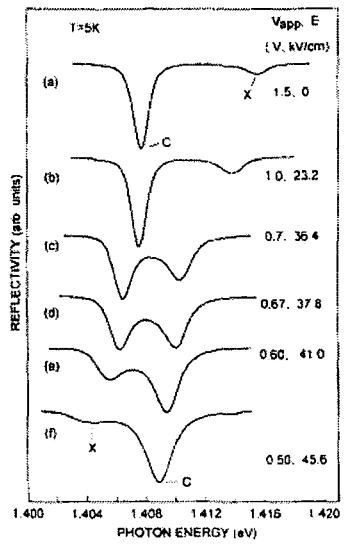

Figure 4.3: Reflectivity spectra at various electric fields. With increasing field the predominantly exciton peak (labeled X) moves closer to the cavity peak.

energy decreases due to the increase of the refractive index with the rise of temperature.[68] However, in experimental work by Fisher *et al.*[69], reflectivity measurements showed a 6.5% decrease for the exciton energy and a 1.3% decrease in the bare cavity mode for a change in temperature from 5K to 300K, (Fig. 4.2). Thus, temperature tuning proved possible and provided an effective method of tuning without the necessity of moving the probing spot position on the sample. This microcavity structure had embedded 100Å GaAs QWs that exhibited anti-crossing of the cavity mode with both the heavy and light hole excitons (X_{hh}, X_{lh} respectively). Using a standard multibeam interference analysis within the linear dispersion theory [70] for simulating the reflectivity spectra a ratio of 2.6 : 1 between the X_{hh} and X_{lh} oscillator strength was obtained in good agreement with the already measured ratio in bare GaAs QWs [71] and theoretical predictions.[66]

4.1.2 Electric Field Effects

Another way to tune the exciton-photon resonance is by introducing an electric field perpendicular to the QW. Although the presence of the electric field does not affect the cavity mode, it lowers the exciton transition energy as it forces the constituent electron

and the hole against opposite walls in the QW. This is the quantum confined Stark effect (QCSE)[72] that permits tuning of the exciton energy through the cavity mode. In addition, the exciton oscillator strength is decreased due to the reduced overlap of the electron-hole wavefunction. Thus, the exciton-photon coupling is reduced, which results in the reduction of the vacuum Rabi splitting. An electric field across the QW can be achieved by p and n doping of the top and bottom DBRs respectively, such that the cavity forms the intrinsic region in a $p-n$ junction. Fisher *et al.* reported reflectivity spectra as a function of the electric field (Fig. 4.3).[73]

In the case of symmetric MTQWs structure, as the one described in section 3.5.2, the excess electrons in the central QW forms a variable electric field with the excess holes in the outer QWs. The electric field is cancelled out at the centre of the middle QW and increases towards the outer QWs. However, for low electron densities in the central QW the amplitude of the electric field is not adequate to lower the exciton transition energy by more than the exciton linewidth.[27, 74]

4.2 Non-linear Regime Photoluminescence

Polaritons interact with each other due to their exciton fraction. Thus, the origin of polariton non-linear effects is the same as for exciton non-linear effects. Excitons are composite particles made from free electron and hole states, usually with many atoms participating. Their non-linear optical properties are exclusively due to their mutual interaction, which originates from their internal fermionic degrees of freedom. The different physical mechanisms that produce the exciton non-linear effects are the direct dipole-dipole interaction, the screening of the Coulomb interaction between two carriers by other carriers, the phase-space filling due to the Pauli exclusion principle and the exchange interaction. For a detailed review on this subject, see Schmitt-Rink *et al.*[75] Furthermore, through their photon fraction, polariton radiative lifetimes can be very fast, in the order of a few picoseconds, for mirror reflectivity around 99.9%. Therefore, microcavities are unique tunable optical systems of strong and fast non-linear responses.

4.2.1 Bosonic Properties of Polaritons

The polariton dispersion curve is steeper, in comparison to the exciton energy dispersion as a function of in-plane momentum. This results in a much lighter effective mass for the polariton, $10^4 - 10^5$ smaller than the QW exciton mass. Thus, the polariton de Broglie wavelength is much longer than the excitonic one and the density of states much smaller. As the condition for quantum degeneracy occurs when the inter-particle distances are comparable with their de Broglie wavelength, this condition can take place for a small number of polaritons per unit area. The effects of phase-space filling and screening for the constituent particles of polaritons are negligible and thus polaritons conserve their bosonic character for the polariton densities per unit area that are required for quantum degeneracy to occur. The bosonic behaviour of polaritons survives as long as the excited density is much smaller than the typical exciton saturation density. In principle, effects such as stimulated scattering and Bose Einstein-like condensation phenomena could occur at moderate excitation densities. This consideration has triggered a number of investigations on semiconductor microcavities. The goal of these investigations has been twofold: the realization of the stimulated scattering of polaritons, for the polariton relaxation into the ground state, and the observation of a Kosterlitz-Thouless phase transition, which is the analog of a non-equilibrium 2D superfluid with a Bose-Einstein condensation in degenerate boson gases.[76]

4.2.2 Polariton Stimulated Emission

Light amplification from stimulated polariton amplification in microcavities has been a very controversial subject in the past decade. The point of controversy has been whether or not the laser-like action that is usually observed in microcavities has a polaritonic or a bare excitonic nature, or otherwise, whether the emitted radiation is coming from strongly coupled or weakly coupled exciton-photon modes. Some experiments dwelt on the energy spectrum of the emission, neglecting the dispersion, which is fundamental to the nature of polaritons.

The main mechanism used to explain the non-linear emission from microcavities is

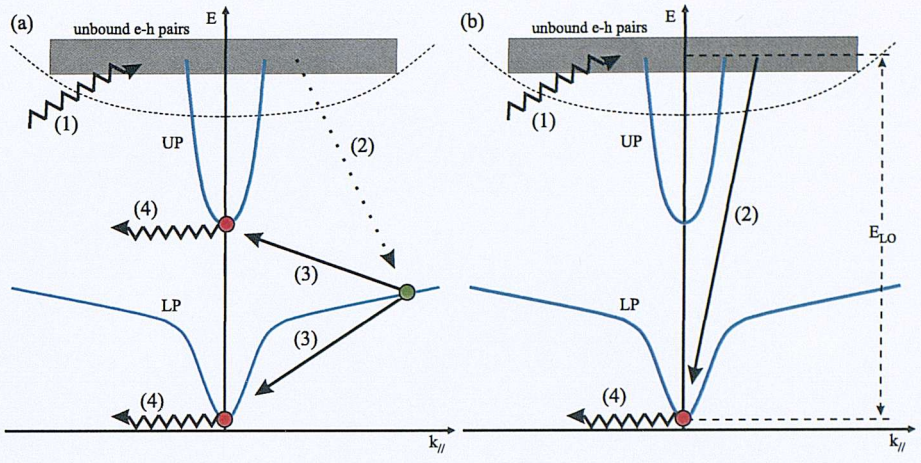

Figure 4.4: Two different versions of the proposed optical/acoustic phonon-polariton scattering, depicted on the polariton dispersion, which consist of (1a,b) non-resonant excitation of electron-hole pair, (2a) formation of hot excitons, (2b) electron-hole pairs relaxation into the lower polariton state via optical phonon emissions, (3a) exciton relaxation into two polariton states via acoustic phonon emissions, and (4a,b) photon leakage from the cavity. Dashed lines denote dispersion with no exciton-photon coupling.

the 'Boser' effect, namely, the stimulated scattering of bosons into their ground state when the ground state occupancy is greater than one. Yamamoto and coworkers [77] were first to report a 'thresholdless coherent spontaneous emission' from semiconductor microcavities. This observation was attributed to the phonon-polariton interaction, depicted in figure 4.4, and it was shown that it leads to a temperature dependent threshold behaviour.[78] In combination with the bosonic properties of polaritons, the phonon-polariton scattering was introduced as the key mechanism for a spontaneous build up of a coherent polariton population in a microcavity due to the onset of final state stimulation.[79] A threshold in the non-linear emission of the upper polariton mode as a function of the non-resonant excitation intensity was initially attributed to the onset of the boser,[78, 79] but was soon refuted as the observed optical nonlinearity could be well described as the transition from strong to weak-coupling regime.[80]

Le Si Dang and collaborators have shown that in a CdTe-based microcavity under non-resonant excitation, the luminescence intensity has a sharp threshold as a function of the pump power.[81] Confirmation that this observation was performed in the

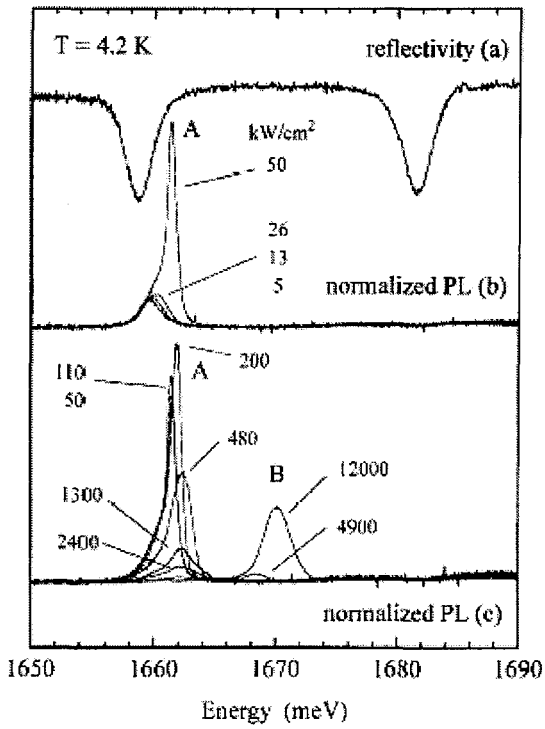

Figure 4.5: Optical measurements at 4.2 K and for zero detuning. (a) Reflectivity spectrum. (b) Photoluminescence spectra for a range of excitation densities. All spectra are normalized to the corresponding excitation densities. The A line is stimulated photoluminescence associated with the lower polariton state in the strong coupling regime. (c) Same as in (b). The B line corresponds to the stimulated emission of electron-hole plasma in the weak coupling regime.

strong coupling regime was given by the clear cut transition to the weak coupling regime for even higher excitation intensities, see figure 4.5. The spectral position of the nonlinear luminescence was blue-shifted with respect to that of the unperturbed polariton, yet it was still far away from the energy of the bare-cavity mode at which the emission in the weak-coupling regime should occur. These measurements established the existence of polariton nonlinearities, intrinsic to the strong-coupling regime. A nonlinear enhancement of the luminescence was found also by Senellart and Bloch on a GaAs/InGaAs sample under non-resonant excitation.[82] A model, including phonon assisted relaxation stimulated by the polariton final state population, was used to describe the experimental variation of the observed non-linearity amplitude and threshold as a function of detuning.

The investigations described so far, for the observation of the 'Boser' action in

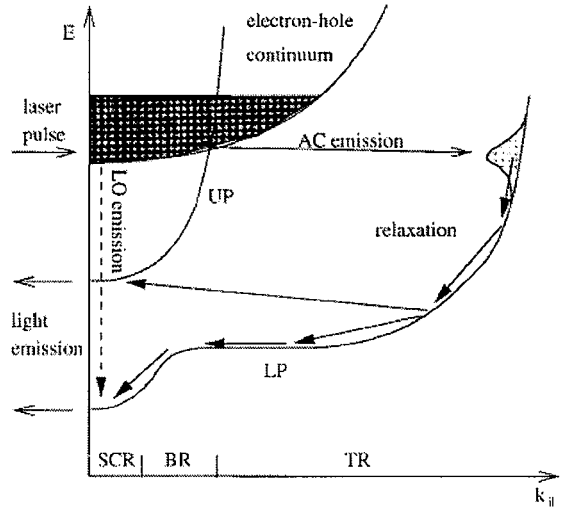

Figure 4.6: Schematic representation of the polariton dispersion, the free-carrier thermal reservoir, and the possible polariton formation processes: scattering processes by acoustic-phonon emission or absorption, and radiative recombination. UP: upper branch; LP: lower branch; SCR: strong-coupling region; BR: bottleneck region; TR: thermal region.

semiconductor microcavities had as a starting point the injection of an incoherent free carrier reservoir. A brilliant study of the polariton formation from the free carrier reservoir was performed by Tassone *et al.*[83] The bottleneck effect in the relaxation and photoluminescence of polaritons was investigated and some very important conclusions were derived; the population of the ground polariton state is not favored by an exciton-exciton scattering for excitons of $k_{//} \geq k_{\mathrm{BR}}$, see figure 4.6, nor by the acoustic phonon-polariton scattering since it cannot provide enough energy transfer for the small wavevectors needed to be exchanged. Suppression of the bottleneck effect in the relaxation of polaritons has been investigated by raising the temperature and/or the excitation intensity. In both cases, the suppression of the bottleneck is achieved by the broadening in energy of the exciton and polariton states.[83, 84, 85, 86]

However, polaritons with $k_{//} \leq k_{\mathrm{BR}}$ are well protected from scattering to wavevectors outside the region $\mid k_{//} \mid \leq k_{\mathrm{BR}}$ for the same reasons that the bottleneck effect is created. Therefore, this region, $\mid k_{//} \mid \leq k_{\mathrm{BR}}$, acts as a 'trap' for polaritons in k-space and increases their coherence time by inhibiting scattering processes. It becomes straightforward that resonant injection of polaritons into the 'trap' would be the preferred

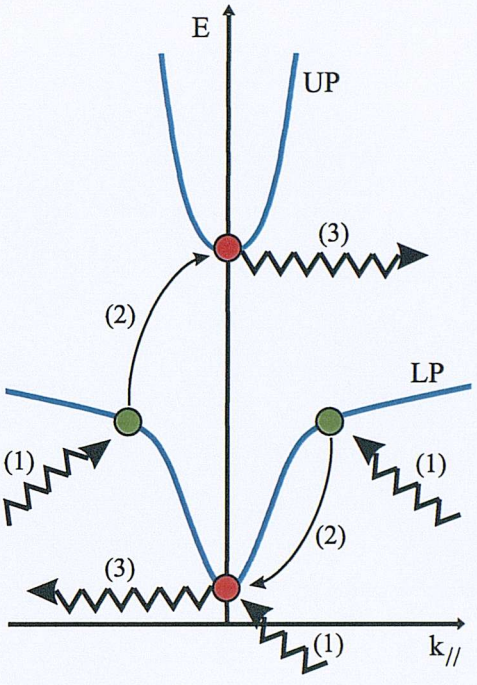

Figure 4.7: The proposed exciton-exciton scattering depicted on the polariton dispersion, which consist of (1) resonant excitation of two anti-symmetric lower polariton states and the ground polariton state, (2) exciton-exciton scattering, and (3) photon leakage from the final upper and lower polariton states.

situation for the investigation of the bosonic properties of polaritons.

The first proposition for the observation of the bosonic properties of polaritons under resonant excitation came from Tassone & Yamamoto.[87] They proposed a mechanism based on the injection of a cold exciton gas that would probe the final state stimulation of polaritons. The experimental observation of the process was performed by Huang *et al.*[88] Two resonant pump pulses were used to excite two anti-symmetric states of the lower polariton dispersion around $k_{//} = 0$. A third probe pulse was used to inject polaritons at the ground polariton state, see figure 4.7. Stimulation of the exciton-exciton scattering rate by the bosonic enhancement factor was observed from the final upper and lower polariton states at $k_{//} = 0$.

The breakthrough in the non-linear effects in semiconductor microcavities under resonant excitation came with an experiment by Savvidis *et al.*[23] In this investigation of the coherent regime, polaritons were resonantly excited by a pump laser pulse on the lower polariton dispersion curve, see figure 4.8. The excitation angle

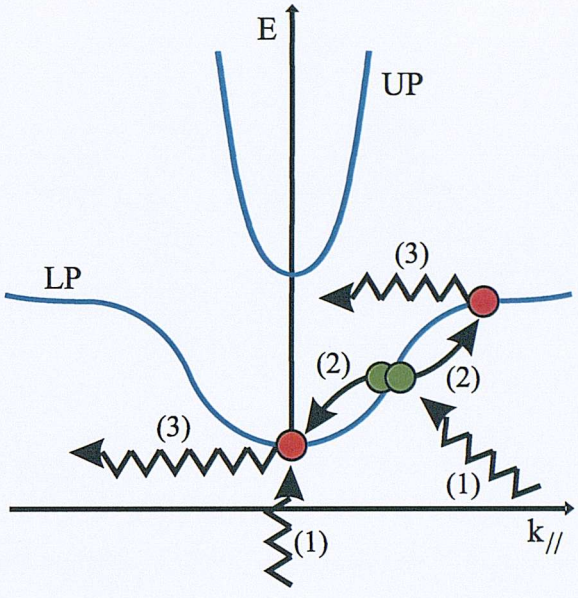

Figure 4.8: The dominant pair polariton scattering depicted on the polariton dispersion, which consist of (1) resonant excitation at the inflection point of the lower polariton branch and the ground polariton state, (2) pair polariton scattering, and (3) photon leakage from the final polariton states.

was chosen to allow energy and momentum conservation for the scattering between two polaritons, one into the ground polariton state and the other into a higher energy state ($2E_k = E_0 + E_{2k}$ has to be fulfilled, where E_k is the energy of a pump polariton injected with an in-plane wavevector k). A weak probe beam, at normal incidence to the microcavity, was used to inject polaritons resonantly at the ground polariton state. Those polaritons seeded the described scattering from the pump polaritons when pump and probe pulses were simultaneously arriving at the structure. A huge amplification of the probe beam was observed, 'the signal', accompanied by the emission from the E_{2k} state, the 'idler', as expected from the energy momentum conservation, see figure 4.8.[89] This experiment gave the most pronounced proof of polaritons bosonic behaviour to date.

This non-degenerate wave mixing process can also be seen as optical parametric amplification as the physical process is analogous to the parametric conversion of pump photons into signal and idler photons in a nonlinear crystal. The exciton content of the pump polaritons makes polariton-polariton interaction very efficient, and gains

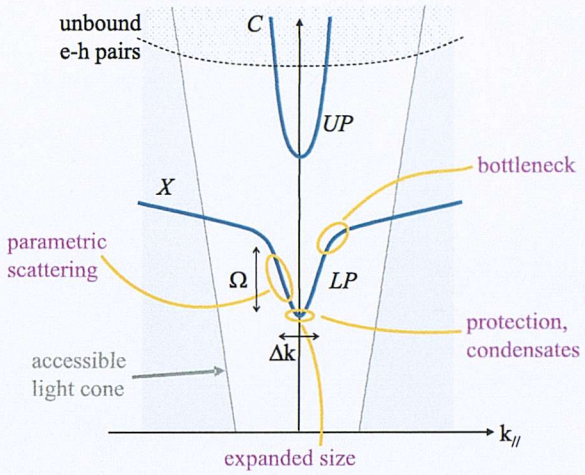

Figure 4.9: Polariton dispersion with depicted the regimes discussed in this section.

up to 4000 on the probe beam have been reported.[90] The efficiency of the process and its resemblance to the parametric conversion justifies the nomenclature 'parametric amplifier'.[91] The spontaneous relaxation of pump polaritons into the bottom of the polariton trap can trigger the parametric scattering also under continuous wave optical pumping and without an external probe.[24]

All the processes described so far have been summarized in figure 4.9. It becomes obvious that the polariton dispersion in semiconductor microcavities is a versatile system with numerous possibilities both for fundamental physics and technological advances.

4.3 Polariton Spin Dynamics

The spin dynamics of polaritons in semiconductor microcavities originate from the exciton spin dynamics in QWs,[92] discussed in section 2.1.4. The first investigations on the spin dynamics of polaritons were performed under non-resonant pulsed excitation of II-VI semiconductor microcavities.[93] Evidence of final state stimulation scattering was given by the exponential growth of the integrated emission intensity from the cavity-like states with increasing intensity. The observed complicated spin dynamics presented novel phenomena, such as the existence of a maximum at a finite time and a sign reversal of the circular polarization. This reversal was observed to be

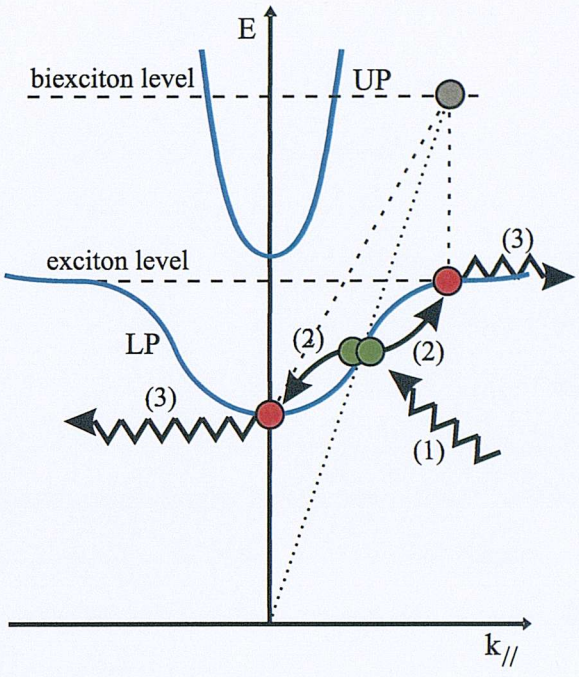

Figure 4.10: The proposed mechanism of the stimulated polariton scattering enhanced from the presence of a biexciton channel, which consist of (1) resonant excitation at the inflection point of the lower polariton branch, (2) pair polariton scattering, and (3) photon leakage from the final polariton states.

related to the sign of the splitting between the energies of the σ^+- and σ^--polarized components of the photoluminescence. The spin of the lowest photon-like energy state changed from +1 for positive detuning to -1 for negative detuning.[93] An explanation to the resolved spin dynamics was given only later,[94] based on an induced precession of polaritons pseudospins caused by an intrinsic LT-splitting of exciton-polaritons in semiconductor microcavities.[94] Under resonant excitation, the first observations on the spin dynamics of polaritons were performed in the CW parametric scattering regime, where maximum gain was observed under an elliptical pump polarization. The enhancement of the scattering was attributed to the opening of an intermediate singlet biexciton state, achievable only under elliptically polarized excitation, see figure 4.10.[95] The introduced mechanism was refuted as the observation did not exhibit a dependence on the detuning of the cavity-exciton modes, as it would have been expected if a biexciton channel was present.[96]

A complete polarization analysis in the parametric scattering regime was performed both in CW and pulsed resonant excitation.[26, 96] The dependence of the

polarization of light emitted exhibited extremely strong and unusual dependence on the polarization of pumping light. This dependence was interpreted using the pseudospin model and in the framework of a quasiclassical formalism where the parametric scattering is described as resonant four-wave mixing. It was first shown that the optically induced splitting of the exciton-polariton eigenstate, both in linear and circular polarizations, is responsible for the observed polarization effects.[26, 96] The splitting of the exciton-polariton energies in linear polarizations was soon attributed to an intrinsic longitudinal-transverse splitting in the quantum wells of semiconductor microcavities, and a microscopic model based completely on the precession of polariton pseudospins was employed to explain in a unified manner the spin dynamics of polaritons both in the non-resonant and resonant excitation regime.[94] A thorough analysis of these studies is given in Chapter 6.

4.4 Electron-Polariton Scattering

In this section, we review the effects of carrier-polariton scattering and particularly electron-polariton scattering in semiconductor microcavities. Under non-resonant excitation of the microcavity, the polariton states are populated through the relaxation of the free carriers excited by the laser. Excitons (and polaritons) are therefore formed in the presence of free carriers, which are known to be very efficient in screening the exciton and breaking it apart (on the effect of free carriers on polariton states see Houdre *et al.*[97]). It is known that the screening of the exciton is much more important in the presence of free carriers, than in the presence of an exciton population only. The presence of free carriers is therefore the main obstacle in reaching the bosonic stimulation of polaritons under non-resonant pumping. This limitation is particularly severe for GaAs quantum wells, where the exciton formation time is long compared to its radiative time and, in the steady state, the amount of free carriers is large compared to that of excitons. In other words, at equilibrium, the effective temperature is much higher than the lattice temperature.[82, 98] For II-VI materials the coupling of electrons with lattice phonons is more efficient and the carriers are more rapidly cooled down, generating excitons at a larger rate.[59, 81, 99, 100]

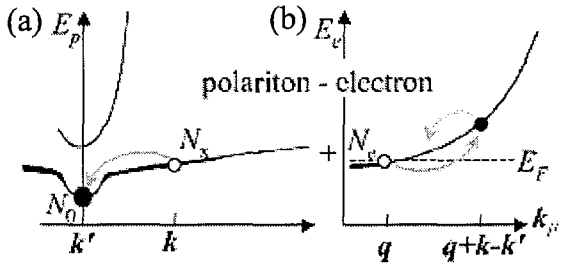

Figure 4.11: Dispersion relations of (a) upper and lower polaritons, (b) free electrons, showing the polariton-electron scattering process feeding energy into the trap at k=0. The excited carriers relax quickly preventing re-ionization.

On the other hand, apart from their detrimental screening of excitons, free carriers have a very large cross scattering section, which produces a very strong scattering interaction with excitons. Already from 1968, electron-exciton scattering has been proposed as a process that could lead to laser action in highly excited CdS. The process was studied theoretically and the results were compared with the experimental observations of the radiative recombination of highly excited CdS.[101]

In semiconductor microcavities, electron-polariton scattering was proposed recently as a very efficient mechanism for the relaxation of polaritons from the bottleneck region to the final emitting ground state with a transition time of a few picoseconds, and n-doped microcavities based on GaN materials were proposed for a new generation of optoelectronic devices based on the polariton laser, Fig.4.11.[102]

Very large changes in the population distributions of microcavity polaritons were observed, under conditions of simultaneous resonant and non-resonant excitation.[103] The strong relaxation bottleneck, which results in weak emission from the lower polariton branch for resonant excitation alone, was suppressed when additional non-resonant excitation was employed. The enhancement of the polariton relaxation was claimed to arise from scattering of polaritons by free carriers, which are present in quantum wells due to residual doping and are then heated by the non-resonant excitation.

The effect of a classical electron gas on the cavity polariton linewidths was studied experimentally in a GaAs/AlAs microcavity with an embedded quantum well that contains photo-generated electrons (at T=80 K). The linewidth dependence on the

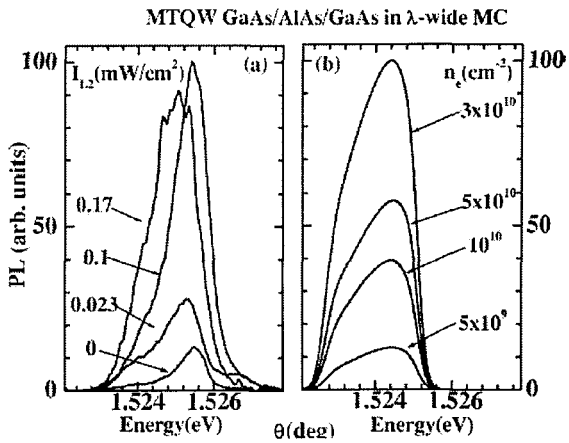

Figure 4.12: (a) PL spectra observed at T=5K and detuning δ=-4 meV. (b) PL spectra calculated for several 2DEG densities at the same δ=-4 meV.

electron density and on the cavity mode energy was explained by a theoretical model based on calculating the asymmetric bare exciton line shape, due to electron-exciton scattering.[104] On the same structure electron-polariton scattering was studied by photoluminescence spectroscopy. The photoluminescence spectra were measured as a function of the detuning energy between the cavity-confined photon and the heavy exciton and the intensity of the laser that generates the electron gas. The integrated photoluminescence intensity was shown to vary non-linearly with increasing electron density, showing a large enhancement that reached a factor of 35 over the intensity observed without an electron gas, Fig.4.12. The enhancement was compared for different detuning conditions and the photoluminescence was collected not only from the ground polariton state but from a wide range of $k_{//}$ within the polariton trap.[105]

A clear experimental observation of this process under non-resonant excitation of a semiconductor microcavity structure that allows control of the electron density and a substantial enhancement of photoluminescence from the ground polariton state was reported. It was shown that this enhancement was more effective at higher temperatures due to the different way that electron scattering processes either broaden or relax polaritons.[27] The details of this study are presented in Chapter 5.

Chapter 5

Electron Polariton Scattering

In semiconductor microcavities, electron-polariton scattering has been proposed as an efficient process that can drive polaritons from the bottleneck region to the ground state, achieving Bose amplification of the optical emission. In this chapter, the first experimental observation of this process is presented in a structure that allows control of the electron density and substantial enhancement of photoluminescence is reported. This enhancement was observed to be more effective at higher temperatures due to the different way that electron scattering processes either broaden or relax polaritons.

5.1 Electron-Polariton Scattering

Recent theoretical studies propose an electron-polariton scattering relaxation mechanism as an excellent candidate for the Bose condensation of polaritons.(Section 4.4,[25, 104]) If a population of free electrons is introduced within the active region, polaritons can be scattered from the bottleneck region to the bottom of the lower polariton (LP) branch by giving their excess energy and momentum to free electrons, as seen by solid arrows in figure 5.1a,b. The excited electrons are then rapidly cooled by the reservoir of cold electrons in the structure thus providing a 'thermal lock' for the scattered polaritons at low temperatures, as they lose the excess of energy needed to ionize the ground state polaritons.[106] Under these circumstances, polaritons at the bottom of the LP branch ($k \sim 0$) are effectively confined in the polariton trap (Fig.5.2).

The electrons facilitate rapid relaxation of polaritons because (a) charge-dipole

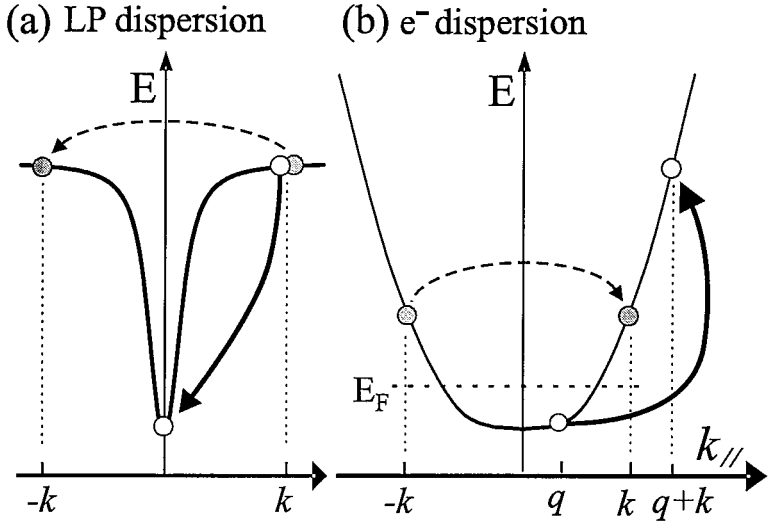

Figure 5.1: Initial and final states of electron-polariton scattering that increases the polariton population at the bottom of the trap (*solid arrow*), and for elastic scattering (*dashed arrow*), plotted on both the LP branch (a) and the electron dispersion (b).

scattering is much stronger than dipole-dipole scattering, and (b) electrons are lighter than excitons and can take away more energy for a given momentum. Since the effectiveness of the process depends on the concentration of free electrons in the active region, we use a photo-tunable n-doped heterostructure that allows for fine modulation of the free carrier density.

5.2 Experimental Configuration

The semiconductor microcavity structure used in this study has been described in section 3.5.2. The symmetry of the structure suppresses electric fields caused by the separation of e and h into different quantum wells (QWs). The strong coupling (SC) of the cavity mode with both heavy and light hole excitons (X_{hh} and X_{lh}) in the GaAs wide-QW results in three polariton branches (Fig.5.2). When a two-dimensional electron gas (2DEG) is introduced into the structure, a fourth excitonic mode appears due to the formation of trions. [74] In the current study, the trion emission has not been explicitly extracted because it appears as a very weak line, disappearing rapidly with rising temperature, in contrast to the scattering observed here. The mixed type-I/type-II QW (MTQW) structure was employed for this investigation since it

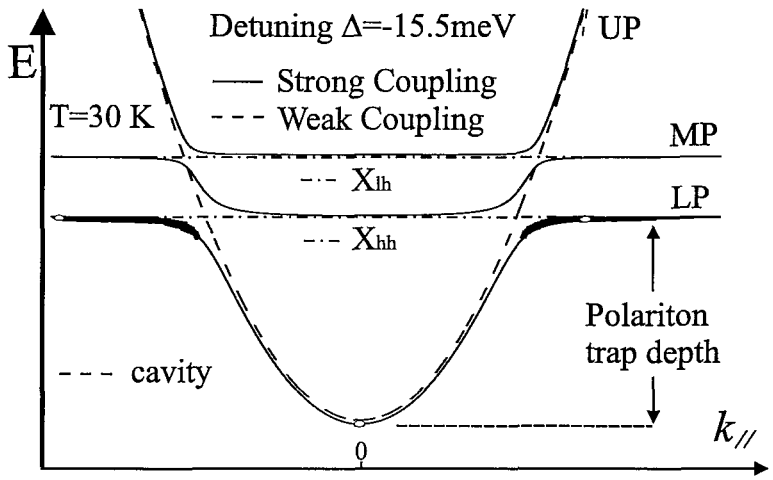

Figure 5.2: (a) Dispersion relations of upper, middle and lower polariton modes (*solid lines*), cavity, X_{hh} and X_{lh} modes (*dashed lines*) for $\Delta = -15.5meV$ and $T = 30\ K$.

allows for fine tuning of the 2DEG in the wide QW within a single sample/device. Under laser photoexcitation at photon energies below the band gap of the narrow QW, excitons can only be generated in the wide QW. However for weak laser photoexcitation with photon energies above the narrow QW band gap, an electron-hole plasma is excited both in the wide QW and in the narrow QW. The MTQW architecture allows for efficient resonant transfer of electrons from the narrow QW to the wide QW through the X-valley of the barrier layer, while holes are trapped in the narrow QW by the absence of these resonant states. This configuration provides an efficient way to repeatably vary the exciton and electron densities in the wide QW. In this study a continuous wave (CW) Ti:S laser at 1.557eV exclusively excites the wide QW and a diode laser at 1.952eV varies the electron density, n_e. The Ti:S laser is set to excite the cavity mode quasi-resonantly, i.e. at high angles and energies above the polariton region. Although the exciton density is accurately estimated from the intensities of the Ti:S laser, I_X, and the diode laser, I_n, the exact dependence of n_e on the intensity of the diode laser is not known. The range of injected n_e used in this study is estimated to be $0 < n_e < 10^{12}\text{cm}^{-2}$ according to previous studies that assumed a linear dependence $n_e \propto I_n$, although more recent calculations predict a non-linear behaviour.[62, 104] Therefore, instead of using n_e, all dependencies are expressed as a function of the diode laser intensity.

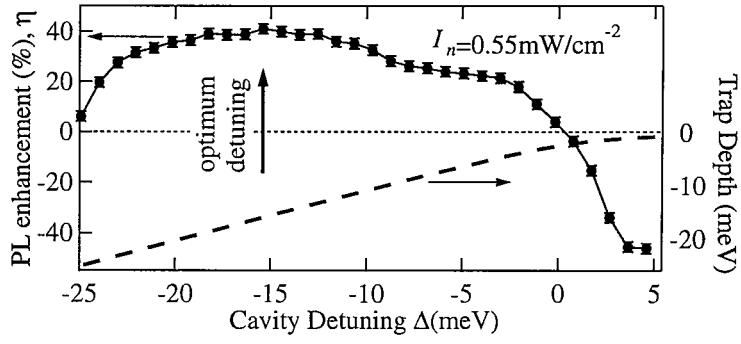

Figure 5.3: Photoluminescence enhancement of the lower polariton mode (*solid line*) and polariton trap depth (*dashed line*) as a function of the cavity detuning energy.

5.3 Resonance Dependence

Photoluminescence (PL) spectra were taken at normal incidence (i.e. in-plane $k = 0$), for T = 5K to 30K and at low excitation powers of both wide and narrow QWs to preserve SC. The emitted light was collected in a cone of $\pm 0.15°$. Under these conditions the PL from the lower and middle polariton branches is modified by introducing a 2DEG in the wide QW. This change of PL varies from enhancement to suppression depending on the exact resonance of the cavity mode with the X_{hh}, Fig.5.3. The detuning dependence was performed under a fixed moderate n_e in the wide QW and at a temperature of 30K in order to avoid any effects from charged exciton states. For each illumination spot, the measured photoluminescence enhancement $\Delta PL = [PL(I_X + I_n) - PL(I_n)]$ (with respect to the lowest power photoluminescence measured) was normalized to the absorbed power of the wide QW, and $\eta = 100\% \times \Delta PL/[PL(I_X) + PL(I_n)]$ was calculated. It is evident that for a wide range of negative detunings the presence of a 2DEG is beneficial to the PL. This implies that whenever the polariton trap is deeper than a few meV (and thus the relaxation bottleneck is present on the LP branch), electrons enhance the scattering from the bottleneck region to the ground state at k=0, Fig.5.3. The detuning dependence of the PL enhancement follows the same trend independently of the temperature, as long as the system remains in the SC regime. This independence arises because the shape of the LP branch remains virtually unaffected with increasing temperature.

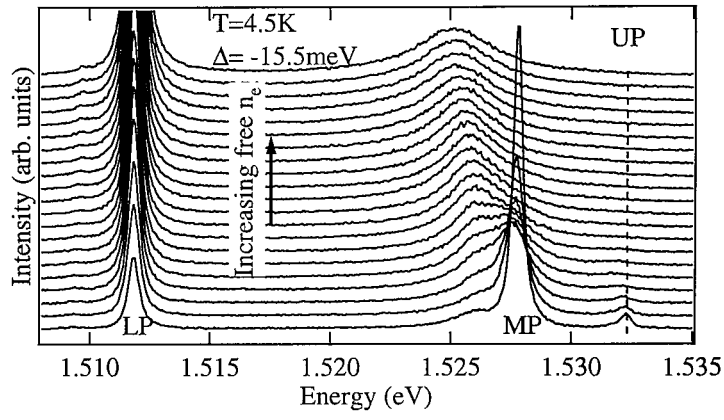

Figure 5.4: Photoluminescence spectra for different free electron densities n_e (n_e increases upwards).

5.4 Electron Density Dependence

In order to reveal the extent of this enhancement, ΔPL was measured as a function of the electron density for a range of different detunings. With the cavity mode optimally detuned from the X_{hh} ($\Delta = -15.5$meV), the normally-emitted PL spectra were recorded in figure 5.4 as n_e increases (upwards). Here the weak Ti:S pump, $I_X = 20\text{mW cm}^{-2}$, only excites exciton densities of $n_X \simeq 4 \times 10^9\text{cm}^{-2}$ (assuming $\tau_X \sim 500ps$). With free electrons injected into the wide QW, the polariton modes are drastically modified as a result of electron-exciton scattering. The PL intensity of the LP mode increases rapidly, (Fig.5.5a), while the PL from the middle polariton (MP) mode conversely decreases. However, increasing n_e also systematically broadens the MP mode and red shifts its peak energy position, Fig.5.5b. The sublinear enhancement follows $\sim I_n^{0.6}$ below a critical diode power, I_n^{sat} (regions I and II), above which the slope reduces to $\sim I_n^{0.4}$ (region III). To understand the nature of this threshold note that the red shift of the MP mode energy towards the bare X_{hh} energy marks a different critical diode power, I_n^{WC}, at which the system passes from the strong coupling (region I) into the weak coupling (WC) regime (regions II and III). The dependence of the PL enhancement on I_n remains *virtually unaffected* by this transition to the WC regime. This is due to the negligible difference in the shape of the LP branch between the SC and WC regimes at these negative detunings Fig.5.2. Even

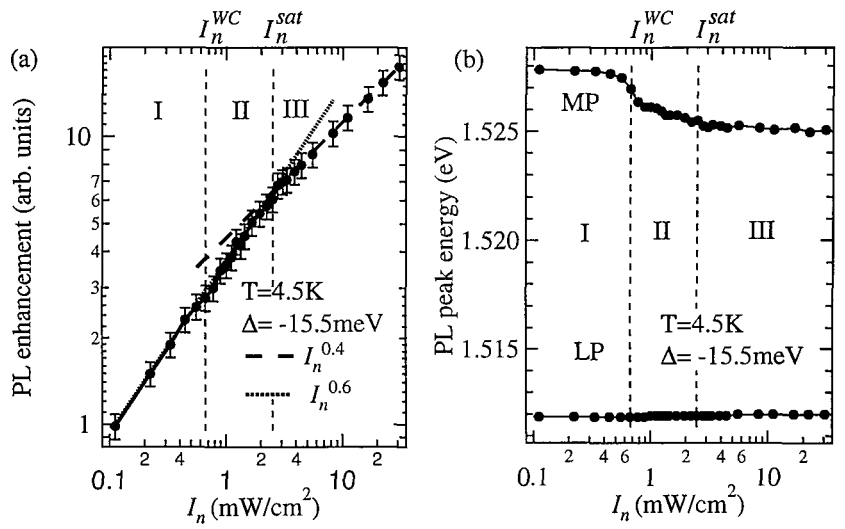

Figure 5.5: (a) PL enhancement vs. I_n for $\Delta = -15.5$meV at $T = 4.5$K. Vertical dotted lines separate the three different regions that correspond to the strong coupling regime (I), weak coupling regime (II) and ionized excitons (III). (b) Peak PL emission energies for the lower and middle polariton branches vs. I_n.

in the WC regime, the lower cavity mode is weakly coupled to the bare exciton and the bottleneck in relaxation remains. In structures with a small Rabi splitting (here only 4meV), the transition to the WC regime occurs for moderate exciton or electron densities and therefore without substantially collision-broadening the exciton transition, so that excitons remain well defined states. Electron-exciton scattering thus exhibits similar properties in both the SC and WC regimes.

The rate of PL enhancement decreases only after the electron density becomes high enough (at I_n^{sat}) to dissociate the excitons in the wide QW, $n_e > 10^{11}$cm^{-2}. To confirm that a separate contribution to the PL enhancement indeed exists when the excitons are ionized, measurements are shown for another detuning condition ($\Delta = -1.5$meV) at which the SC and WC dispersion relations vary considerably, but for which a low n_e still enhances the LP mode emission, Fig.5.3. The PL enhancement with I_n shown in figure 5.6a is again separated into three regions. The first vertical dashed line corresponds to the transition from the SC to the WC regime, as identified from the shift of the peak energy positions. For this small negative detuning the LP branch and the bare cavity mode differ greatly, unlike the situation at very negative detuning. Therefore, for a wide range of n_e (regions I and II) the excitons are still

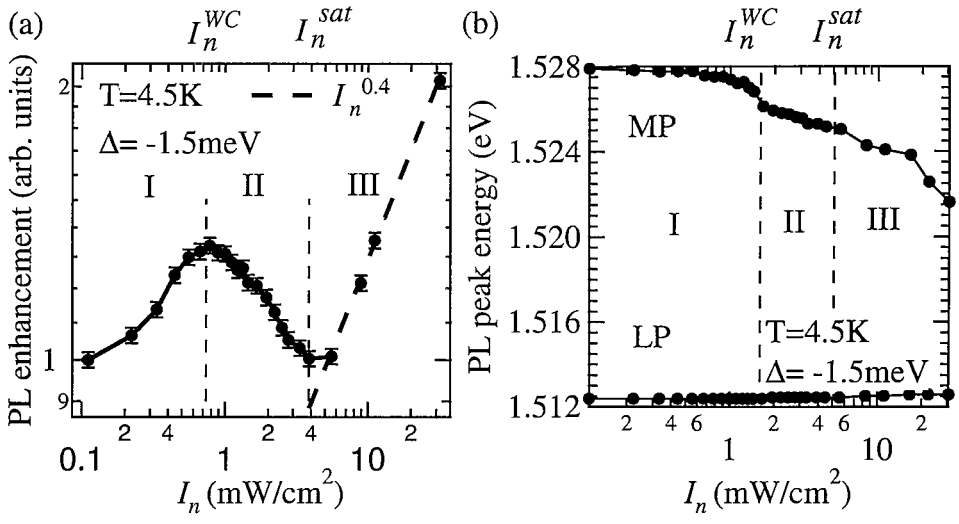

Figure 5.6: (a) PL enhancement vs. I_n for $\Delta = -1.5$meV at $T = 4.5$K. Vertical dotted lines separate the three different regions that correspond to the strong coupling regime (I), weak coupling regime (II) and ionized excitons (III). (b) Peak PL emission energies for the lower and middle polariton branches vs. I_n.

well-defined quasiparticles and electron-exciton scattering is a well-defined process. In this case, when the system enters the WC regime, ΔPL changes behaviour because the LP and the bare cavity mode now have different shapes. However in region III, the enhancement in emission is once again sublinear with the same exponent as for the optimum detuning, $\Delta PL \propto I_n^{0.4}$. This confirms that region III indeed corresponds to the screening out of the bound exciton and that the recombination of the electron-hole plasma in the wide QW depends on the excess electron density, independent of detuning.

5.5 Temperature Dependence

Although an enhancement in the PL at k=0 is seen at T=4.5K, it is limited to a factor of two within the SC regime. One of the main reasons for this is that the extra homogeneous broadening of the exciton transition produced by injecting the 2DEG leads to a rapid reduction of the exciton oscillator strength and the transition to the WC regime. However, it is noticed that this relationship between PL enhancement and exciton broadening produced by the electron-polariton scattering is considerably

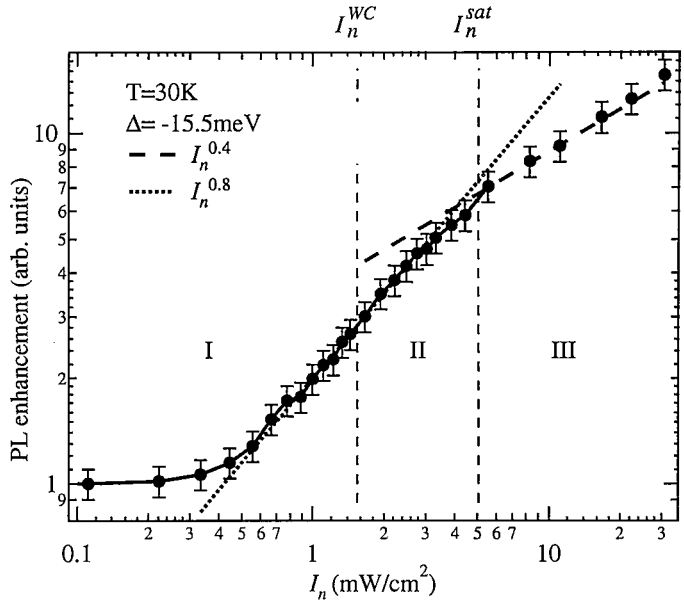

Figure 5.7: PL enhancement vs. I_n for $\Delta = -15.5$meV at $T = 30$K. Vertical dotted lines separate the three different regions that correspond to the strong coupling regime (I), weak coupling regime (II) and ionized excitons (III).

affected by temperature. The electron-induced PL enhancement at T=30K and the optimum resonance condition (Δ=-15.5meV) is shown in figure 5.7.

In this case, the PL enhancement turns on only after a larger diode power and similarly, both the transition to the weak coupling, $I_n{}^{WC}$, and the exciton unbinding, $I_n{}^{sat}$, are shifted to higher diode power (by a factor $\sim$ 2.5). This would suggest that electron-polariton scattering is *reduced* at higher temperatures as predicted by recent theoretical calculations.[104] At the same time, in the strong coupling regime the enhancement of PL by electrons is more rapid, $\Delta PL \propto I_n^{0.8}$, implying that the electron-polariton scattering rate is *larger* at higher temperatures (discussed below). Within the SC regime this immediately results in a threefold enhancement of PL due to electron-polariton scattering compared to PL emitted without photo-injecting electrons into the wide QW. Once again, in the plasma regime the dependence on I_n remains unchanged with temperature for the reasons discussed above. However, before the excitons are ionized, a 10-fold enhancement is achieved.

The smaller contribution to exciton broadening by electrons, at higher temperatures, is confirmed by plotting the linewidth of the (mostly X_{hh}-like) MP mode vs.

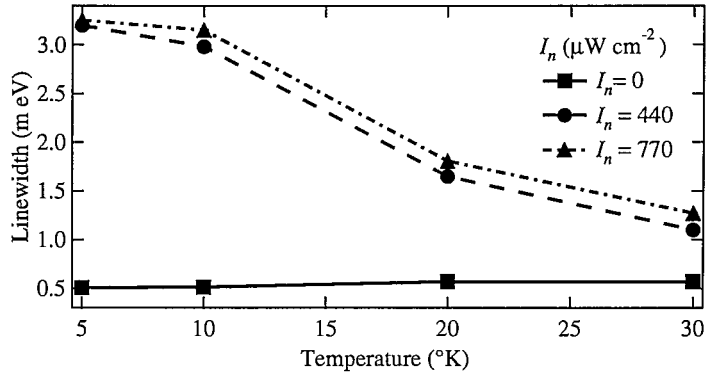

Figure 5.8: Linewidth (FWHM) of middle polariton mode as a function of temperature at several I_n.

temperature at low n_e (Fig.5.8). This observation agrees with calculations of the electron-exciton interaction matrix elements, which favor small energy transfer transitions, as seen in figure 5.1 on both electron and polariton dispersions with dashed arrows.[104] Essentially, as the exciton temperature increases, energy-momentum conservation reduces the range of final states that electrons can scatter excitons into, and decreases the strength of this scattering. Consequently, the higher the temperature, the less effective electrons will be in the electron-exciton scattering interaction. This would indeed mean that a larger electron density is needed both to reduce the exciton oscillator strength enough to pass over to weak coupling, and also to ionize the excitons, in agreement with the increase in both I_n^{WC} and I_n^{sat} at T=30K.

5.6 Underlying Mechanism

To understand how the efficiency of electron-polariton scattering (observed in enhanced PL) *increases* despite the drop in electron-exciton scattering at higher temperatures, one needs to understand the very different scattering processes participating. As depicted in figure 5.1, the scattering of an exciton from the bottleneck region to $k \approx 0$ implies a small exchange in wavevector but a large exchange of energy. This exchange favors electrons with initial states of higher energy/wavevector as found at higher temperatures. This effect is thus not in contradiction with the previous

analysis since it implies that only the specific scattering rate (into the $k_{final} \approx 0$) becomes faster while the scattering contribution to the exciton linewidth involves all final states.

A number of approximations are made in this model. The present phenomenological approach neglects the effects of bound charged excitons states. However, recent calculations show that trion dissociation operates in a similar manner to the free particle scattering presented here.[104] Trion-mediated scattering will therefore contribute in the same way as electrons at low temperatures, but should be absent above T=10K due to their ionization. In addition, the effects of both exciton and carrier localization have been ignored. This is a valid approximation for samples that are of high quality. In particular, the sample under investigation has polariton linewidths eight (8) times smaller than the Rabi splitting, which justifies the approximation.

5.7 Conclusions

This chapter thus presented evidence for the effectiveness of electrons within the active region of a strongly-coupled semiconductor microcavity, for enhancing relaxation of polaritons. This matches recent theoretical predictions. Understanding the ways that electron-exciton Coulomb scattering contributes differently to exciton broadening and photoluminescence enhancement paves the way to improved polariton emitters and lasers.

Chapter 6

Spin Dependence of the Parametric Amplifier

As already discussed in section 4.2.2, strong angular asymmetries are observed in the photoluminescence [85, 89, 107] produced by parametric scattering between polaritons with different in-plane momentum and energy. Strong nonlinearities in the emission are produced when this scattering is externally stimulated by seeding the final polariton state. This process has been shown to provide extremely strong gain $\sim 10^6$ cm^{-1}, building up substantial polariton populations in the lowest energy states, which emit normally from the sample. In previous studies, parametric scattering was found to be strongest when the spin of the interacting quasiparticles was identical.[23] Recent CW measurements conversely show that elliptically-polarized pumping produces stronger emission, however it remains unclear what processes can be involved.[95] In this chapter, a comprehensive analysis of the polarization dynamics of the light emitted from microcavity samples, which are resonantly pumped at a critical angle to the normal is given in order to reveal the underlying spin dynamics of the parametric polariton amplifier.

6.1 Experimental Configuration

The semiconductor microcavity used in this study is described in section 3.5.1. The sample was held in a cold-finger cryostat at a temperature of 10 K. The strong coupling of exciton and cavity modes produces two new polariton branches of which only the

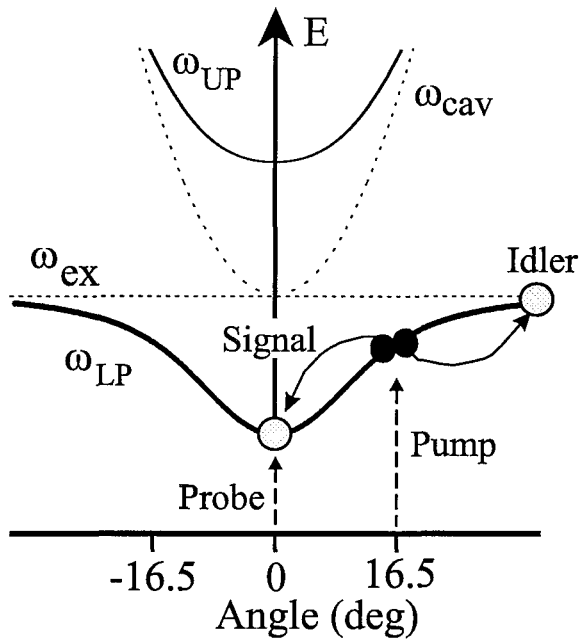

Figure 6.1: Dispersion relations of exciton (ω_{ex}), cavity photon (ω_{cav}), upper (ω_{UP})and lower (ω_{LP}) polaritons, showing the dominant pair scattering for pump polaritons.

$\smile\!\!\!\frown$-shaped lower polariton dispersion ω_{LP} is of concern here, Fig.6.1. Each branch is doubly spin degenerate ($J = \pm 1$) due to the heavy hole exciton, with circularly polarized light of each helicity able to couple to one spin only, as discussed in section 2.1.4. Thus one can simply track polariton spins using polarization analysis of the emitted photons.

In order to track the spin dynamics of the parametric scattering mechanism the measurements were performed in a regime which shows strong stimulated gain.[23] Pulsed experiments allow one to disentangle the different scattering processes, while remaining below threshold for parametric oscillation. A pump pulse, incident at the critical angle of 16.5° injects polaritons at the point of inflection on the dispersion relation, and a normally-incident probe pulse seeds polaritons with zero in-plane momentum, Fig.6.1. This seed is amplified by over two orders of magnitude, producing emerging beams at 0° ('signal') and 35° ('idler'). The incident pulses are derived from a 100fs mode-locked Ti:sapphire laser and are separately spectrally filtered inside zero-dispersion grating compressors in order to selectively excite the lower polariton branch. The polarization of each 3ps pulse is set by wave plates, and arranged to

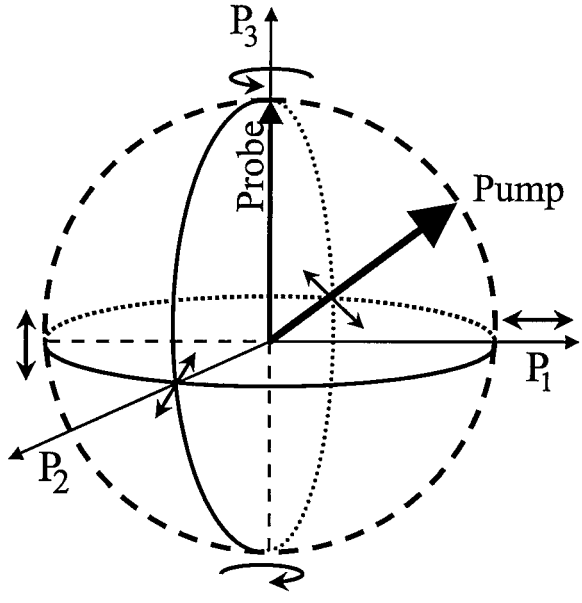

Figure 6.2: Poincaré sphere, representing polarizations: right/left circular at $P_3 = \pm 1$, and linear around the equator, $P_3 = 0$. In experiments, the probe has always $P_3 = +1$, while the pump follows the dashed meridian.

compensate Fresnel losses at the sample surface.

Throughout the experiment the polarization of the probe pulse is kept right circular whereas the pump polarization is rotated from right- to left-circular hence varying linearly the relative spin populations of the pump-injected polaritons while keeping the pump intensity constant. This polarization selectivity in the pulsed domain allows the details of the Coulomb dipole-dipole scattering process to be accurately investigated.

Analysis of each polarization state using the three Stokes parameters, was performed in order to keep track of the polarization of the different injected and emitted beams. The Stokes parameters correspond to the following polarization degrees:

$$P_1 = \frac{I_{\updownarrow} - I_{\leftrightarrow}}{I_{\updownarrow} + I_{\leftrightarrow}}, \; P_2 = \frac{I_{\nearrow} - I_{\searrow}}{I_{\nearrow} + I_{\searrow}}, \; P_3 = \frac{I_{\circlearrowright} - I_{\circlearrowleft}}{I_{\circlearrowright} + I_{\circlearrowleft}} \tag{6.1}$$

where $I_{\updownarrow,\leftrightarrow,\nearrow,\searrow}$ are the intensities of linear components at $0°, 90°, \pm 45°$ to the horizontal, and $I_{\circlearrowright,\circlearrowleft}$ are the circular components. In this way, any polarization state can be expressed as a vector in the orthogonal basis of Eq.6.1 and can be projected in the 3D polarization space, also known as the Poincaré sphere, as figure 6.2 shows. Calculation of the evolution of the three Stokes parameters is performed by three

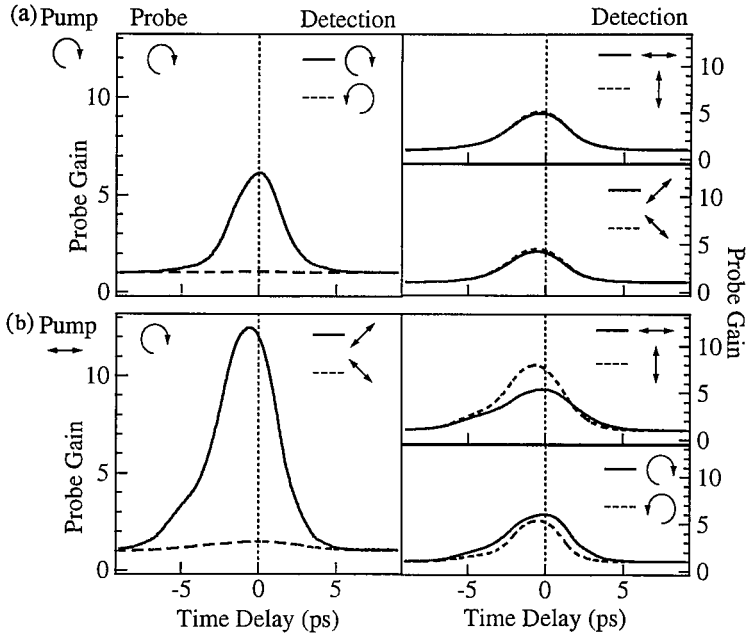

Figure 6.3: (a,b) Emitted signal for (a) co-circular pump and probe, and (b) linear pump and circular probe, as a function of their time delay, polarization analyzed as specified.

independent measurements that correspond to the three orthogonal axes of the Poincaré sphere. The signal (**S**) and idler (**I**) Stokes vectors are extracted by judicious settings of $\frac{\lambda}{2}, \frac{\lambda}{4}$ plates and a polarizing beam splitter as a function of the ratio of injected spin-up to spin-down polaritons, which is set by the pump circular polarization degree

$$\rho = P_3 = \frac{I_{\circlearrowleft} - I_{\circlearrowright}}{I_{\circlearrowleft} + I_{\circlearrowright}} \tag{6.2}$$

6.2 Polarisation Dependence in the Pulsed regime

If circularly-polarized pulses are used to inject polaritons of one specific spin, stimulated gain of the probe polaritons is seen only for co-circularly polarized pump and probe near zero time delay, Fig.6.3a. In this case the emitted signal is completely circularly-polarized indicating the absence of significant polariton spin-flips within their 3ps radiative lifetime. However, when the pump pulse is horizontally polarized

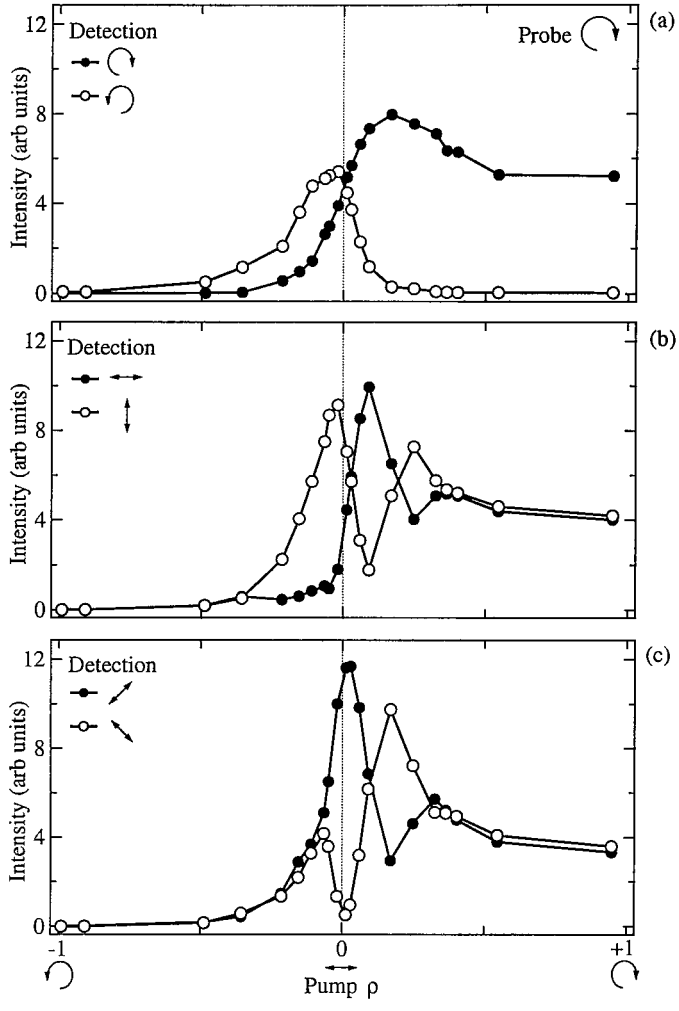

Figure 6.4: Intensity of signal emission, decomposed into (a) circular, (b) linear and (c) linear diagonal polarizations, as a function of the pump circular polarization degree. The probe is σ^+ polarized.

which injects equal populations of spin-up and spin-down polaritons, the emitted signal is linearly polarized at 45°, Fig.6.3a,b. Moreover, the gain is nearly twice as large for this configuration even though the density of polaritons with the same spin as the probe is halved. Despite the large variation in gain magnitude in these two cases, the speed of response is very similar and the gain is maximized at the same (within 1ps) pump-probe time delay, Fig.6.3a,b. To explore this phenomenon in more detail, figure 6.4 plots the intensity of each polarization component as a function of the pump circular polarization degree, ρ, which corresponds to the ratio of spin-up to spin-down polaritons injected (termed the *net spin* injected). The total gain is maximized for linear pump ($\rho = 0$), while to maximize emission from the spin-up seeded

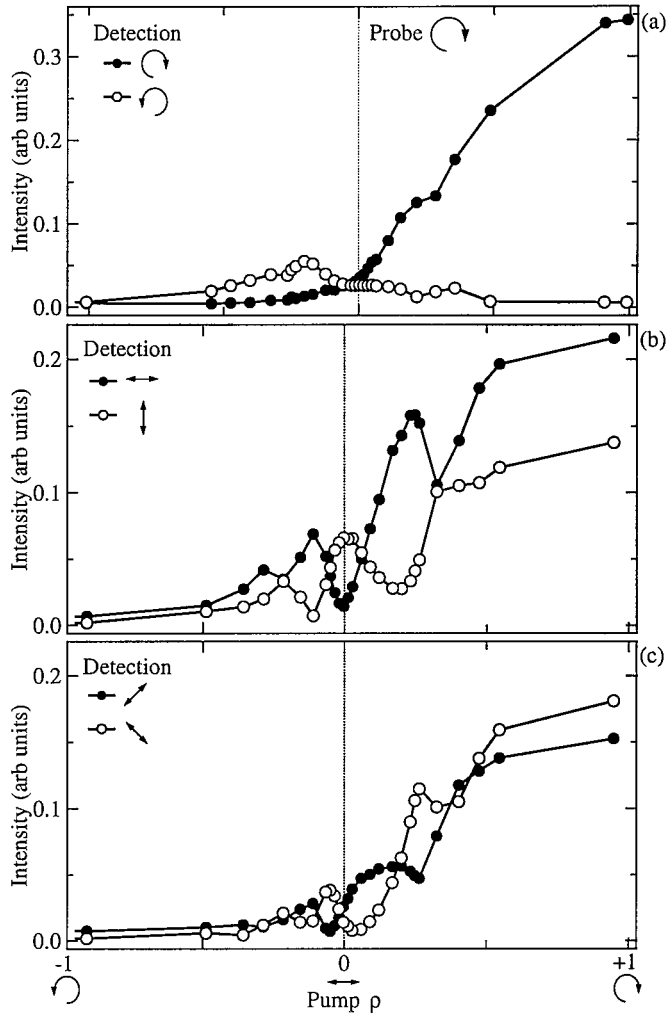

Figure 6.5: Intensity of idler emission, decomposed into (a) circular, (b) linear and (c) linear diagonal polarisations, as a function of the pump circular polarization degree. The probe is σ^+ polarized.

polaritons requires an elliptical pump, $\rho = 0.15$, Fig.6.4a. Light also emerges from non-seeded spin-down polaritons:- the intensity of this unexpected contribution can be even larger than that from the spin-up polaritons, and their emissions are matched when the pump injects equal spin populations. Examining the linear components of figures 6.4b,c shows that they rapidly oscillate in strength near $\rho \sim 0$, changing from near-vertical to near-horizontal with only a 5% change in net spin population. As seen in figure 6.3b, the emission is completely diagonally-polarized at $\rho = 0$. This graphically demonstrates the necessity of complete polarization analysis to resolve the true spin dynamics of the dynamical processes. The simple description of spin-preserving parametric scattering completely fails to predict this large enhancement.

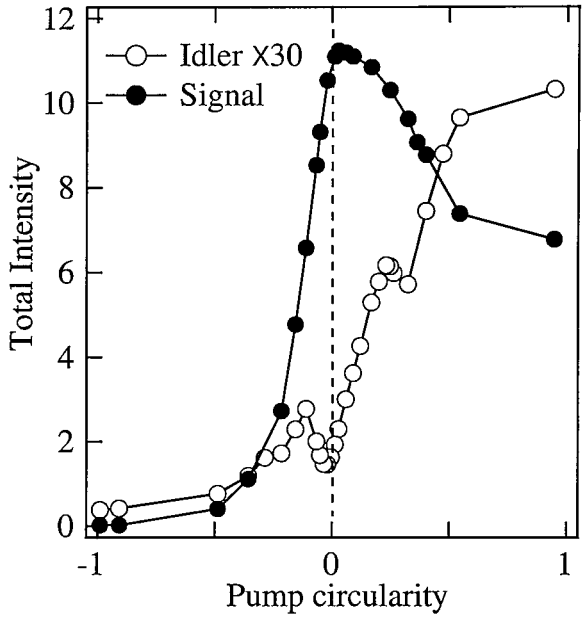

Figure 6.6: Total intensity of the emission of signal and idler as functions of the pump circular polarization degree.

The experimental values of the components that correspond to the three polarization degrees versus ρ for the emitted signal and idler are presented in figures 6.4(a,b,c) and 6.5(a,b,c) correspondingly. It can be seen that the linear components of both signal and idler exhibit oscillations versus circular polarization degree of pump. However, from a direct comparison of figures 6.4(a,b,c) and 6.5(a,b,c) it becomes evident that the total intensities of signal and idler emission versus ρ exhibit very different behaviour. To demonstrate clearly the difference a plot in figure 6.6 shows the total intensity of the emission versus pump circularity for both signal and idler. It is now evident that for the signal the total emitted light intensity is doubled for a linearly-polarized pump compared to a σ^+ polarized pump, while in the case of idler emission the total intensity monotonically drops as the pump circular polarization degree decreases. Note also that the coherence degree of signal and idler emission is different, as seen in figures 6.7(a,b). The coherence degree is defined as the length of the polarization vector on the Poincaré sphere. This parameter is always close to one for the signal while it is only about 0.5 for the idler at linear pumping. Enhancement of the idler coherence degree with polarization degree of the pump pulse is correlated with

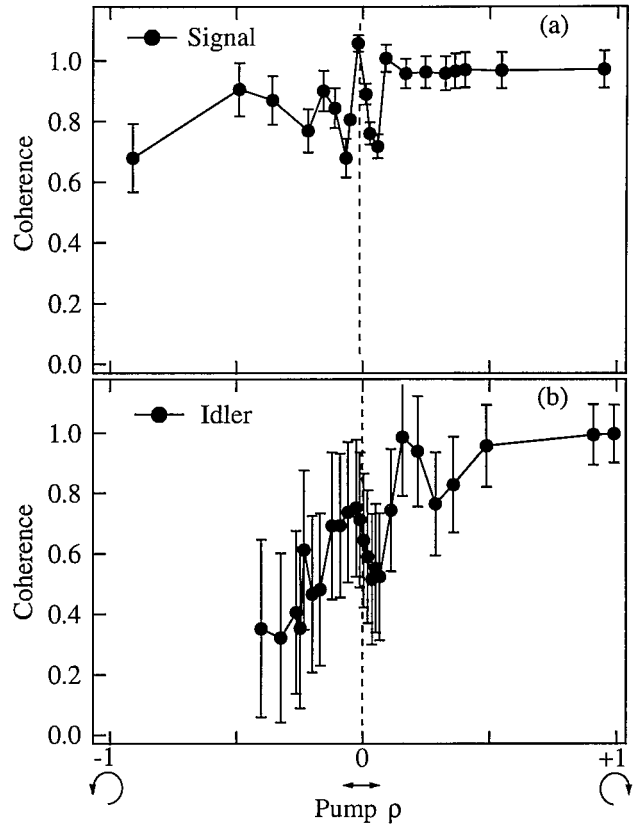

Figure 6.7: Coherence of signal and idler emission versus the pump circular polarization degree.

increasing overall intensity of idler emission, Fig.6.6. These observations can be intuitively understood having in mind that the idler polaritons have longer life-times and can be efficiently elastically scattered with much higher probability than $k = 0$ polaritons that have a substantial photonic component. This shows that spin-polarized excitons are more resistive and keep their polarization longer than linearly-polarized excitons. This should be true if spin-relaxation processes are slower than wavevector relaxation, which is usually the case in quantum wells.

Furthermore, two new features appear from the comparison of signal and idler that will prove in the following sections to be of high importance for the understanding of the spin dynamics in the parametric scattering of polaritons. Firstly, the signal emission is *diagonally* linearly polarized for *horizontal* linear pump polarization . This feature cannot be derived from a stimulation effect of the polariton scattering, as in this case only polaritons of one spin component (σ^+) are seeded. As it will be discussed

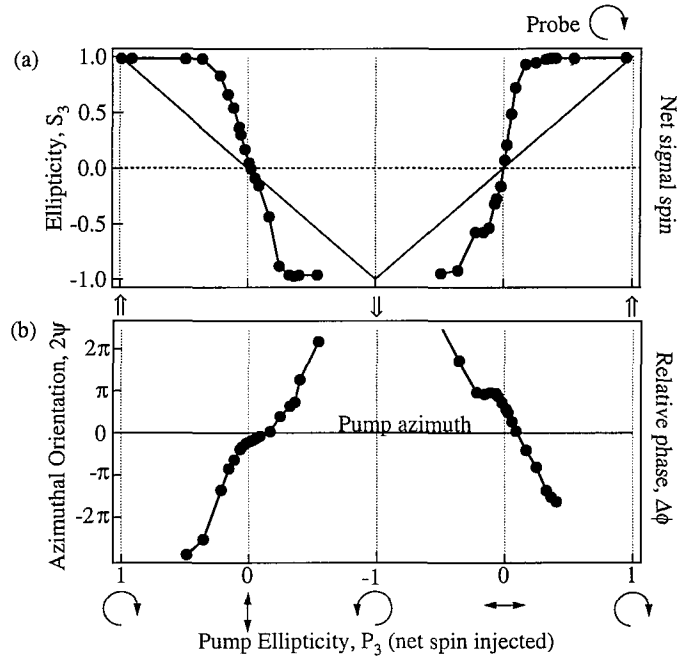

Figure 6.8: Signal emission as a function of pump ellipticity, decomposed into (a) ellipticity, and (b) azimuthal orientation of polarization ellipse.

in detail in section 6.3 this effect originates from the pump-induced splitting of the exciton resonance in directions *both parallel and orthogonal* to the linear polarization, which rotates the polarization of signal polaritons.

Secondly, for the same (horizontally-linear) pump polarization, the idler emission turns out to be *vertically* linear polarized. This feature is in fact in agreement with a calculation by Ciuti *et al.*[108], which showed that the matrix element of exciton-exciton interactions is dominated by the term coming from carrier-carrier exchange and it will be interpreted in the next theoretical sections together with the extremely pronounced and clear beats between the two linearly polarized components of emission both in signal and idler versus the circular polarization degree of the pump pulse.

To summarize the polarization behaviour in the pulsed regime, a plot of the net spin of the signal polaritons, is evidenced by the circular polarization degree of their emission, S_3, Fig.6.8a. The steep gradient of figure 6.8a demonstrates the delicate spin balance controlled by the pump - a small net spin in the pump polaritons creates a much larger net spin in the signal polaritons. Due to the stimulation process, the phase of each parametrically-scattering polariton is set by the phase of those

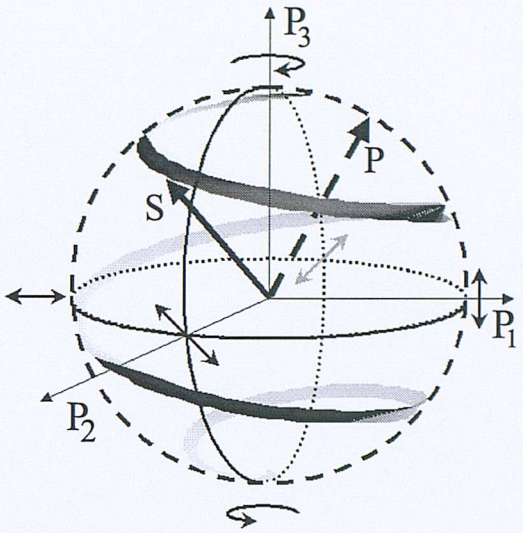

Figure 6.9: Poincaré sphere for representing polarizations: right/left circular at $P_3 = \pm 1$, and linear around the equator, $P_3 = 0$. In experiments, the pump follows the dashed meridian, while the signal emission follows the solid spiral.

polaritons already in the final state. Thus the two separate spin populations of signal polaritons can have a different macroscopic phase, $\phi_{\Uparrow,\Downarrow}$. As well as the *ratio of spin populations* in the signal, their *relative phase*, $\Delta\phi = \phi_{\Uparrow} - \phi_{\Downarrow}$ is recorded, which corresponds to the azimuthal orientation of the emitted polarization ellipse, $\psi = \tan^{-1}(S_2/S_1) = \Delta\phi/2$, Fig.6.8b. The axis of the signal polarization ellipse twists rapidly depending on the net spin injected into the system, $\Delta\phi \propto S_3$. On the Poincaré sphere, 2ψ is the longitude of the Stokes vector, which rotates through more than two full revolutions as the majority spin passes from up to down. This dramatic contrast with the fixed pump azimuthal orientation is seen in the spiralling trajectory of the signal Stokes vector, Fig.6.9.

6.3 Dynamical model of the Parametric Amplifier

Hitherto, the experimental data have been presented together with some conclusions derived from phenomenological arguments. In this section a theoretical approach to the observed dynamics is attempted. The model treats the exciton and photon interaction within the second quantization scheme and accounts for the exciton spin interaction with the intrinsic and applied fields in the microcavity structure. The

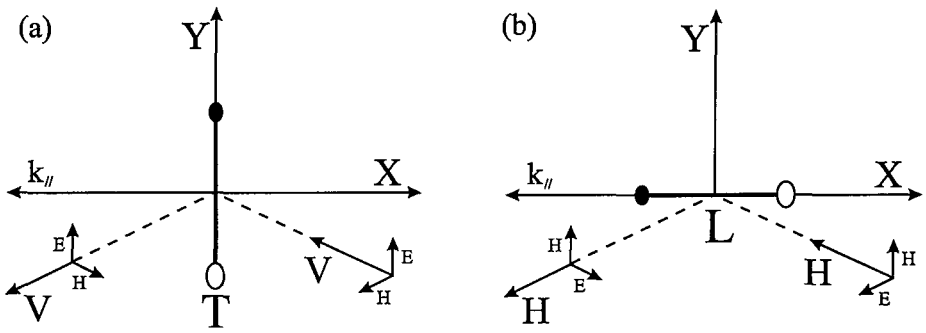

Figure 6.10: For in-plane wavevector parallel to the horizontal (a) T excitons are polarized along the Y-direction parallel to the V-linear polarized electromagnetic field (TE). (b) L excitons are polarized along the X-direction parallel to the H-linear polarized electromagnetic field (TM).

optical emission of quantum well excitons will be described within the dipole approximation and the exciton spin orientation and alignment will be linked to the different polarizations of the coupling light.

6.3.1 Exciton Spin and Alignment

The electromagnetic radiation from an excitonic dipole is maximized on the plane normal to the center of the dipole and is zero along the dipole axis.Therefore, in a quantum well optical emission perpendicular to the quantum well comes only from excitons with dipole moments parallel to the quantum well plane. Previous studies, have shown that only excitons polarized along the quantum well are optically active.[109] Excitons with dipole moment perpendicular to the quantum well plane are optically inactive due to the quantum confinement. This is an approximation in the case of heavy hole excitons in InGaAs/GaAs quantum wells as it is valid in the case of heavy-hole excitons in a cubic semiconductor.[109]

Excitons polarized parallel to the quantum well plane can further be distinguished into those which have dipole moments parallel to the in-plane wavevector $k_{//}$ (longitudinal excitons), and those which have dipole moments orthogonal to the in-plane wavevector $k_{//}$ (transverse excitons). Transverse (T) excitons couple only to TE modes and longitudinal (L) excitons couple only to TM modes.[110]

Therefore, optical emission from a quantum well can originate either from T excitons, or L excitons, or from a superposition of T and L excitons. Assuming in-plane wavevector parallel to the horizontal, as seen in figure 6.10, the correspondence between the various exciton polarizations and those of the electromagnetic field become apparent. Horizontally linearly polarized light (H) couples only to longitudinal excitons (polarized along X-direction), and vertically linear polarized light (V) couples only to transverse excitons (polarized along Y-direction). Diagonally linear polarized light (H', or V') couples to a linear superposition of L and T excitons since it can be analyzed as a linear superposition of H-, V-linear polarizations

$$|H'> = (1/\sqrt{2})|H> + (1/\sqrt{2})|V> \tag{6.3}$$

$$|V'> = (1/\sqrt{2})|H> - (1/\sqrt{2})|V> \tag{6.4}$$

Similarly, circularly polarized light couples to a coherent superposition of L and T excitons since it corresponds to a coherent superposition of H-, V-linear polarizations

$$|\sigma\pm> = (1/\sqrt{2})|H> \pm (i/\sqrt{2})|V> \tag{6.5}$$

and finally elliptically polarized light couples to a coherent superposition of L and T excitons of different weights since it corresponds to a coherent superposition of H-, V-linear polarizations with different weights

$$|\sigma\pm> = a|H> \pm b\, e^{i\Phi}|V> \tag{6.6}$$

where $a^2 + b^2 = 1$ and $a \neq b$.

Following the discussion of section 2.1.4, the different polarizations of light do not affect only the alignment of the excitonic dipole, X-,Y-directions, or superposition of those. Angular momentum conservation between the exciton and photon spins has to be satisfied (spin selection rules), Eq.2.15. Focusing on the spin selection rules of the heavy-hole exciton, seen in figure 2.5, an appropriate base to describe an exciton state according to its spin is that of the two opposite spin eigenstates. Therefore, right (left) circular, $\sigma+$ ($\sigma-$), polarized light couples to excitons of spin 1 (-1), $|1>$,($|-1>$)

and so on. The exciton spin is parallel to the direction of propagation of the polarized light.

The two basis ($|X>$,$|Y>$ or $|1>$,$|-1>$) for projecting an exciton state are equivalent. Thus, an L (T) exciton can be expressed as a coherent superposition of $|1>$ and $|-1>$ states

$$\begin{aligned} |X> &= (1/\sqrt{2})|1> + (1/\sqrt{2})|-1> \\ (|Y> &= (i/\sqrt{2})|1> - (i/\sqrt{2})|-1>) \end{aligned} \tag{6.7}$$

and reciprocally

$$|\pm 1> = (1/\sqrt{2})|X> \pm (i/\sqrt{2})|Y> \tag{6.8}$$

6.3.2 Spin Interactions in the Parametric Polariton Amplifier

It is straightforward to explain the scattering dynamics in the case of co- and cross-circular pump-probe polarization configuration in terms of spin conservation

$$|1>_{pump} + |1>_{pump} \xrightarrow[|1>_{probe}]{} |1>_{signal} + |1>_{idler} \tag{6.9}$$

and

$$|-1>_{pump} + |-1>_{pump} \xrightarrow[|1>_{probe}]{} \text{no parametric amplification} \tag{6.10}$$

as resulted from the experimental observations. Thus, exciton spin is a good quantum number for polaritons since it determines the onset or not of stimulation.

In the case of linear pump polarization and circular probe the only possible 'seeded' scattering channels are

$$|X>_{pump} + |X>_{pump} \xrightarrow[|1>_{probe}]{} 2|\pm 1>_{signal} + 2|\mp 1>_{idler} \tag{6.11}$$

which are based on the direct exciton scattering that breaks the coherence of the pump induced polaritons, $|X> = (1/\sqrt{2})|1> + (1/\sqrt{2})|-1>$. In an attempt to explain the observed dynamics based on the direct exciton interaction, the observed oscillation of the signal's linear polarized components could not be reproduced. Recent theoretical

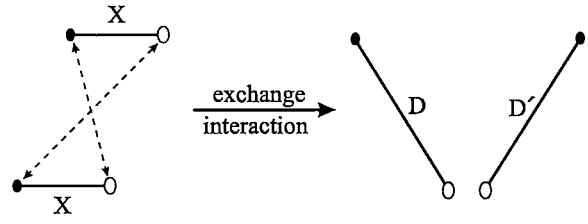

Figure 6.11: Exchange interaction of two X linear excitons. The outcome is two linear excitons D and D'.

investigations calculated that the direct exciton interaction is much weaker than the exchange interaction [108], suggesting that the observed dynamics are based on the exchange interaction.

Exchange interaction between two linear excitons (i.e. X-direction) can lead to the following configurations

$$|X> \ + \ |X> \ \rightarrow \ |D> \ + \ |D'> \tag{6.12}$$

where $|D> = \ a|X> \ + b|Y>$ and $|D'> = \ c|X> \ + d|Y>$ are linear superpositions of X and Y linear excitons with $a, b, c, d \ \epsilon \ \Re$ with $a = c$ and $b + d = 0$. The amplitude of these coefficients depends on the distance between the two initial X-linear excitons and therefore on the exciton density. A schematic of the exchange interaction is given in figure 6.11. However, in the case of the parametric amplifier the exchange process can not be stimulated from a circular probe

$$|X>_{pump} \ + \ |X>_{pump} \ \overset{\text{NO}\times\rightarrow}{|1>_{probe}} \ \ |D>_{signal} \ + \ |D'>_{idler} \tag{6.13}$$

since all possible final states are different from that induced by the probe beam $|1>_{probe}$. On the other hand, the presence of a probed linear final state, $|D>_{probe}$ could seed the stimulated scattering

$$|X>_{pump} \ + \ |X>_{pump} \ \overrightarrow{|D>_{probe}} \ |D>_{signal} \ + \ |D'>_{idler} \tag{6.14}$$

to that state.

Focusing on the particular experimental case of a linear pump, (i.e. $|X>$) and a circular probe (i.e. $|1>$), the observation of diagonal linear signal emission suggests that the process (6.14) is actually taking place with $|D> \equiv |X'>$. This would be possible if another mechanism would create probe polaritons of the $|X'>_{probe}$ state.

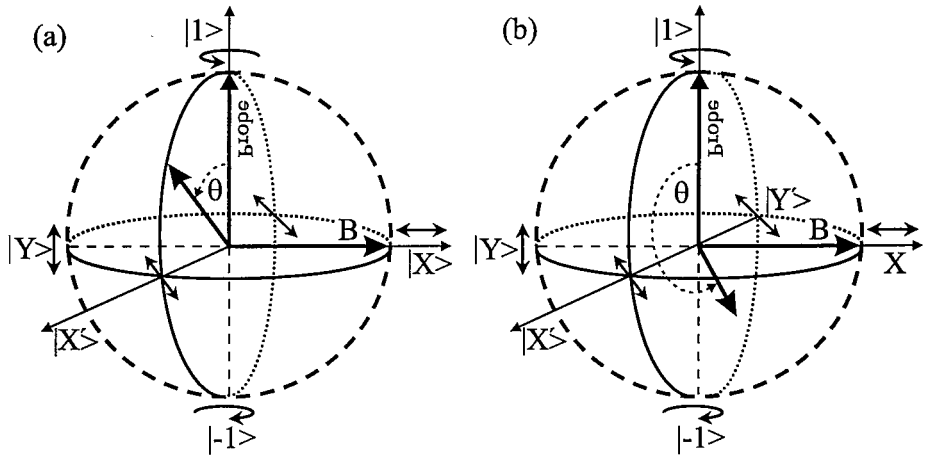

Figure 6.12: A circular exciton $|1>$, in the presence of an in-plane uniform magnetic field along the X-direction precesses on a plane orthogonal to the magnetic field direction.

6.3.3 Exciton Spin Precession

The exciton spin in the presence of a magnetic field undergoes Larmor precession. For example a circular exciton $|1>$, in the presence of an in-plane uniform magnetic field along the X-direction would precess on a plane orthogonal to the magnetic field direction, Fig.6.12a. This precession creates a probe projection along the X'-direction as long as the angle of precession $\theta\epsilon(0,\pi)$, and a projection along the Y' direction for $\theta\epsilon(\pi,2\pi)$, Fig.6.12b.

This precession leads to the desired signal polarization in the parametric polariton amplifier

$$|X>_{pump} + |X>_{pump} \xrightarrow[|X'>_{probe}]{} |X'>_{signal} + |Y'>_{idler} \tag{6.15}$$

as long as the period of precession is four times the pump pulse duration. The origin of the magnetic field cannot be intrinsic to the sample (strain matched) since the polarization of the signal emission changes from X' to Y'-linear polarization when pump is V-linearly polarized

$$|Y>_{pump} + |Y>_{pump} \xrightarrow[|Y'>_{probe}]{} |Y'>_{signal} + |X'>_{idler} \tag{6.16}$$

Therefore the origin of the magnetic field is related with the polarization of the pump beam.

In the polariton parametric amplifier, two different polariton states are resonantly excited (probe, pump) and three states are coherently populated from the scattering process (signal, pump, idler). Thus, three exciton states of different wavevectors are populated. Furthermore, the in-plane wavevector is a conserved quantity of the system as it is evidenced from the strict energy momentum conservation rules of the parametric scattering. Therefore, excitons can be conceptually separated for the different in-plane wavevectors. Excitons induced by the X-linear pump polarization are all aligned along the X-direction. This creates an energy splitting between the TE and TM modes in the quantum well plane due to Coulomb dipole-dipole interaction and long range exchange exciton-exciton interaction.[109, 32] This energy splitting, E_{XY}, creates an effective magnetic field along X-direction which exercises a torque on exciton spin states perpendicular to the magnetic field direction. The energy splitting dependence on pump-induced imbalance of X- and Y-linear excitons is assumed to be linear. This assumption holds for exciton densities smaller than the exciton saturation density, in the same way that the energy splitting between two opposite circular polarization is considered linear to their population imbalance. Thus

$$\hbar\omega_X = a_{XY}(N_X - N_Y) \tag{6.17}$$

where a_{XY} is the proportionality coefficient, N_X, N_Y are the X and Y exciton densities induced by the pump beam. a_{XY} is a constant, with its value set by the demand that the probe spin precession angle takes values in the range of $\theta\epsilon(0, pi/2]$, within the pump pulse duration. This splitting is estimated to be of the order of few $10^{th}s$ of μeV, which is smaller than the spectral resolution of the monochromator used in this study.

In a similar way, a circular polarized pump creates an energy splitting between the $|\pm 1>$ exciton spin states, $E_{\sigma+\sigma-}$.[111] However, the nature of this splitting is different from the one discussed above. In this case a $\sigma+$ polarized pump beam creates exciton states of parallel spin, $|1>$. The energy splitting in this case occurs from the magnetic dipole-dipole interaction and from phase space filling. This results in a much bigger energy splitting, $\hbar\omega_z \sim meV$. The energy splitting dependence on the spin imbalance between $|1>$ and $|-1>$ has been measured, Fig.6.13.[96]

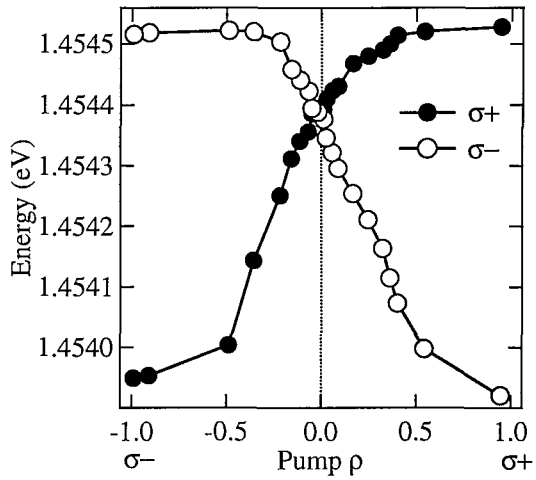

Figure 6.13: Energies of σ^+ and σ^- exciton resonance as functions of the pump circular polarization degree.

Finally, in the general case of an elliptical pump polarization, both kinds of energy splitting are present in the system, (E_{HV} and $E_{\sigma+\sigma-}$). Therefore, an exciton spin $|1>$ state, created by the probe beam will precess around the pump with a Larmor frequency

$$\omega_{tot} = \sqrt{\omega_X^2 + \omega_z^2} \tag{6.18}$$

Idler Emission

Exciton spin precession describes the experimentally observed diagonal X'-linear polarization of the emitted signal. From equation (6.12) it follows that idler emission should be orthogonal to signal's emission, therefore Y'-linear polarized. However, idler polaritons have a much higher probability of being elastically scattered than signal polaritons due to their high wavevector. Treating elastic scattering events as a perturbation on idler's dipole moment results in its alignment along the direction orthogonal to the pump induced exciton dipole moment as being lower energetically. Thus, idler's polarization is aligned along the Y-linear polarization for a X-linear polarized pump, in agreement with the experimental observation.

6.3.4 Pseudospin Space

In the discussion above, the exciton spin states have been projected on two different bases, a) the exciton spin, $|\pm 1>$, and b) the dipole's direction, X, Y. Besides the equivalence, the one or the other basis has been used in order to present the discussed exciton states as an eigenstate of the system.

In the simplest case of a $\sigma+$ circular probe and H-linear pump polarization, shown in figure 6.12, the probe induced exciton spin is in the eigenstate $|1>$. Under the influence of the effective magnetic field created by the pump, $|1>$ will start precessing on the X', Y' plane, Fig.6.12. Therefore, the state of the probe spin will be described by

$$|\Psi>_{probe} = a(t)\,|1> \;\; + b(t)\,|-1> \tag{6.19}$$

or equivalently

$$|\Psi>_{probe} = c(t)\,|X'> \;\; + d(t)\,|Y'> \tag{6.20}$$

where the $a(t)$, $b(t)$, $c(t)$, $d(t)$ are complex coefficients. Calculating the dynamical evolution of the system in any of the two basis will give information about the real magnitude of $a(t)$ and $b(t)$ or $c(t)$ and $d(t)$, which are related with the level populations of the basis eigenstates. However, when coherent processes are involved knowledge of the real values of the dynamical variables is not adequate to describe the state.

For example, in the parametric polariton amplifier in order to characterize the polarization state of the emitted signal, measurement of the real magnitude of a and b ($I_{\circlearrowleft}$, $I_{\circlearrowright}$) was not not adequate. Measurement of the three Stokes parameters was necessary, which corresponds to measurement of the level populations into three different orthogonal basis ($|\pm 1>$, $|X/Y>$ and $|X'/Y'>$).

The procedure for characterizing the polarization state of the emitted signal cannot be adapted for the calculation of the dynamical evolution of the exciton spin state, i.e. to calculate the dynamical evolution independently in each of the three orthogonal basis ($|\pm 1>$, $|X/Y>$ and $|X'/Y'>$) and then construct the complete polarization state. The reason is that in the parametric polariton amplifier, scattering processes between exciton eigenstates from different basis occur.[Section 6.3.2]

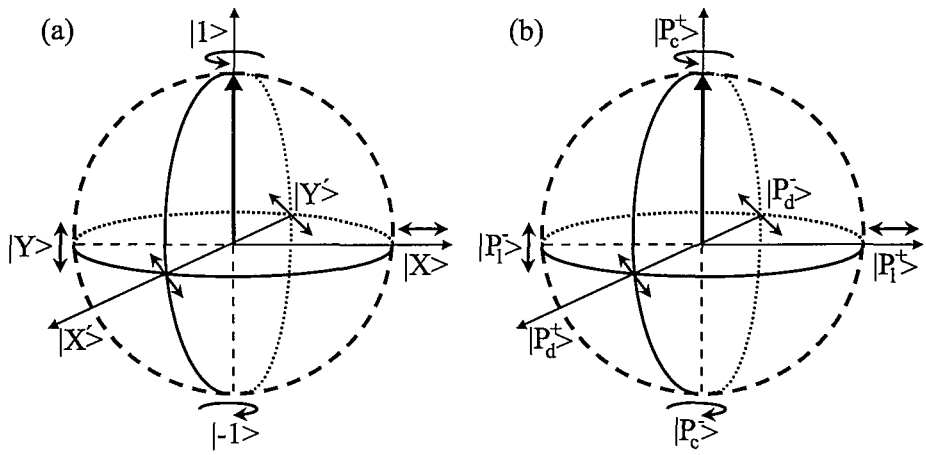

Figure 6.14: The correspondence between (a) exciton spin states and (b) pseudospin states.

Treatment of these processes in a single basis could be taken into account only by disentangling all other states which results in loss of coherence information.

A way to go around this problem is to construct three real functions (P_l, P_d, P_c) for example of a and b in the case of $|\pm 1>$ basis , that define a 3D-vector P, whose time dependence is given by

$$\begin{aligned} P_l &\equiv ab^* + ba* \\ P_d &\equiv i\,(ab^* - ba*) \\ P_c &\equiv aa^* - bb* \end{aligned} \tag{6.21}$$

The remaining real combination is $aa^* + bb^*$ which corresponds to the total spin population and is equal to the vector length $P = (P_l^2 + P_d^2 + P_c^2)^{1/2}$. In the case of dipole transitions with $\Delta m = \pm 1$, the mathematical space converts into a '*pseudo*' spin 1/2 space (pseudospin space).[112] Each function corresponds to a pseudospin 1/2, with $m_s = \pm 1/2$, which has the same characteristics of a real spin, i.e. pseudospins undergo Larmor precession in the presence of an effective magnetic field. Calculating the dynamical evolution of the three pseudospin components is equivalent with measuring the three Stokes parameters and therefore complete characterization of the spin dynamics can be obtained.[113] Its pseudospin is thus equivalent to an exciton spin state. The correspondence between exciton spin states and pseudospins is depicted on figure 6.14.

The time evolution of the precession of a pseudospin vector P around Ω =

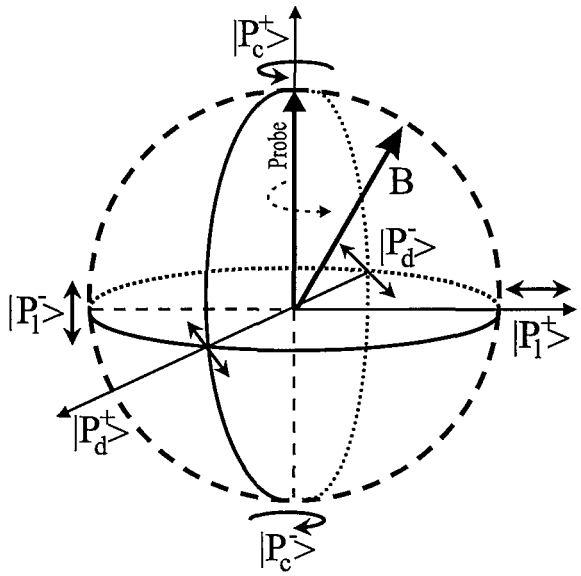

Figure 6.15: The precession of an exciton state with pseudospin $P_c = 1/2$ around an effective magnetic field that varies along the meridian of the pseudospin sphere.

$(\omega_X, \omega_Y, \omega_z)$ is given by

$$\frac{dP}{dt} = -\Omega \times P \tag{6.22}$$

where $\times$ represents the vector product.

The precession of an exciton state with an initial pseudospin state $|P_c^+>$ around an effective magnetic field that varies along the meridian of the pseudospin sphere, gives rise to oscillatory behaviour of the three polarization degrees, as seen in figure 6.16. In figures 6.16(a,b,c) the angle of pseudospin precession at the presence of an effective magnetic field parallel to $|P_l^+>$ is $\theta = \pi$. In figures 6.16(d,e,f) the angle of pseudospin precession at the presence of an effective magnetic field parallel to $|P_l^+>$ is $\theta = \pi/2$. $\omega_Y = 0$ and the ratio $\frac{\omega_z}{\omega_X}$ is kept $\frac{10}{1}$ in both cases. A complete model that accounts both for the pseudospin precession and the stimulated polariton scattering is developed in the following sections.

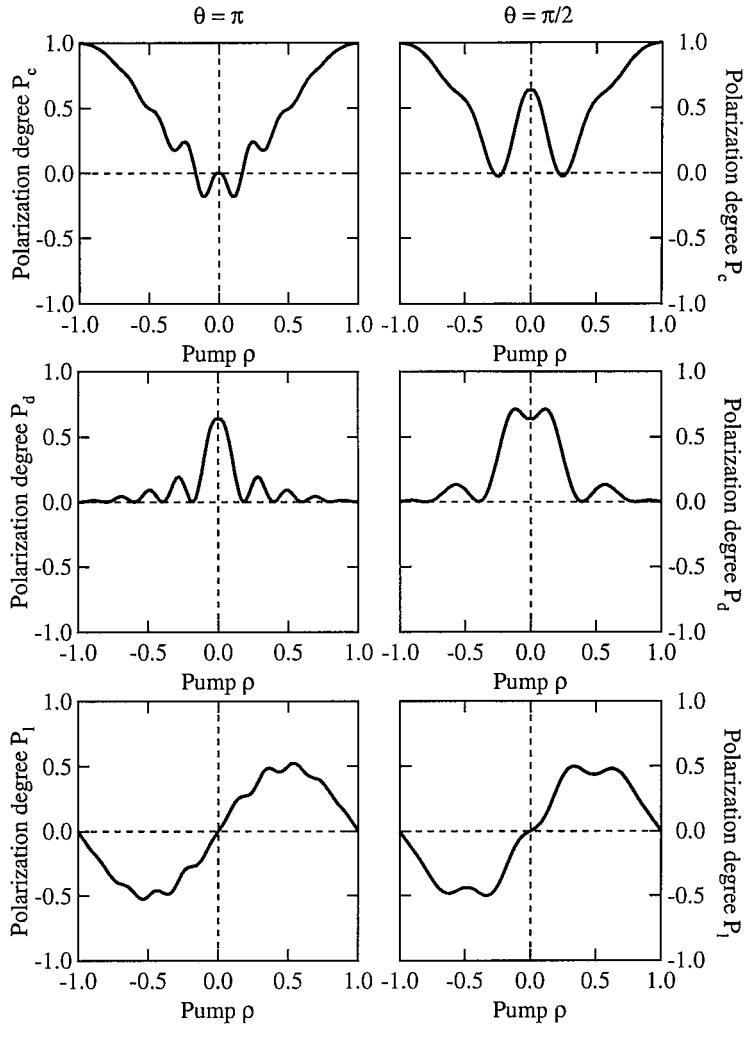

Figure 6.16: Pseudospin components P_c, P_l, P_d as a function of a rotating magnetic field along the meridian for an initial pseudospin state $|P_c^+>$.

6.4 Spinless Theory of Polariton Parametric Amplifier

In this section, the quantum mechanical model of the parametric amplifier is reviewed in its spinless form as developed by C. Ciuti.[114] In the parametric polariton amplifier two polariton states are resonantly excited and three are populated in total. Therefore, as a first approximation the model neglects the off-resonant contribution of the upper polariton branch and deals only with the interaction between the three coherent polariton states.

Interactions between polaritons originate from their exciton fraction.[Chapter 4] In the second quantization form the exciton-exciton interaction Hamiltonian is

$$H_{XX} = \frac{1}{2}\sum_{\mathrm{k,k',q}} V_{\mathrm{q}}^{XX} b^{\dagger}_{+,\mathrm{k+q}} b^{\dagger}_{+,\mathrm{k'-q}} b_{+,\mathrm{k}} b_{+,\mathrm{k'}} \tag{6.23}$$

where V_{q}^{XX} is the effective potential which is microscopically determined from the Coulomb electron-hole Hamiltonian.[108, 115] This potential becomes negligible for wavevectors comparable to α_{ex}^{-1}, where α_{ex} is the two dimensional exciton Bohr radius. On the other hand for small wavevectors it has a weak dependence on q, $V_{\mathrm{q}}^{XX} \simeq V_0^{XX}$. This approximation turns out to be very useful since the resonantly excited states in the parametric amplifier have small wavevectors. The zero wavevector value of the effective potential is

$$V_0^{XX} = \frac{6e^2\alpha_{ex}}{A\epsilon} \tag{6.24}$$

where ϵ is the static dielectric constant of the quantum well and A is the macroscopic quantization area. Furthermore, in this section the index + will be omitted from the creation and annihilation Bose operators since the model accounts only for excitons of the same spin state, i.e. $|1>$.

The Hamiltonian (6.23) does not account for exciton density dependent effects.[Chapter 4] Excitons are composite fermions, and their fermionic nature is revealed when the inter-exciton distance becomes comparable to α_{ex}. Exciton density effects give rise to a saturation of the exciton-photon coupling. The interaction is described by

$$H_{sat} = \frac{1}{2}\sum_{\mathrm{k,k',q}} \frac{\hbar\Omega_R}{n_{sat}A} a^{\dagger}_{\mathrm{k+q}} b^{\dagger}_{\mathrm{k'-q}} b_{\mathrm{k}} b_{\mathrm{k'}} + h.c. \tag{6.25}$$

where $n_{sat} = 7/(16\pi\alpha_{ex})$ is the exciton saturation density.[115]

Applying the inverse Hopfield transformation of (2.47) in (6.23) results in the reduced polariton-polariton interaction for the lower polariton branch

$$H_{PP} = \frac{1}{2}\sum_{\mathrm{k,k',q}} \frac{\alpha_{ex}^2}{A} V_0^{PP} p^{\dagger}_{\mathrm{k+q}} p^{\dagger}_{\mathrm{k'-q}} p_{\mathrm{k}} p_{\mathrm{k'}} \tag{6.26}$$

where the effective potential V_0^{PP} is due to the exciton-exciton interaction and the exciton-photon coupling saturation

$$V_0^{PP} = \frac{6e^2}{\epsilon\alpha_{ex}} X_{\mathrm{k+q}} X_{\mathrm{k'-q}} X_{\mathrm{k}} X_{\mathrm{k'}} + 2\frac{\hbar\Omega_R}{n_{sat}\alpha_{ex}^2}\left(|C_{\mathrm{k+q}}|X_{\mathrm{k'}} + X_{\mathrm{k+q}}|C_{\mathrm{k'}}|\right) X_{\mathrm{k'-q}} X_{\mathrm{k}} \tag{6.27}$$

where both terms have a positive contribution. Thus, the interaction between two polaritons (with the same spin) is always repulsive.

So far polariton interactions within the cavity have been considered. However, in order to describe polariton photoluminescence dynamics, coupling with the extracavity space needs to be taken into account. The finite transmission of the microcavity mirrors makes a microcavity an open system that interacts with the extracavity electromagnetic field. This interaction has been successfully treated within the quasi-mode approximation.[116, 117] The corresponding Hamiltonian for the lower polariton branch is

$$H_{ext} = g \sum_{\mathrm{k}} \Omega_{\mathrm{k}}(t) C_{\mathrm{k}} p_{\mathrm{k}}^{\dagger} + h.c \tag{6.28}$$

where $\Omega_{\mathrm{k}}(t)$ is the external electromagnetic field and g is the quasi-mode coupling constant that depends on mirror's reflectivity. In the case of polariton parametric amplifier

$$\Omega_{\mathrm{k}}(t) = \delta_{\mathrm{k},\mathrm{k_p}} \Omega_{pump}(t) + \delta_{\mathrm{k},0} \Omega_{probe}(t) \tag{6.29}$$

The pump (probe) field drives a strong (weak) polarization of the lower polariton mode with in-plane wavevector $\mathrm{k_p}$ (0), whose time dependence is represented by the expectation value $< p_{\mathrm{k_p}} > (t)$ ($< p_0 > (t)$). One important physical quantity linked with the external field is the polariton occupation number $N_{\mathrm{k}} = < p_{\mathrm{k}}^{\dagger} p_{\mathrm{k}} > \simeq | < p_{\mathrm{k}} > |^2$. This expression is an approximation of the coherent polariton population due to the field driven polarization, which suits the resonant excitation experimental conditions since the amplification process lasts as long as the pump pulse, Fig. 6.3.

Adding all the interactions together, the total Hamiltonian of this model becomes

$$H_{tot} = H_P + H_{PP} + H_{ext} \tag{6.30}$$

where H_P is the free polariton Hamiltonian (2.48) only for the lower polariton branch

$$H_P = \sum_{\mathrm{k}} E_{LP}(\mathrm{k}) p_{\mathrm{k}}^{\dagger} p_{\mathrm{k}} \tag{6.31}$$

Due to the polariton-polariton interaction in (6.30) the two polarization states, $< p_0 >$ and $< p_{\mathrm{k_p}} >$ are coupled. The basic scattering channel is

$$< p_{\mathrm{k_p}} > + < p_{\mathrm{k_p}} > \quad \overleftrightarrow{< p_0 >} \quad < p_0 > + < p_{2\mathrm{k_p}} > \tag{6.32}$$

which is the 'parametric' conversion of two pump polaritons into a signal-idler pair. Such matter wave-mixing amplifies coherently the probed polariton mode and creates a coherent population at the idler mode, for momentum conservation. The equations of motion for the three modes are closed when all other scattering channels are neglected.[118] These coupled equations of motion are obtained from Heisenberg equation and Wick factorization of the many-polariton expectation values in terms of $<p_0>$, $<p_{\mathrm{k_p}}>$, $<p_{2\mathrm{k_p}}>$ (e.g. $<p_0^\dagger p_{\mathrm{k_p}} p_{\mathrm{k_p}}>=<p_0>^*<p_{\mathrm{k_p}}>^2$).[119] The resulting equations are [114]

$$i\hbar\frac{\partial P_0}{\partial t} = \left(\widetilde{E}_{LP}(0) - i\gamma_0\right) P_0 + E_{int} P^*_{2\mathrm{k_p}} P^2_{\mathrm{k_p}} + F_{probe}(t) \tag{6.33}$$

$$i\hbar\frac{\partial P_{\mathrm{k_p}}}{\partial t} = \left(\widetilde{E}_{LP}(\mathrm{k_p}) - i\gamma_{\mathrm{k_p}}\right) P_{\mathrm{k_p}} + 2E_{int} P^*_{\mathrm{k_p}} P_0 P_{2\mathrm{k_p}} + F_{pump}(t) \tag{6.34}$$

$$i\hbar\frac{\partial P_{2\mathrm{k_p}}}{\partial t} = \left(\widetilde{E}_{LP}(2\mathrm{k_p}) - i\gamma_{2\mathrm{k_p}}\right) P_{2\mathrm{k_p}} + E_{int} P_0^* P^2_{\mathrm{k_p}} \tag{6.35}$$

where for convenience the rescaled polarization $P_{\mathrm{k}}(t)$ has been employed

$$P_{\mathrm{k}}(t) = \frac{\alpha_{ex}}{\sqrt{A}} <p_{\mathrm{k}}> (t) \tag{6.36}$$

whose amplitude is

$$|P_{\mathrm{k}}|^2 = n_{\mathrm{k}} \alpha_{ex}^2 \tag{6.37}$$

where n_{k} is the coherent density of k-polaritons in units of α_{ex}^{-2}. The inhomogeneous terms are the rescaled pump (probe) driving fields

$$\begin{array}{l} F_{pump}(t) = \frac{\alpha_{ex}}{\sqrt{A}} g C_{\mathrm{k_p}} \Omega_{pump}(t) \\ \left(F_{probe}(t) = \frac{\alpha_{ex}}{\sqrt{A}} g C_0 \Omega_{probe}(t)\right) \end{array} \tag{6.38}$$

and the parametric coupling occurs through the interaction energy

$$E_{int} = \frac{1}{2}(V^{PP}_{\mathrm{k_p},\mathrm{k_p},\mathrm{k_p}} + V^{PP}_{\mathrm{k_p},\mathrm{k_p},-\mathrm{k_p}}) \tag{6.39}$$

The energies γ_0, $\gamma_{\mathrm{k_p}}$, $\gamma_{2\mathrm{k_p}}$ are the homogeneous linewidths of the corresponding polariton modes. Finally, the renormalized polariton energy $\widetilde{E}_{LP}(\mathrm{k}) \neq E_{LP}(\mathrm{k})$ is blueshifted with respect to the free polariton energy $E_{LP}(\mathrm{k})$ by

$$\widetilde{E}_{LP}(\mathrm{k}) - E_{LP}(\mathrm{k}) = (V^{PP}_{\mathrm{k},\mathrm{k_p},0} + V^{PP}_{\mathrm{k},\mathrm{k_p},\mathrm{k_p}-\mathrm{k}})|P_{\mathrm{k}}|^2 \simeq 2V^{PP}_{\mathrm{k},\mathrm{k_p},0}|P_{\mathrm{k}}|^2 \tag{6.40}$$

The generalized equation of motion,[118] when more than three polariton modes are involved into the parametric polariton scattering is

$$i\hbar\frac{\partial P_{\mathrm{k}}}{\partial t} = \left(\widetilde{E}_{LP}(\mathrm{k}) - i\gamma_{\mathrm{k}}\right) P_{\mathrm{k}} + \sum_{\mathrm{k}',\mathrm{k}''\neq\mathrm{k}} E^{int}_{\mathrm{k},\mathrm{k}',\mathrm{k}''} P^{*}_{\mathrm{k}'+\mathrm{k}''-\mathrm{k}} P_{\mathrm{k}'} P_{\mathrm{k}''} + F_{\mathrm{k}}(t) \tag{6.41}$$

where the generalized coupling energy is

$$E^{int}_{\mathrm{k},\mathrm{k}',\mathrm{k}''} = \frac{1}{2}(V^{PP}_{\mathrm{k}',\mathrm{k}'',\mathrm{k}-\mathrm{k}'} + V^{PP}_{\mathrm{k}',\mathrm{k}'',\mathrm{k}''-\mathrm{k}}) \tag{6.42}$$

and the general expression for the renormalized polariton energy is

$$\widetilde{E}_{LP}(\mathrm{k}) = E_{LP}(\mathrm{k}) + \sum_{\mathrm{k}'} E^{shift}_{\mathrm{k},\mathrm{k}'} |P_{\mathrm{k}'}|^2 \tag{6.43}$$

where $E^{shift}_{\mathrm{k},\mathrm{k}'} = V^{PP}_{\mathrm{k},\mathrm{k}',0} + V^{PP}_{\mathrm{k},\mathrm{k}',\mathrm{k}'-\mathrm{k}}$. Finally the applied external fields produce the driving term $F_{\mathrm{k}}(t) = \frac{\alpha_{ex}}{\sqrt{A}} g C_{\mathrm{k}} \Omega_{\mathrm{k}}(t)$.[119]

In order for this model to account for the spin dynamics of the parametric amplifier discussed in the previous sections, spin degrees of freedom should be attributed to the different polariton modes.

6.5 Polariton Parametric Amplifier

Following the discussion in section 6.3.2, the spin conservation of the parametric scattering, ((6.9), (6.10)), imposes exciton spin as a good quantum number. Including the exciton spin degree of freedom into the coupled equation of motion of the parametric polariton amplifier, (6.33), (6.34), (6.35), one gets

$$i\hbar\frac{\partial P_{+,0}}{\partial t} = \left(\widetilde{E}_{LP}(+,0) - i\gamma_0\right) P_{+,0} + E_{int} P^{*}_{+,2\mathrm{k_p}} P^{2}_{+,\mathrm{k_p}} + F_{+,probe}(t)$$

$$i\hbar\frac{\partial P_{-,0}}{\partial t} = \left(\widetilde{E}_{LP}(-,0) - i\gamma_0\right) P_{-,0} + E_{int} P^{*}_{-,2\mathrm{k_p}} P^{2}_{-,\mathrm{k_p}} \tag{6.44}$$

$$i\hbar\frac{\partial P_{+,\mathrm{k_p}}}{\partial t} = \left(\widetilde{E}_{LP}(+,\mathrm{k_p}) - i\gamma_{\mathrm{k_p}}\right) P_{+,\mathrm{k_p}} + 2E_{int} P^{*}_{+,\mathrm{k_p}} P_{+,0} P_{+,2\mathrm{k_p}} + F_{+,pump}(t)$$

$$i\hbar\frac{\partial P_{-,\mathrm{k_p}}}{\partial t} = \left(\widetilde{E}_{LP}(-,\mathrm{k_p}) - i\gamma_{\mathrm{k_p}}\right) P_{-,\mathrm{k_p}} + 2E_{int} P^{*}_{-,\mathrm{k_p}} P_{-,0} P_{-,2\mathrm{k_p}} + F_{-,pump}(t) \tag{6.45}$$

$$i\hbar\frac{\partial P_{+,2k_p}}{\partial t} = \left(\widetilde{E}_{LP}(+,2k_p) - i\gamma_{2k_p}\right) P_{+,2k_p} + E_{int}P^*_{+,0}P^2_{+,k_p}$$

$$i\hbar\frac{\partial P_{-,2k_p}}{\partial t} = \left(\widetilde{E}_{LP}(-,2k_p) - i\gamma_{2k_p}\right) P_{-,2k_p} + E_{int}P^*_{-,0}P^2_{-,k_p} \tag{6.46}$$

where $+$, $-$ originate from the $\sigma+$ and $\sigma-$ circular polarized light that is used to excite the polariton spin states $|1>$ and $|-1>$ correspondingly. For simplicity the different polariton modes linewidths have been kept equal for both spin states and in the case of probe the $\sigma-$ circular external field has been omitted since in the experimental configuration probe is always kept $\sigma+$ circular polarized.

It is apparent that in the case of co- or cross-circular polarized light, equations (6.44), (6.45) and (6.46) can describe correctly the dynamics of the parametric polariton amplifier including the spin. However, when scattering events that include coherent superpositions of $|1>$ and $|-1>$ exciton spins are taken into account these equations fail to describe the dynamics of the system as discussed in section 6.3.4.

6.6 Pseudospin Dynamical Evolution

It was shown in sections 6.3.4 and 6.3.2 that the correct basis to describe the different scattering channels is that of the pseudospin space. An equation of motion is derived for each pseudospin state. The allowed scattering channels of the different exciton spin states produce a coupling term between the corresponding pseudospin states. The possible scattering channels are presented together with their pseudospin analog.

By analogy with the equations of motion for the signal, pump, and idler, for the exciton spin states $|1>$ and $|-1>$, (6.44), (6.45), (6.46), the equations of motion for the pseudospin states P_c^+, P_c^-, P_l^+, P_l^-, P_d^+, P_d^-, for the signal are

$$i\hbar\frac{\partial P_{P_c^+,0}}{\partial t} = \left(\widetilde{E}_{LP}(P_c^+,0) - i\gamma_0\right) P_{P_c^+,0} + E_{int}P^*_{P_c^+,2k_p}P^2_{P_c^+,k_p} + F_{P_c^+,probe}(t)$$

$$i\hbar\frac{\partial P_{P_c^-,0}}{\partial t} = \left(\widetilde{E}_{LP}(P_c^-,0) - i\gamma_0\right) P_{P_c^-,0} + E_{int}P^*_{P_c^-,2k_p}P^2_{P_c^-,k_p} \tag{6.47}$$

$$i\hbar\frac{\partial P_{\mathrm{P_l^+},0}}{\partial t} = \left(\widetilde{E}_{LP}(\mathrm{P_l^+},0) - i\gamma_0\right) P_{\mathrm{P_l^+},0} + E_{int} P^*_{\mathrm{P_l^+},2\mathrm{k_p}} P^2_{\mathrm{P_l^+},\mathrm{k_p}}$$

$$i\hbar\frac{\partial P_{\mathrm{P_l^-},0}}{\partial t} = \left(\widetilde{E}_{LP}(\mathrm{P_l^-},0) - i\gamma_0\right) P_{\mathrm{P_l^-},0} + E_{int} P^*_{\mathrm{P_l^-},2\mathrm{k_p}} P^2_{\mathrm{P_l^-},\mathrm{k_p}} \tag{6.48}$$

$$i\hbar\frac{\partial P_{\mathrm{P_d^+},0}}{\partial t} = \left(\widetilde{E}_{LP}(\mathrm{P_d^+},0) - i\gamma_0\right) P_{\mathrm{P_d^+},0} + E_{int} P^*_{\mathrm{P_d^+},2\mathrm{k_p}} P^2_{\mathrm{P_d^+},\mathrm{k_p}}$$

$$i\hbar\frac{\partial P_{\mathrm{P_d^-},0}}{\partial t} = \left(\widetilde{E}_{LP}(\mathrm{P_d^-},0) - i\gamma_0\right) P_{\mathrm{P_d^-},0} + E_{int} P^*_{\mathrm{P_d^-},2\mathrm{k_p}} P^2_{\mathrm{P_d^-},\mathrm{k_p}} \tag{6.49}$$

where +, − indicates pseudospin of 1/2, -1/2 correspondingly. An external field has been applied only to the $\mathrm{P_c^+}$ pseudospin state that corresponds to the $|1>$ exciton spin state, since in the experimental configuration probe is always kept $\sigma+$ circular polarized.

Similarly, the pseudospin states for the pumped polariton mode are

$$i\hbar\frac{\partial P_{\mathrm{P_c^+},\mathrm{k_p}}}{\partial t} = \left(\widetilde{E}_{LP}(\mathrm{P_c^+},\mathrm{k_p}) - i\gamma_{\mathrm{k_p}}\right) P_{\mathrm{P_c^+},\mathrm{k_p}} + 2E_{int} P^*_{\mathrm{P_c^+},\mathrm{k_p}} P_{\mathrm{P_c^+},0} P_{\mathrm{P_c^+},2\mathrm{k_p}} + F_{P_c^+,pump}(t)$$

$$i\hbar\frac{\partial P_{\mathrm{P_c^-},\mathrm{k_p}}}{\partial t} = \left(\widetilde{E}_{LP}(\mathrm{P_c^-},\mathrm{k_p}) - i\gamma_{\mathrm{k_p}}\right) P_{\mathrm{P_c^-},\mathrm{k_p}} + 2E_{int} P^*_{\mathrm{P_c^-},\mathrm{k_p}} P_{\mathrm{P_c^-},0} P_{\mathrm{P_c^-},2\mathrm{k_p}} + F_{P_c^-,pump}(t) \tag{6.50}$$

$$i\hbar\frac{\partial P_{\mathrm{P_l^+},\mathrm{k_p}}}{\partial t} = \left(\widetilde{E}_{LP}(\mathrm{P_l^+},\mathrm{k_p}) - i\gamma_{\mathrm{k_p}}\right) P_{\mathrm{P_l^+},\mathrm{k_p}} + 2E_{int} P^*_{\mathrm{P_l^+},\mathrm{k_p}} P_{\mathrm{P_l^+},0} P_{\mathrm{P_l^+},2\mathrm{k_p}} + F_{P_l^+,pump}(t)$$

$$i\hbar\frac{\partial P_{\mathrm{P_l^-},\mathrm{k_p}}}{\partial t} = \left(\widetilde{E}_{LP}(\mathrm{P_l^-},\mathrm{k_p}) - i\gamma_{\mathrm{k_p}}\right) P_{\mathrm{P_l^-},\mathrm{k_p}} + 2E_{int} P^*_{\mathrm{P_l^-},\mathrm{k_p}} P_{\mathrm{P_l^-},0} P_{\mathrm{P_l^-},2\mathrm{k_p}} + F_{P_l^-,pump}(t) \tag{6.51}$$

$$i\hbar\frac{\partial P_{\mathrm{P_d^+},\mathrm{k_p}}}{\partial t} = \left(\widetilde{E}_{LP}(\mathrm{P_d^+},\mathrm{k_p}) - i\gamma_{\mathrm{k_p}}\right) P_{\mathrm{P_d^+},\mathrm{k_p}} + 2E_{int} P^*_{\mathrm{P_d^+},\mathrm{k_p}} P_{\mathrm{P_d^+},0} P_{\mathrm{P_d^+},2\mathrm{k_p}} \tag{6.52}$$

$$i\hbar\frac{\partial P_{\mathrm{P_d^-},\mathrm{k_p}}}{\partial t} = \left(\widetilde{E}_{LP}(\mathrm{P_d^-},\mathrm{k_p}) - i\gamma_{\mathrm{k_p}}\right) P_{\mathrm{P_d^-},\mathrm{k_p}} + 2E_{int} P^*_{\mathrm{P_d^-},\mathrm{k_p}} P_{\mathrm{P_d^-},0} P_{\mathrm{P_d^-},2\mathrm{k_p}}$$

where external fields have been applied to P_c^+, P_c^-, P_l^+, P_l^- pseudospin states that correspond to the exciton spin states that span the the meridian of the Poincare sphere, Fig.6.15, as in the experimental case.

Finally, the pseudospin states for the idler polariton mode are

$$i\hbar\frac{\partial P_{P_c^+,2k_p}}{\partial t} = \left(\widetilde{E}_{LP}(P_c^+,2k_p) - i\gamma_{2k_p}\right) P_{P_c^+,2k_p} + E_{int}P^*_{P_c^+,0}P^2_{P_c^+,k_p}$$

$$i\hbar\frac{\partial P_{P_c^-,2k_p}}{\partial t} = \left(\widetilde{E}_{LP}(P_c^-,2k_p) - i\gamma_{2k_p}\right) P_{P_c^-,2k_p} + E_{int}P^*_{P_c^-,0}P^2_{P_c^-,k_p} \tag{6.53}$$

$$i\hbar\frac{\partial P_{P_l^+,2k_p}}{\partial t} = \left(\widetilde{E}_{LP}(P_l^+,2k_p) - i\gamma_{2k_p}\right) P_{P_l^+,2k_p} + E_{int}P^*_{P_l^+,0}P^2_{P_l^+,k_p}$$

$$i\hbar\frac{\partial P_{P_l^-,2k_p}}{\partial t} = \left(\widetilde{E}_{LP}(P_l^-,2k_p) - i\gamma_{2k_p}\right) P_{P_l^-,2k_p} + E_{int}P^*_{P_l^-,0}P^2_{P_l^-,k_p} \tag{6.54}$$

$$i\hbar\frac{\partial P_{P_d^+,2k_p}}{\partial t} = \left(\widetilde{E}_{LP}(P_d^+,2k_p) - i\gamma_{2k_p}\right) P_{P_d^+,2k_p} + E_{int}P^*_{P_d^+,0}P^2_{P_d^+,k_p}$$

$$i\hbar\frac{\partial P_{P_d^-,2k_p}}{\partial t} = \left(\widetilde{E}_{LP}(P_d^-,2k_p) - i\gamma_{2k_p}\right) P_{P_d^-,2k_p} + E_{int}P^*_{P_d^-,0}P^2_{P_d^-,k_p} \tag{6.55}$$

where no external fields have been applied.

So far, the equations of motion of the pseudospin states are coupled only between the same pseudospin state. However, in order to describe scattering channels like (6.14), coupling between different pseudospin states has to be included in the equation of motion. More specifically in the case of $|X>$ pumped exciton spin states and a projection of the probe on $|X'>$ or $|Y'>$ exciton spin state the following channels are allowed

$$|X>_{pump} + |X>_{pump} \xrightarrow[|X'>_{probe}]{} |X'>_{signal} + |Y'>_{idler} \tag{6.56}$$

$$|X>_{pump} + |X>_{pump} \xrightarrow[|Y'>_{probe}]{} |Y'>_{signal} + |X'>_{idler} \tag{6.57}$$

The equivalent scattering configuration for the pseudospin states are

$$|P_l^+>_{pump} + |P_l^+>_{pump} \xrightarrow[|P_d^+>_{probe}]{} |P_d^+>_{signal} + |P_d^->_{idler} \tag{6.58}$$

$$|P_l^+>_{pump} + |P_l^+>_{pump} \xrightarrow[|P_d^->_{probe}]{} |P_d^->_{signal} + |P_d^+>_{idler} \tag{6.59}$$

In the case of $|Y>$ pumped exciton spin states the corresponding scattering channels have exactly the same terms on the right hand side. In the case of a projection of the probe on $|X>$ or $|Y>$ exciton spin states terms on the left hand side remain the same and on the right hand side signal has the same state with the probe and idler has the orthogonal.

Equations (6.58) and (6.59) and their equivalent for the other combinations of exciton spin states give rise to coupling terms in the pseudospin equations of motion between the $P^+_{l/d}$ and $P^-_{l/d}$ states. These terms are

$$\begin{aligned} E^{cross}_{P^+_d,0} &= E_{P^+_d,P^+_l} P^*_{P^-_d,2k_p} P^2_{P^+_l,k_p} + E_{P^+_d,P^-_l} P^*_{P^-_d,2k_p} P^2_{P^-_l,k_p} \\ E^{cross}_{P^-_d,0} &= E_{P^-_d,P^+_l} P^*_{P^+_d,2k_p} P^2_{P^+_l,k_p} + E_{P^-_d,P^-_l} P^*_{P^+_d,2k_p} P^2_{P^-_l,k_p} \end{aligned} \tag{6.60}$$

$$\begin{aligned} E^{cross}_{P^+_l,k_p} &= E_{P^+_d,P^+_l} P^*_{P^+_l,k_p} [(P_{P^+_d,0} P_{P^-_d,2k_p}) + (P_{P^-_d,0} P_{P^+_d,2k_p})] \\ &+ E_{P^-_d,P^+_l} P^*_{P^+_l,k_p} [(P_{P^+_d,0} P_{P^-_d,2k_p}) + (P_{P^-_d,0} P_{P^+_d,2k_p})] \end{aligned} \tag{6.61}$$

$$\begin{aligned} E^{cross}_{P^-_l,k_p} &= E_{P^+_d,P^-_l} P^*_{P^-_l,k_p} [(P_{P^+_d,0} P_{P^-_d,2k_p}) + (P_{P^-_d,0} P_{P^+_d,2k_p})] \\ &+ E_{P^-_d,P^-_l} P^*_{P^-_l,k_p} [(P_{P^+_d,0} P_{P^-_d,2k_p}) + (P_{P^-_d,0} P_{P^+_d,2k_p})] \end{aligned}$$

$$\begin{aligned} E^{cross}_{P^+_d,2k_p} &= E_{P^+_d,P^+_l} P^*_{P^-_d,0} P^2_{P^+_l,k_p} + E_{P^+_d,P^-_l} P^*_{P^-_d,0} P^2_{P^-_l,k_p} \\ E^{cross}_{P^-_d,2k_p} &= E_{P^-_d,P^+_l} P^*_{P^+_d,0} P^2_{P^+_l,k_p} + E_{P^-_d,P^-_l} P^*_{P^+_d,0} P^2_{P^-_l,k_p} \end{aligned} \tag{6.62}$$

where $E_{P^+_d,P^+_l}$, $E_{P^+_d,P^-_l}$, $E_{P^-_d,P^-_l}$, and $E_{P^-_d,P^+_l}$ are the interaction energies of the cross-pseudospin coupling terms, where the equality of terms from interchange of the $+$, $-$ signs has been taken into account.

The precession of the pseudospins in the presence of a magnetic field is given by (6.22) where the pseudospin components are P_l, P_d, and P_c and $\Omega = (\omega_X, 0, \omega_z)$ since

the pump polarization has been varied on the XY plane. Hence their time evolution is described by

$$\begin{aligned}\frac{dP_l}{dt} &= \omega_z P_d \\ \frac{dP_d}{dt} &= \omega_X P_c - \omega_z P_l \\ \frac{dP_c}{dt} &= \omega_X P_d\end{aligned} \tag{6.63}$$

or for the separated pseudospin states

$$\begin{aligned}\frac{dP_l^+}{dt} &= \omega_z(P_d^+ - P_d^-)\Theta(P_l^+) \\ \frac{dP_l^-}{dt} &= -\omega_z(P_d^+ - P_d^-)\Theta(P_l^-)\end{aligned}$$

$$\begin{aligned}\frac{dP_d^+}{dt} &= \left[\omega_X(P_c^+ - P_c^-) - \omega_z(P_l^+ - P_l^-)\right]\Theta(P_d^+) \\ \frac{dP_d^-}{dt} &= -\left[\omega_X(P_c^+ - P_c^-) - \omega_z(P_l^+ - P_l^-)\right]\Theta(P_d^-)\end{aligned} \tag{6.64}$$

$$\begin{aligned}\frac{dP_c^+}{dt} &= \omega_X(P_d^+ - P_d^-)\Theta(P_c^+) \\ \frac{dP_c^-}{dt} &= -\omega_X(P_d^+ - P_d^-)\Theta(P_c^-)\end{aligned}$$

where Θ is the Heavyside step function. Adding this components to the pseudospin equations of motion for the parametric polariton amplifier ((6.47)-(6.52), including the cross-coupling terms (6.60)-(6.62)) the dynamical evolution of the parametric amplifier including the polariton spin, is formulated.

The numerical simulation of these coupled differential equations has as parameters the interaction strength between the different pseudospin states, which correspond to different matrix elements of the pseudospin-pseudospin interaction matrix

$$\begin{pmatrix} E_{P_l^+,P_l^+} & E_{P_l^+,P_l^-} & E_{P_l^+,P_d^+} & E_{P_l^+,P_d^-} \\ E_{P_l^-,P_l^+} & E_{P_l^-,P_l^-} & E_{P_l^-,P_d^+} & E_{P_l^-,P_d^-} \\ E_{P_d^+,P_l^+} & E_{P_d^+,P_l^-} & E_{P_d^+,P_d^+} & E_{P_d^+,P_d^-} \\ E_{P_d^-,P_l^+} & E_{P_d^-,P_l^-} & E_{P_d^-,P_d^+} & E_{P_d^-,P_d^-} \end{pmatrix} \tag{6.65}$$

and

$$\begin{pmatrix} E_{P_c^+,P_c^+} & E_{P_c^+,P_c^-} \\ E_{P_c^-,P_c^+} & E_{P_c^-,P_c^-} \end{pmatrix} \tag{6.66}$$

Symmetry reasons reduce the arbitrary matrix elements to five (5). Due to the equivalence between the different pseudospin states and the real exciton spin states, knowledge of matrices (6.65), (6.66) corresponds to knowledge of the exciton-exciton interaction matrix elements for the different exciton spin states

$$\begin{pmatrix} E_{XX} & E_{XY} & E_{XX'} & E_{XY'} \\ E_{YX} & E_{YY} & E_{YX'} & E_{YY'} \\ E_{X'X} & E_{X'Y} & E_{X'X'} & E_{X'Y'} \\ E_{Y'X} & E_{Y'Y} & E_{Y'X'} & E_{Y'Y'} \end{pmatrix} \tag{6.67}$$

and

$$\begin{pmatrix} E_{\sigma+\sigma+} & E_{\sigma+\sigma-} \\ E_{\sigma-\sigma+} & E_{\sigma-\sigma-} \end{pmatrix} \tag{6.68}$$

The five arbitrary parameters in the real exciton spin space correspond to the different interaction strengths between: i) co-circular exciton spin states, ii) cross-circular exciton spin states, iii) excitons of parallel exciton dipole moments, iv) excitons of orthogonal dipole moments and v) excitons of intersecting at 45° dipole moments.

6.7 Conclusions

In this chapter, the spin dynamics of the polariton parametric amplifier were thoroughly investigated. Complete characterization of the polarized emission from signal and idler led to the disentanglement of the different mechanisms that produce the observed spin mixing. The presented theoretical model produced a phenomenological interpretation of the observed dynamics and formulated the equations of motion that describe the system, starting from the spinless quantum mechanical treatment of the parametric polariton amplifier.

Chapter 7

Quantum Dot lasing in Semiconductor Microcavities

In this chapter, the coexistence of low threshold lasing and strong coupling in a high-quality semiconductor microcavity under near-resonant optical pumping is described. A sharp laser mode splits from the lower-polariton branch and approaches the bare cavity mode frequency as the pump power increases. The lasing is produced by low density localized exciton states,[120] which are weakly coupled to the cavity mode. The appearance of this quantum-dot-like lasing mode distinguishes between quantum-well excitons which are strongly-coupled and quantum well excitons which are weakly-coupled with the cavity mode.

7.1 Experimental Configuration

The semiconductor microcavity structure under investigation was described in section 3.5.2. A continuous-wave Ti:S pump laser at 1.557eV is used to excite the quantum well (QW) above the band gap. The strong coupling (SC) of the cavity mode with both heavy- and light-hole excitons (X_{hh} and X_{lh}) in the QW results in three polariton branches, see figure 7.1. In this way, unbound electrons and holes are injected at energies $\sim$ 30meV above the heavy- or light-hole excitons in the structure. These carriers relax rapidly onto the lower polariton (LP) branch and create a reservoir of exciton-polaritons at 1.5277eV.[83] This exciton-polariton population (which is termed the 'exciton reservoir' due to the predominantly excitonic character of the

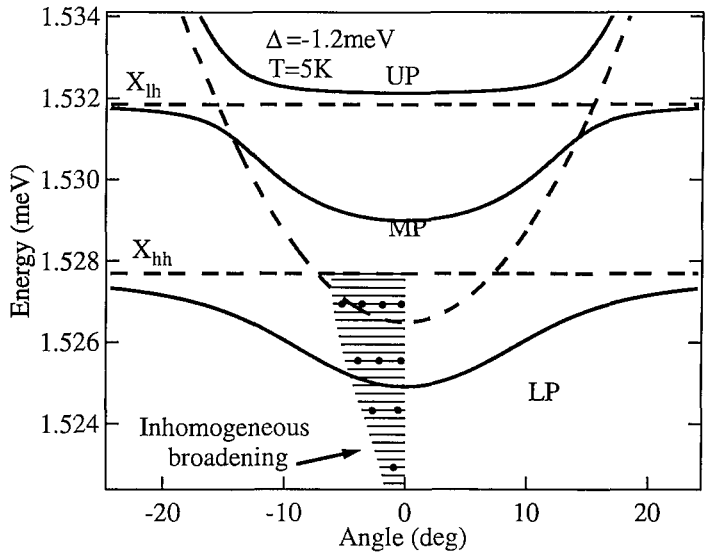

Figure 7.1: Dispersion relations of upper, middle and lower polariton modes (*solid lines*), cavity, X_{hh} and X_{lh} modes (*dashed lines*) for $\Delta = -1.2meV$. The excitation conditions and formation of the 'exciton-reservoir' is depicted with solid arrows

high-wavevector exciton-polaritons) is assumed to be proportional to the pumping power, P, and feeds the lower energy emitting states.

Photoluminescence (PL) spectra are taken at normal incidence for a wide range of pump powers. The emitted light collected in a cone of $\pm 0.15°$ evolves with incident pump power, Fig.7.2. For pump powers above $200\mu W$, an extra unexpected mode appears, termed here the quantum-dot mode (QDM) for reasons explained below. The QDM emerges from the LP mode and shifts to higher energies with increasing pump power, saturating at the energy of the bare exciton mode. This dependence has been observed for a range of detuning (Δ) conditions of exciton and cavity mode (from Δ=+2 to -4meV). At the same time, the peak intensity of the QDM vs pump power exhibits an almost-exponential increase until saturation when its energy reaches the bare cavity mode. Surprisingly, the polariton modes coexist with the QDM for a wide range of pump powers. However, for pump powers above 1mW these modes clearly collapse and the system passes exclusively into the weak coupling (WC) regime.

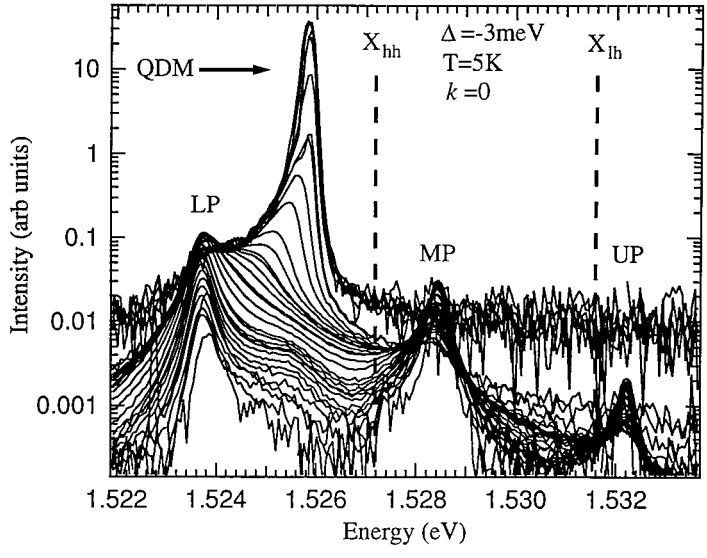

Figure 7.2: Photoluminescence emission from the normal for increasing (upwards) pumping intensities from 200nW to 6mW.

7.2 From Strong to Weak Coupling Regime

To confirm this unexpected coexistence of strong- and weak-coupling regimes, trivial explanations have been discount, such as the coexistence of the two regimes due to the Gaussian excitation beam profile on the sample surface, Fig.7.3a. A well-defined pump power transition between strong and weak coupling corresponds to a particular intensity within the excitation beam profile. Figure 7.3b shows the result of a calculation dividing the pumped area into strong and weak-coupled domains, with the boundary between them radially increasing from the center of the pump spot as the power increases. The calculation is scaled to match the experimentally-observed appearance of the QDM, and to incorporate the observed power dependence of the lower polariton PL, see figure 7.4. The fact that the observed lower polariton PL *does not decrease* beyond the appearance of the QDM mode contrary to the above theory, together with the *gradual* energy shift of the QDM compared to its appearance directly at the bare cavity mode energy, confirms that *a simple collapse is not observed.* Another reason the QDM might be selected is from a resonance between excitation and emission energies when differing by an LO-phonon energy: this is excluded by the absence of any dependence on the excitation energy.

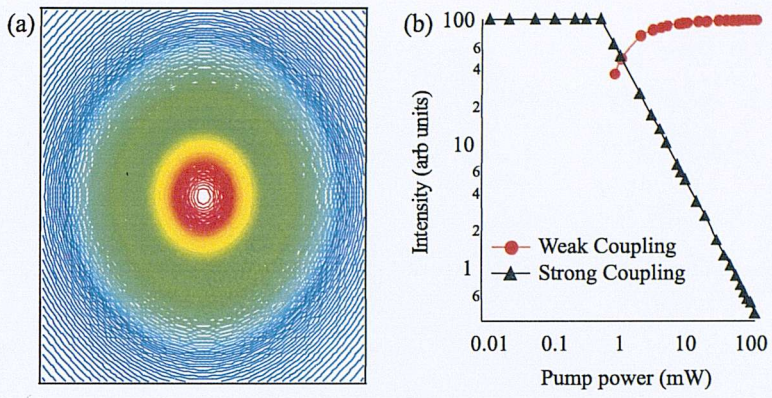

Figure 7.3: (a) Gaussian excitation intensity profile. (b) expected normalised PL for spatially-inhomogeneous Rabi transition due to the Gaussian excitation profile.

Hitherto, the presence of the QDM at zero wavevector has been discussed. However to prove the involvement of cavity feedback it is necessary to angularly resolve the emission. The angular dispersion at the threshold condition is shown in figure 7.5. It is evident that the QDM tracks the cavity mode while the polariton modes are also still present in the heterostructure. Further confirmation of the role of the cavity mode is seen in the detuning dependence (Fig.7.6), which again shows the co-existence of the anti-crossing polaritons modes with the QDM (that follows the bare cavity mode). At higher wavevectors, where the emission of the QDM mode is small, seen in figure 7.5, and does not screen the emission from the strongly coupled modes, the anti-crossing of polariton states is even more pronounced, Fig.7.7.

A basic interpretation for the appearance and evolution of this QDM can be derived from the coupled oscillator model. The strong coupling regime holds if $2\Omega_R > \gamma_x + \gamma_c$, where Ω_R is the exciton-cavity mode coupling (proportional to the square root of the exciton oscillator strength). In every semiconductor heterostructure, both free and localized exciton states exist due to the disorder potential fluctuations. The latter states have a reduced oscillator strength and contribute to the inhomogeneous broadening of the exciton line out of resonance with the cavity mode, but are invisible in microcavity PL spectra in the strong coupling regime, because emission and absorption of light are dominated by free polariton modes shifted far into the tail of localized states. The results presented here show that in high quality microcavities, the extremely low concentration of localized states can be significantly

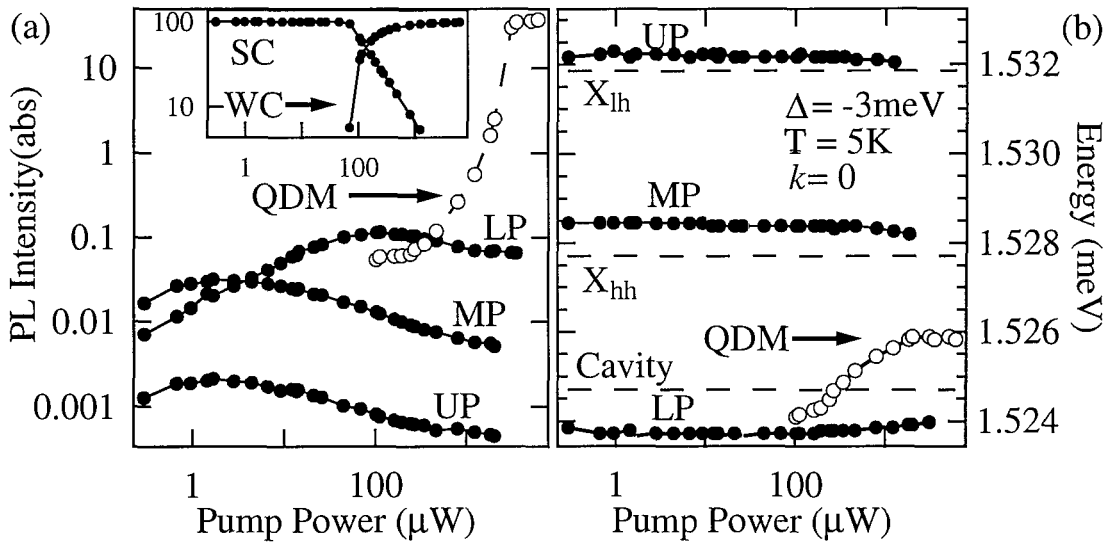

Figure 7.4: (a) Normalized perpendicular PL emission vs. I_{pump}, for polariton modes (•) and the quantum dot-like lasing mode (○). Inset: expected normalized PL for spatially-inhomogeneous Rabi transition. (b) Peak perpendicular PL emission energies vs. I_{pump} for polariton modes (•) and the quantum dot-like lasing mode (○).

populated by non-resonant optical excitation. This results in their population inversion, accompanied by low threshold lasing (absorbed pump power $P \simeq 0.4$ W/cm^{-2}) once the gain is sufficient to offset round trip losses in the high finesse cavity. In this regime, the microcavity acts both as a QD VCSEL and as a strongly-coupled microcavity. This relies on the cavity mode being narrower than the inhomogeneous distribution of localized excitons (as is the case here). The situation is impossible in lower-quality cavities where the round trip losses are higher.

The lasing mode frequency increases with pump power P because localized states at higher energy can now successively become inverted. This occupation of the QD distribution affects both the optical susceptibility and the emission of the microcavity. We assume that non-resonant pumping generates an exciton reservoir with an energy close to the free exciton energy, ω_x. This reservoir has a population N_x that is proportional to the external pumping power P. Relaxation from N_x populates the inhomogeneous QD distribution (of width γ_x) of localized exciton states, whose density $g(\omega)$ is taken to be Gaussian. Furthermore, the following assumptions are made: at low densities, collision between reservoir excitons is the main mechanism

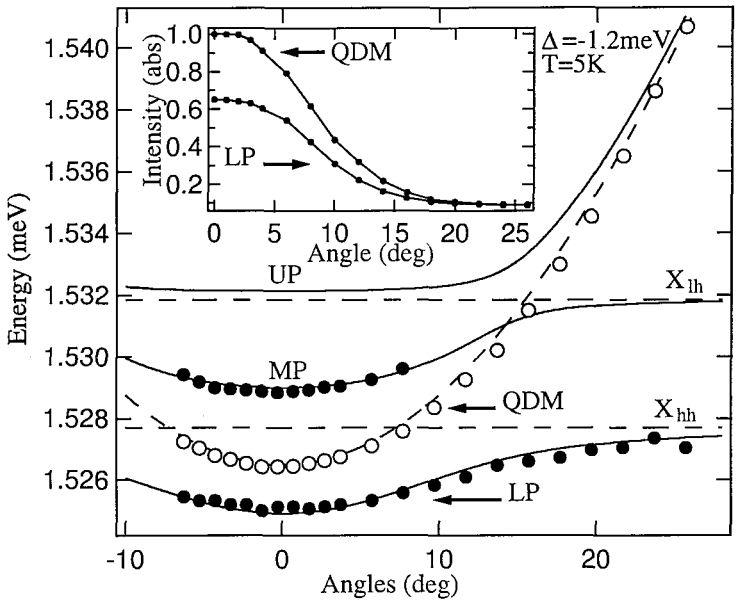

Figure 7.5: Experimental PL emission of upper, middle and lower polariton modes (•) and the quantum dot-like lasing mode (○) together with theoretical dispersions of upper, middle and lower polariton modes (solid lines), cavity, X_{hh} and X_{lh} modes (dashed lines), shown vs angle of emission. Inset shows PL intensity vs angle.

populating localized states, whose total population N_{QD} is thus proportional to P^2; the localized states are sufficiently well thermalized to be described by a Boltzmann distribution defined by a chemical potential $\mu(P)$. All states having an energy smaller than μ are strongly populated and therefore have a vanishing oscillator strength. In the framework of the non-local semi-classical model,[121] the QW susceptibility reads:

$$\tilde{\chi}(\omega,\gamma)=\frac{1}{\pi^{1/2}\gamma_x}\int_{\mu}^{+\infty}\frac{\Gamma_0}{\omega_x-\omega-i\gamma}\exp\left[-\left(\frac{\omega_1-\omega_x}{\gamma_x}\right)^2\right]d\omega_1$$

where Γ_0 is the radiative emission rate of the exciton, and γ is its non-radiative homogeneous broadening. Once this susceptibility is known, one can use the generalized scattering state technique [122] to calculate the emission spectrum of the cavity $F(\omega,\mu)$ produced by an embedded single narrow band emitting state. To obtain the spectral emission of the microcavity, $F(\omega,\mu)$ should be multiplied by the spectral distribution of the embedded emitters. Two main types of emitters are taken into consideration. The first type are SC excitons, which have an emission spectrum $I_{SC}(\omega)$ proportional to the optical susceptibility, $(\tilde{\chi})$. The second type of emitters

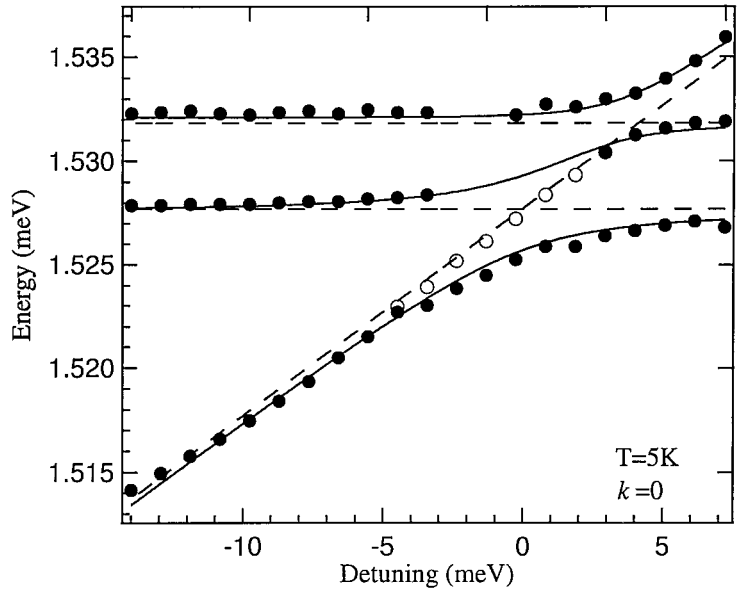

Figure 7.6: (a) Experimental PL emission of upper, middle and lower polariton modes (•) and the quantum dot-like lasing mode (○) together with theoretical dispersions of upper, middle and lower polariton modes (*solid lines*), cavity, X_{hh} and X_{lh} modes (*dashed lines*), shown vs cavity detuning.

are inverted weakly-coupled excitons. The main contribution from WC excitons is assumed to come from the states having an energy equal to the chemical potential. The intensity is therefore proportional to the number of dots at the energy of the chemical potential. The spectral emission from weakly coupled excitons therefore reads (using for simplicity an arbitrary energy at ω_x of zero)

$$I_{QD}(\omega,\mu) = \frac{\exp(-\mu^2)}{\omega - \mu - i\gamma}$$

The total spectrum I_T emitted by the sample is then

$$I_T(\omega,\mu) = [I_{SC}(\omega,\mu) + \alpha I_{QD}(\omega,\mu)]F(\omega,\mu)$$

The only unknown parameters remaining are the phenomenological coefficient α which depends on the density of QD-like states produced by the disorder, and the power dependence of μ. Solving

$$N_{QD} = \int g(\omega) \exp\left(\frac{\mu(P) - \omega}{k_b T}\right) d\omega$$

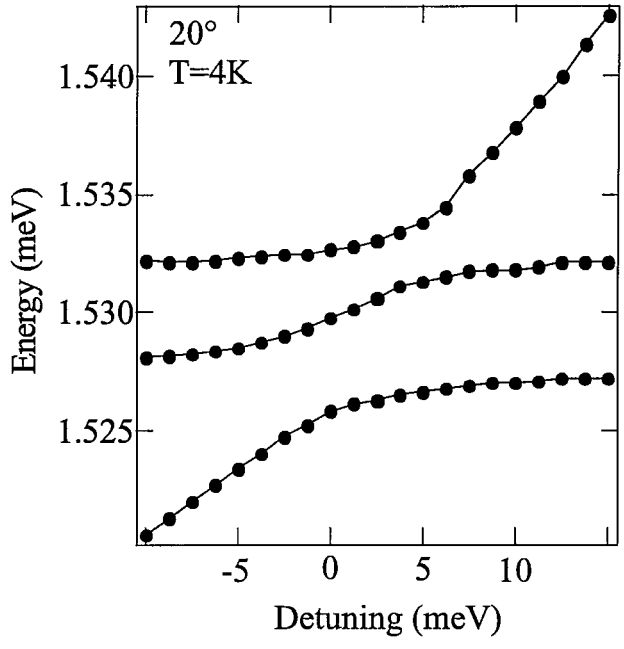

Figure 7.7: (a) Experimental PL emission of upper, middle and lower polariton modes (•) and the quantum dot-like lasing mode (○) together with theoretical dispersions of upper, middle and lower polariton modes (*solid lines*), cavity, X_{hh} and X_{lh} modes (*dashed lines*), shown vs cavity detuning.

where k_b is Boltzmann's constant and T is the temperature, yields

$$\mu(P) = \frac{\gamma_x^2}{2k_bT} \ln(P/P_c)$$

When the critical pump power P_c is reached, μ vanishes and the emission energy reaches the free exciton energy. Thus, μ represents the energy shift of the lasing with respect to the free exciton energy. Using the microcavity parameters and P_c=3mW, the shift of the lasing mode as P is increased to P_c is 1 meV in good agreement with experimental findings.

The emission $I_T(\omega, P)$ is calculated in Figure 7.8 with $\alpha = 1$ and $\Delta = -2$ meV in order to allow direct comparison with Figure 7.4b. Many of the features in the experiment are reproduced by this highly simplified theory, including the shift in the laser emission $\propto \ln(P)$ and the exponential rise in QDM emission, supporting the identification of this QD lasing mode.

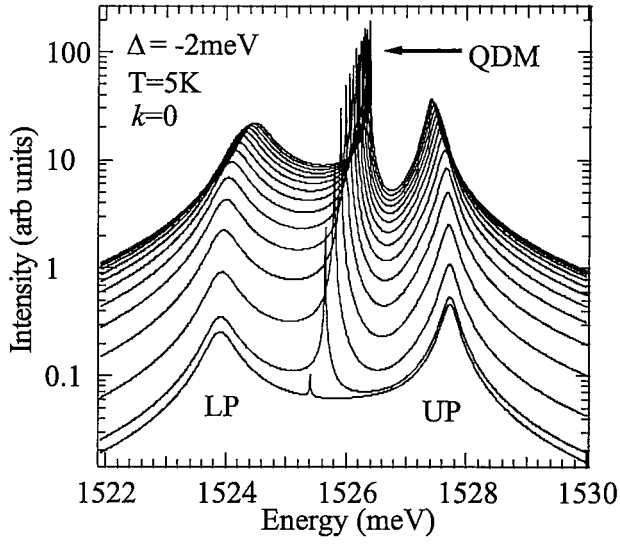

Figure 7.8: Calculated emission from weakly and strongly coupled states. The pump evolves from 200 μW to 3 mW in steps of 200 μW.

7.3 Conclusion

In summary, experimental evidence and a phenomenological model have been presented that show the simultaneous presence of strongly-coupled polariton modes and laser emission from localized exciton states in the same semiconductor microcavity. Anti-crossing behaviour of the coupled cavity and exciton mode has been demonstrated, characteristic of the strong-coupling regime, in addition to the appearance of a new strong line between the polariton eigenstates of the system, whose intensity is exponentially dependent on the pumping power. An intermediate regime has been identified, in which this unexpected lasing mode, which fulfills the characteristics of the weak-coupling regime, coexists with the free polariton modes. This extra mode has been interpreted as the result of a population inversion of localized exciton states that behave as quantum-dot-like traps in the plane of the quantum well. The theoretical model explains why the population inversion at pump densities lower than the Rabi-transition threshold density is only possible in high quality microcavities possessing a very low concentration of localized states. This work thus links the fields of VCSELs and strongly-coupled microcavities and is important for future generations of highly efficient semiconductor emitters.

Chapter 8

Conclusions and Outlook

The work presented in this thesis is an investigation of exciton-polariton dynamics in semiconductor microcavities. Quantum confinement of both photon and exciton modes in a single microscale heterostructure modifies the dispersion relations of the bare modes. Fine tuning of the confinement parameters results in tailoring of the polariton dispersion. Since the properties of polaritons are being very different from those of bare exciton and photon modes, the tunability of their dispersion provides a fertile ground for research. Interest lies both in the investigation of the fundamental physics and in the potential for future technological applications.

Due to the pronounced bosonic properties of polaritons, the microcavity system is a good candidate for the realization of non-equilibrium Bose-Einstein condensate in solid state physics. Electron-polariton scattering has been proposed as a key process for driving polaritons from the bottleneck region to the ground polariton state. By employing a semiconductor microcavity structure that allows control of the free electron density, electron-polariton scattering was investigated under continuous wave non-resonant excitation. The photoluminescence enhancement from the ground polariton state was studied as a function of free carrier density, exciton-cavity resonance detuning, and temperature. Under optimal conditions, a substantial emission enhancement was observed from the ground polariton state, and a phenomenological explanation was attributed to the experimental observations.

The transition of the exciton-photon interaction from the strong coupling to the weak coupling regime can be used to characterize the electron-polariton scattering strength. A steady state solution of the dynamics derived from the electron-exciton

Hamiltonian in the microcavity system can result in an estimation for the value of the strength of the interaction when the electron density is known and vice versa. The effect of electron-polariton scattering on the parametric polariton scattering was recently investigated. The presence of free carriers had a rather detrimental effect. The gain of the process was decreasing with increasing electron density in the structure probably due to the decoherence caused by the electron-polariton scattering to the final polariton states of the parametric scattering. Another interesting point is the experimental investigation of electron-polariton scattering under resonant excitation of the bottleneck region. Ultrafast spectroscopy in this regime can provide information for the dynamics of the scattering and the relaxation time of the free carriers.

The spin dynamics of the polariton parametric amplifier were also investigated in this study. Complete measurement of the emitted polarization state was performed both for signal and idler. Disentanglement of the different mechanisms that contribute to the peculiar characteristics of the spin dynamics was performed in terms of the well studied exciton spin dynamics. The model initially provides a phenomenological explanation of the main, experimentally observed features. The microscopic formulation of the dynamical evolution of the system was set and numerical simulations of the derived equations of motion are in progress. Future experiments involve measurement of the spin evolution in a very short time scale (picosecond range) in order to resolve the precession of the exciton spin under the influence of the pump induced magnetic field.

The transition from strong to weak coupling regime was investigated in semiconductor microcavities. An intermediate regime was observed, in which the peculiar characteristics of the spin dependence of the stimulated polariton scattering led to the polariton modes coexistence with a lasing mode that fulfills the characteristics of the weak coupling regime. This observation leads to the true picture for the coupling of light with the electronic excitation. In an otherwise strongly coupled microcavity, excitons are separated into those which couple strongly with light and those which remain in the weak coupling regime. A phenomenological model was used to explain the observed energy shifts of the lasing mode.

Future experimental studies focus on the interesting phenomena of the non-equilibrium

polariton condensates. The understanding of the fundamental physics underlying polariton condensate can be improved by experimental observations that reveal the condensate dynamics. Experimental techniques for measuring the superfluid properties of polariton condensates and the interactions of two spatially separated polariton spin condensates are under development.

Bibliography

[1] D. A. B. Miller. *Physical reasons for optical interconnection.* Int. J. Optoelectronics **11**, 155 (1997).

[2] A. Yariv. *Quantum Electronics.* Wiley, New York, 1988.

[3] E. Burstein, and C. Weisbuch. *Confined Electrons and Photons.* Plenum, New York, 1995.

[4] K. Huang. Proc. Roy. Soc. A, **208**, 352 (1951).

[5] J. J. Hopfield. Phys. Rev. **112**, 1555 (1958).

[6] D. Fröhlich, E. Mohler, and P. Wiesner. Phys. Rev. Lett. **26**, 554 (1971).

[7] B. Hönerlage, A. Bivas, and V. Phach. Phys. Rev. Lett **41**, 49 (1978).

[8] R. G. Ulbrich and G. W. Fehrenbach. Phys. Rev. Lett. **43**, 963 (1979).

[9] A. Toyozawa. Prog. Theor. Phys. Suppl. **12**, 111 (1959).

[10] H. Sumi. J. Phys. Soc. Jpn **21**, 1936 (1976).

[11] C. Weisbuch, and R. G. Ulbrich. Phys. Rev. Lett. **39**, 654 (1977).

[12] C. Weisbuch, C. Ulbrich, and R. Ulbrich. J. Lumin. **18/19**, 27 (1979).

[13] V.M. Agranovich, and A. O. Dubowskii. Pis'ma Zh. Eksp. Teor. Fiz. **3**, 345 (1966)[JTEP Lett. **3**, 233 (1966)]

[14] J. Hegarty, L. Goldner, and M. D. Sturge. Phys. Rev. B **30**, 7346 (1984).

[15] J. Hegarty, and M. D. Sturge. J. Opt. Soc. Am. B **2**, 1143 (1985).

[16] B. Deveaud, F. Clérot, N. Roy, S. Satzke, B. Sermage, and D. S. Katzer. Phys. Rev. Lett. **67**, 2355 (1991).

[17] E. Purcell. Phys. Rev. **69**, 681 (1946).

[18] C. Weisbuch, M. Nishioka, A. Ishikawa, and Y. Arakawa. Phys. Rev. Lett. **69**, 3314 (1992).

[19] R. Houdré, C. Weisbuch, R. Stanley, U. Oesterle, P. Pellandini, and M. Ilegems. Phys. Rev. Lett. **73**, 2043 (1994).

[20] E. Hanamura, and H. Haug. Physics Reports **33C**, 209 (1977).

[21] A. Griffin, D. Snoke, and S. Stringari. *Bose-Einstein condensation.* CUP, Cambridge, 1995.

[22] F. Dalfovo, S. Giorgini, L. P. Pitaevskii, and S. Stringari. *Theory of Bose Einstein Condensation in Trapped Gases.* Rev. Mod. Phys. **71**, 463 (1999).

[23] P. Savvidis, J. Baumberg, R. Stevenson, M. Skolnick, D. Whittaker, and J. Roberts. Phys. Rev. Lett. **84**, 1547 (2000).

[24] R. Stevenson, V. Astratov, M. Skolnick, D. Whittaker, M. Emam-Ismail, A. Tartakovskii, P. Savvidis, J. Baumberg, and J. Roberts. Phys. Rev. Lett. **85**, 3680 (2000).

[25] G. Malpuech, A. Kavokin, A. Di Carlo, and J. J. Baumberg. Phys. Rev. B **65**, 153310 (2002).

[26] A. Kavokin, P. G. Lagoudakis, G. Malpuech and J. J. Baumberg. Phys. Rev. B **67**, 195321 (2003).

[27] P. G. Lagoudakis, M. D. Martin, J. J. Baumberg, A. Qarry, E. Cohen and L. N. Pfeiffer. Phys. Rev. Lett. **90**, 206401 (2003).

[28] Peter Y. Yu, and Manuel Cardona. *Fundamentals of Semiconductors.* Springer-Verlag, Berlin, 2001.

[29] G. H. Wannier. Phys. Rev. **52**, 191 (1937).

[30] J. Frenkel. Phys. Rev. **37**, 17 (1931).

[31] W. W. Chow and S. W. Koch. *Semiconductor Laser Fundamentals: Physics of the Gain Materials* Springer-Verlag, Berlin Heidelberg, 1999.

[32] C. Weisbuch and B. Vinter. *Quantum Semiconductor Structures.* Academic Press, Boston, 1991.

[33] R. Dingle. Festkoerperprobleme **15**, 21 (1975).

[34] L. C. Andreani, in *Confined Electrons and Photons,* edited by E. Burstein, and C. Weisbuch. Plenum, New York, 1995.

[35] E. O. Kane, in *Semiconductors and Semimetals,* edited by R. K. Willardson, and A. C. Beer. Academic, New York, p.75, 1966.

[36] J. M. Luttinger, and W. Kohn Phys. Rev. **97**, 869 (1954).

[37] J. M. Luttinger. Phys. Rev. **102**, 1030 (1956).

[38] G. E. Pikus and E. L. Ivchenko, in *Excitons*, edited by E. I. Rashba and M. D. Sturge. North-Holland, Amsterdam, p.205, 1982.

[39] R. Planel and C. Benoit a la Guilaume, in *Optical Orientation*, edited by F. Meier and B. P. Zakharchenya North-Holland, Amsterdam, p.353, 1984.

[40] E. L. Ivchenko. Pure Appl. Chem. **67**, 463 (1995).

[41] E. L. Ivchenko and G. E. Pikus. *Superlattices and other Heterostructures. Symmetry and Optical Phenomena.* Springer-Verlag, Berlin, 1995.

[42] Y. Yamamoto, F. Tassone, and H. Cao. *Semiconductor Cavity Quantum Electrodynamics.* Springer Tracts in Modern Physics **169**, Berlin, 2000.

[43] R. E. Slusher, C. Weisbuch. Solid State Commun. **92**, 149 (1994).

[44] R. Stanley, R. Houdre, and U. Oesterle. App. Phys. Lett. **65**, 1883 (1994).

[45] H. A. McLeod. *Thin Film Optical Filters*, second edition. Hilger, 1986.

[46] M. Born, and E. Wolf. *Principles of Optics*, sixth edition. Plenum Press, Oxford, 1980.

[47] U. Fano. Phys. Rev. **124**, 1866 (1961).

[48] K. H. Drexhage. in *Progress in Optics*, edited by E. Wolf. North-Holland, New York, 1974.

[49] F. Bassani, and G. Pastori Parravicini. *Electronic States and Optical Transitions in Solids.* Pergamon Press, Oxford, 1975.

[50] V. Savona, C. Piermarocchi, A. Quattropani, P. Schwindimann, and F. Tassone. Phase Transitions **68**, 169 (1999).

[51] F. Bassani, F. Ruggiero, and A. Quattropani. Nuovo Cimento D, **7**, 700 (1986)

[52] C. Rulliere. *Femtosecond Laser Pulses.* Springer, 1998.

[53] C. Ell, J. Prineas, T. Nelson, S. Park, H. Gibbs, G. Khitrova, and S. Koch. Phys. Rev. Lett. **80**, 4795 (1998).

[54] J. Baumberg, A. Armitage, M. Skolnick, and J. Roberts. Phys. Rev. Lett. **81**, 661 (1998).

[55] A. Weiner, D. Leaird, J. Patel, and J. Wullert. Opt. Lett. **15**, 326 (1990).

[56] J. Scofield. American. Journal of Physics **62**, 139 (1994).

[57] P. G. Savvidis. PhD Thesis University of Southampton, UK, 2001

[58] G. Stokes. Trans. Cambridge Phil. Soc. **9**, 399 (1852).

[59] H. Mueller. J. Opt. Soc. Am. **38**, 661 (1948).

[60] I. Galbraith, P. Dawson, and C. T. Foxon. Phys. Rev. B **45**, 13499 (1992).

[61] J. Feldmann, J. Nunnenkamp, G. Peter, E. Gbel, J. Kuhl, K. Ploog, P. Dawson, and C. T. Foxon. Phys. Rev. B **42**, 5809 (1990).

[62] Ronen Rapaport, E. Cohen, Arza Ron, Evegeny Linder, and L. N. Pfeiffer. Phys. Rev. B **63**, 235310 (2001).

[63] Z. L. Zhang, M. Nishioka, C. Weisbuch, and Y. Arakawa. Appl. Phys. Lett. **64**, 1068 (1994).

[64] T. Yamauchi, Y. Arakawa, and M. Nishioka. Appl. Phys. Lett. **58**, 2339 (1991).

[65] A. Frey, G. Jungk, and R. Hey. Appl. Phys. Lett. **64**, 2214 (1994).

[66] Lucio Claudio Andreani, and Alfredo Pasquarello. Phys. Rev. B **42**, 8928 (1990).

[67] E. Grilli, M. Guzzi, R. Zamboni, and L. Pavesi. Phys. Rev. B **45**, 1638 (1992).

[68] J. Talghader and J. S. Smith. Appl. Phys. Lett. **66**, 335 (1995).

[69] T. Fisher, A. Afshar, D. Whittaker, J. Roberts, G. Hill, and M. Pate. Phys. Rev. B **51**, 2600 (1995).

[70] Y. Zhu, D. J. Gauthier, S. E. Morin, Q. Wu, M. J. Carmichael, and T. W. Mossberg. Phys. Rev. Lett. **64**, 2499 (1990).

[71] W. T. Masselink, P. J. Pearah, J. Klem, C. K. Peng, H. Morkoc, G. D. Sanders and Y.-C. Chang. Phys. Rev. B **32**, 8027 (1985).

[72] D. A. B. Miller, D. S. Chemla, T. C. Damen, A. C. Gossard, W. Wiegmann, T. H. Wood and C. Burrus. Phys. Rev. B **32**, 1043 (1985).

[73] T. Fisher, A. Afshar, M. Skolnick, D. Whittaker, J. Roberts, G. Hill, and M. Pate. Solid State Electronics **40**, 493 (1996).

[74] Ronen Rapaport, E. Cohen, Arza Ron, Evegeny Linder, and L. N. Pfeiffer. Phys. Rev. Lett. **84**, 1607 (2000).

[75] S. Schmitt-Rink, D. S. Chemla, and D. A. B. Miller. Adv. Phys. **38**, 89 (1989).

[76] Alexey Kavokin, Guillaume Malpuech, Fabrice P. Laussy.
Physics Letters A **306** 187 (2003).

[77] Y. Yamamoto, F. Matinaga, S. Machida, A. Krlsson, J. Jacobson, G. Bjork and T. Mukai. J. Phys (France) II **3**, 39 (1993).

[78] S. Pau, H. Cao, J. Jacobson, G. Bjork, Y. Yamamoto, and A. Imamoglu.
Phys. Rev. A **54**, R1789 (1996).

[79] S. Pau, G. Bjautrk, H. Cao, F. Tassone, R. Huang, Y. Yamamoto, and R. Stanley.
Phys. Rev. B **55**, R1942 (1997).

[80] M. Kira, J. F., S. W. Koch, J. D. Berger, D. V. Wick, T. R. Nelson, G. Khitrova, and H. M. Gibbs. Phys. Rev. Lett. **79**, 5170 (1997).

[81] Le Si Dang, D. Heger, R. Andre, F. Boeuf, and R. Romestain.
Phys. Rev. Lett. **81**, 3920 (1998).

[82] P. Senellart and J. Bloch. Phys. Rev. Lett. **82**, 1233 (1999).

[83] F. Tassone, C. Piermarocchi, V. Savona, A. Quattropani, and P. Schwendimann.
Phys. Rev. B **56**, 7554 (1997).

[84] T. Baars, M. Bayer, A. Forchel, F. Schafer, and J. Reithmaier.
Phys. Rev. B **61**, R2409 (2000).

[85] Markus Müller, Joël Bleuse, and Régis André Phys. Rev. B **62**, 16886 (2000).

[86] A. Tartakovskii, M. Emam-Ismail, R. Stevenson, M. Skolnick, V. Astratov, D. Whittaker, J. Baumberg, and J. Roberts. Phys. Rev. B **62**, R2283 (2000).

[87] F. Tassone and Y. Yamamoto. Phys. Rev. B **59**, 10830 (1999).

[88] R. Huang, F. Tassone, and Y. Yamamoto. Phys. Rev. B **61**, R7854 (2000).

[89] P. Savvidis, J. Baumberg, R. Stevenson, M. Skolnick, D. Whittaker, and J. Roberts. Phys. Rev. B **62**, R13278 (2000).

[90] M. Saba, C. Ciuti, J. Bloch, V. Thierry-Mieg, R. André, Le Si Dang, S. Kundermann, A. Mura, G. Bongiovanni, J. L. Staehli, and B. Deveaud.
Nature **414**, 731 (2001).

[91] J. Baumberg, P. Savvidis, R. Stevenson, A. Tartakovskii, M. Skolnick, D. Whittaker, and J. Roberts. Phys. Rev. B **62**, R16247 (2000).

[92] M. Z. Maialle, E. A. de Andrada e Silva, and L. J. Sham.
Phys. Rev. B **47**, 15776 (1993).

[93] M. D. Martin, G. Aichmayr, and L. Viña R. André.
Phys. Rev. Lett. **89**, 077402 (2002).

[94] I. A. Shelykh, A. V. Kavokin, K. V. Kavokin, P. Bigenwald, and G. Malpuech. submitted to Phys. Stat. Sol. (c) (2003).

[95] A. I. Tartakovskii, D. N. Krizhanovskii, and V. D. Kulakovskii.
Phys. Rev. B **62**, R13298 (2000).

[96] P. G. Lagoudakis, P. G. Savvidis, J. J. Baumberg, D. M. Whittaker, P. R. Eastham, M. S. Skolnick, and J. S. Roberts.
Phys. Rev. B. **65**, 161310 (R) (2002).

[97] R. Houdré, R. Giberon, P. Pellandini, R. P. Stanley, U. Oesterle, C. Weisbuch, J. O'Gorman, B. Roycroft, and M. Ilegems. Phys. Rev. B **52**, 7810 (1995).

[98] R. Butté, G. Delalleau, A. I. Tartakovskii, M. S. Skolnick, V. N. Astratov, J. J. Baumberg, G. Malpuech, A. Di Carlo, A. V. Kavokin, and J. S. Roberts.
Phys. Rev. B **65**, 205310 (2002).

[99] R. Huang, Y. Yamamoto, R. André, J. Bleuse, M. Muller, and H. Ulmer-Tuffigo.
Phys. Rev. B **65**, 165314 (2002).

[100] Marian Zamfirescu, Alexey Kavokin, Bernard Gil, Guillaume Malpuech, and Mikhail Kaliteevski. Phys. Rev. B **65**, 161205 (R) (2002).

[101] Claude Benoit à la Guillaume, Jean-Marie Debever, and Frank Salvan. Phys. Rev. **177**, 567 (1969).

[102] Guillaume Malpuech, Aldo Di Carlo, Alexey Kavokin, Jeremy J. Baumberg, Marian Zamfirescu, and Paolo Lugli
Appl. Phys. Lett. **81**, 412 (2002).

[103] A. I. Tartakovskii, D. N. Krizhanovskii, G. Malpuech, M. Emam-Ismail, A. V. Chernenko, A. V. Kavokin, V. D. Kulakovskii, M. S. Skolnick, and J. S. Roberts. Phys. Rev. B **67**, 165302 (2003).

[104] G. Ramon, A. Mann, and E. Cohen. Phys. Rev. B **67**, 045323 (2003).

[105] A. Qarry, G. Ramon, R. Rapaport, E. Cohen, Arza Ron, A. Mann, E. Linder, and L. N. Pfeiffer. Phys. Rev. B **67**, 115320 (2003).

[106] P. G. Savvidis, J. J. Baumberg, D. Porras, D. M. Whittaker, M. S. Skolnick, and J. S. Roberts. Phys. Rev. B **65**, 073309 (2002).

[107] J. Erland, V. Mizeikis, W. Langbein, J. Jensen, and J. Hvam.
Phys. Rev. Lett. **86**, 5791 (2001).

[108] C. Ciuti, V. Savona, C. Piermarocchi, A. Quattropani, and P. Schwendimann, Phys. Rev. B. **58**, 7926 (1998).

[109] Lucio Claudio Andreani, and Franco Bassani. Phys. Rev. B **41**, 7536 (1990).

[110] F. Tassone, F. Bassani, and Lucio Claudio Andreani. Phys. Rev. B **45**, 6023 (1992).

[111] J. Fernandez-Rossier and C. Tejedor. Phys. Rev. Lett. **78**, 4809 (1997).

[112] Richard P. Feynman, Frank L. Vernon, and Robert W. Hellwarth. J. of Appl. Phys. **28**, 49 (1957).

[113] R. I. Dzhioev, H. M. Gibbs, E. L. Ivchenko, G. Khitrova, V. L. Korenev, M. N. Tkachuk, and B. P. Zakharchenya. Phys. Rev. B, **56**, 13405 (1997).

[114] C. Ciuti, P. Schwendimann, B. Deveaud, and A. Quattropani. Phys. Rev. B **62**, R4825 (2000).

[115] G. Rochat, C. Ciuti, V. Savona, C. Piermarocchi, A. Quattropani, and P. Schwendimann. Phys. Rev. B **61**, 13856 (2000).

[116] H. J. Carmichael, R. J. Brecha, M. G. Raizen, H. J. Kimble, and P. R. Rice. Phys. Rev. A **40**, 55165519 (1989).

[117] V. Savona, and C. Weisbuch Phys. Rev. B **54**, 10835 (1996).

[118] P. G. Savvidis, C. Ciuti, J. J. Baumberg, D. M. Whittaker, M. S. Skolnick, and J. S. Roberts, Phys. Rev. B **64**, 75311 (2000).

[119] C. Ciuti. PhD thesis, Swiss Federal Institute of Technology, Lausanne-Switzerland, 2001.

[120] X. Fan, H. Wang, H. Hou, and B. Hammons. Phys. Rev. B **56**, 15256 (1997).

[121] L. C. Andreani, G. Panzarini, A. V. Kavokin, and M. R. Vladimirova. Phys. Rev. **B 57**, 4670, (1998).

[122] G. Malpuech, and A. Kavokin. Semicond. Sci. Technol. Topical Rev. **16** R1 (2001).

Selected Publications

- P. G. Lagoudakis, J. J. Baumberg, G. Malpuech, and A. Kavokin, *Quantum Dot lasing from strongly-coupled Semiconductor Microcavities*, submitted in App. Phys. Lett. (2003).

- P. G. Savvidis, P. G. Lagoudakis, *Teaching Polaritons new tricks*, accepted in Semiconductor Science & Technology (2003).

- P. G. Lagoudakis, M. D. Martin, J. J. Baumberg, A. Qarry, E. Cohen and L. N. Pfeiffer, *Electron-Polariton Scattering in n-doped Semiconductor Microcavities*, Phys. Rev. Lett. **90**, 206401 (2003).

- A. Kavokin, P. G. Lagoudakis, G. Malpuech and J. J. Baumberg, *Polarization rotation in parametric scattering of polaritons in semiconductor microcavities*, Phys. Rev. B **67**, 195321 (2003)

- A. Kavokin, G. Malpuech, P. G. Lagoudakis, J. J. Baumberg, K. Kavokin, *Polarisation rotation in resonant emission of semiconductor microcavities*, Phys. Stat. Sol. (a) 195, 579 (2003).

- J. J. Baumberg, P. G. Lagoudakis, M. D. Martin, *Lasing and Condensation in Semiconductor Microcavities*, accepted in Nuovo Cimento (2002).

- P. G. Lagoudakis, P. G. Savvidis, J. J. Baumberg, D. M. Whittaker, P. R. Eastham, M. S. Skolnick, and J. S. Roberts, *Stimulated spin dynamics of polaritons in semiconductor microcavities*, Phys. Rev. B **65** R161310 (2002).

- J. J. Baumberg, P. G. Savvidis, P. G. Lagoudakis, M. D. Martin, D. M. Whittaker, M.S. Skolnick, J.S. Roberts, *Polariton Traps in Semiconductor Microcavities*, Physica E **13** 385 389 (2002).